Title

I: Low-Frequency NMR and NQR Using a dc SQUID II: Variable-Temperature 13C CP/MAS of Organometallics

Author

Ziegeweid, Marcia A

Publication Date

1995-11-01

LBL-38324

ERNEST ORLANDO LAWRENCE
BERKELEY NATIONAL LABORATORY

I: Low-Frequency NMR and NQR Using a dc SQUID
II: Variable-Temperature ^{13}C CP/MAS of Organometallics

Marcia A. Ziegeweid

Materials Sciences Division

November 1995

Ph.D. Thesis

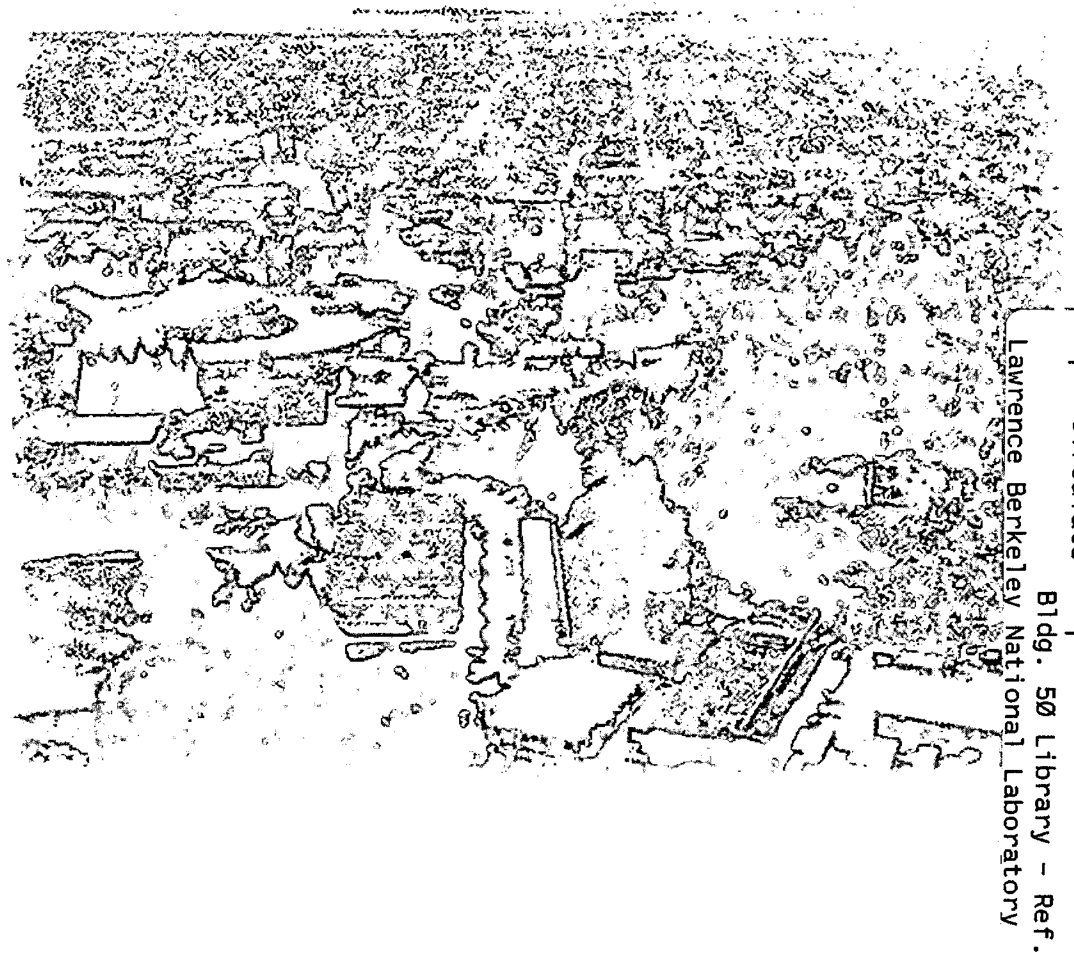

DISCLAIMER

LBL-38324

I: Low-Frequency NMR and NQR Using a dc SQUID
II: Variable-Temperature ^{13}C CP/MAS of Organometallics

Marcia A. Ziegeweid
Ph.D. Thesis

Department of Chemistry
University of California, Berkeley

and

Materials Sciences Division
Ernest Orlando Lawrence Berkeley National Laboratory
University of California
Berkeley, California 94720

November 1995

This work was supported by the Director, Office of Energy Research, Office of Basic Energy Sciences, Materials Sciences Division, of the U.S. Department of Energy under Contract No. DE-AC03-76SF00098.

I: Low-Frequency NMR and NQR Using a dc SQUID
II: Variable-Temperature ^{13}C CP/MAS of Organometallics

by

Marcia Ann Ziegeweid

B.S. (University of Wisconsin-La Crosse) 1990

A dissertation submitted in partial satisfaction of the
requirements for the degree of
Doctor of Philosophy
in
Physical Chemistry
in the
GRADUATE DIVISION
of the
UNIVERSITY of CALIFORNIA at BERKELEY

Committee in charge:

Professor Alexander Pines, Chair
Professor Charles Harris
Professor John Clarke

1995

I: Low-Frequency NMR and NQR Using a dc SQUID
II: Variable-Temperature ^{13}C CP/MAS of Organometallics

by

Marcia Ann Ziegeweid

Abstract

I: Low-Frequency NMR and NQR Using a dc SQUID

II: Variable-Temperature ^{13}C CP/MAS of Organometallics

by

Marcia Ann Ziegeweid

Doctor of Philosophy in Physical Chemistry

University of California at Berkeley

Professor Alexander Pines, Chair

NMR and NQR at low frequencies are difficult prospects due to small nuclear spin polarization. Furthermore, the sensitivity of the inductive pickup circuitry of standard spectrometers is reduced as the frequency is lowered. I have used a cw-SQUID (Superconducting QUantum Interference Device) spectrometer, which has no such frequency dependence, to study the local atomic environment of ^{14}N via the quadrupolar interaction. Because ^{14}N has spin I=1 and a 0-6 MHz frequency range, it is not possible to obtain well-resolved spectra in high magnetic fields.. I have used a technique to observe ^{14}N NQR resonances via their effect on neighboring protons mediated by the heteronuclear dipolar interaction to study peptides and narcotics.

The sensitivity of the SQUID is not enough to measure low-frequency surface (or other low spin density) systems. The application of spin-polarized xenon has been previously used to enhance polarization in conventional NMR experiments. Because xenon only polarizes spins with which it is in contact, it is surface selective. While differences in chemical shifts between surface and bulk spins are not large, it is expected that the differences in quadrupole coupling constant should be very large due to the drastic change of the electric field gradient surrounding spins at the surface. With this in mind, I have taken preliminary steps to measure SQUID detected polarization transfer from Xe to another spin species at 4.2 K and in small magnetic fields (<50 G). In this regime, the

spin-lattice relaxation of xenon is dependent on the applied magnetic field. The results of our efforts to characterize the relaxation of xenon are presented.

The final section describes the solid-state variable-temperature (VT) one- and two-dimensional ^{13}C cross polarization (CP)/magic angle spinning (MAS) NMR of $Hf(\eta^5\text{-}C_5H_5)_2(\eta^1\text{-}C_5H_5)_2$, $Zr(\eta^5\text{-}C_5H_5)_3(\eta^1\text{-}C_5H_5)$ and $Sn(\eta^1\text{-}C_5H_5)_4$. This work was undertaken in the hope of gaining insight into the intramolecular dynamics, specifically which fluxional processes exist in the solid state, by what mechanism rearrangements are occurring, and the activation energies by which these processes are governed.

Table of Contents

List of Figures

Acknowledgements

I'd like to thank the many people who I have worked with over the last three and a half years: my advisor Alex Pines for his time, commitment, and inspiration; my "adopted" advisor John Clarke for his support and the physics perspective; Bruce Black and Ulli Werner-Zwanziger for introducing me to ^{14}N NQR; Al Garroway of the Naval Research Laboratory for collaborating with me on the ^{14}N detection in narcotics; Dinh Ton for our collaboration on the pulsed SQUID project (as well as Yi-Qiao Song, Tanja Pietraß, and Eric Munson); Susan DePaul and Eric Munson for collaboration on the organometallics work; Gerry Chingas who seemed to know the answers to all my questions about electronics; Dione Carmichael who keeps the group running; all of the Pinenuts, past and present, that made this environment such a positive one; and my family, friends, and Alan Stellpflug for putting up with me for all these years.

Chapter 1 Introduction

Nuclear magnetic resonance (NMR) and nuclear quadrupole resonance (NQR) are two experimental techniques which have become important in research as well as analytical applications. NMR studies the interaction of a nucleus with a magnetic field, while NQR studies the interaction with the electric quadrupole moment of a nucleus (present in nuclei with $I > 1/2$) with the surrounding electric field gradient. As these interactions have become well understood, a variety of experimental techniques have been developed and continue to evolve to probe the structure and dynamics of many systems. These include medical[1] and materials[2] imaging, investigations of the dynamics of polymers[3], and the detection of narcotics and explosives[4,5], to name a few.

The two issues that are always present when conducting experiments are resolution and sensitivity. In liquids, NMR has inherently been a high-resolution technique since the rapid tumbling of molecules in solution averages interactions to their isotropic values. In solid-state NMR, a high degree of resolution has also been achieved by artificially inducing an isotropic character. This has been achieved by spinning experiments[6-8], pulse gymnastics[9-11], and zero field[12,13] techniques. NQR techniques performed in the absence of a static magnetic field have inherently high resolution. However, since the transition frequencies tend to be much smaller than NMR transition frequencies, the resolution is achieved at the expense of sensitivity.

Low sensitivity is inherent in NMR and NQR due to the small transition frequencies and the correspondingly small difference in the Boltzmann distribution of spins in these energy levels. The problem of low sensitivity is compounded by the use of Faraday detectors in most magnetic resonance spectrometers. A Faraday detector measures the voltage produced as the transverse magnetization oscillates at the resonance frequency after rf irradiation[14]. The sensitivity is proportional to the rate of change of magnetization and, thus, decreases linearly with frequency. NMR has typically addressed this issue by increasing the strength of the applied static magnetic field to increase the separation of the energy levels and, therefore, the population difference. It has also been addressed by the use of spin-exchange optical pumping to artificially induce a high degree of polarization[15,16]. This method of increasing sensitivity is not limited to high field techniques, as will be shown later in this thesis. The application of a large magnetic field is not practical in NQR experiments because it can broaden and distort the otherwise sharp quadrupolar resonances. Quadrupole transition frequencies can range from zero to hundreds of megahertz. Conventional NQR has been able to measure frequencies as low as 1-3 MHz, the exact lower limit dependent on the spectrometer[17,18]. Transition frequencies below this threshold have also been studied by techniques such as field cycling[19,20], where the system is prepared in high magnetic field to increase the population difference between the energy levels, adiabatically demagnetized, irradiated at a specific rf frequency, and adiabatically remagnetized for detection. However, this is ultimately a point-by-point method of acquiring a spectrum and therefore more efficient techniques are sought. To study low-frequency NMR and NQR resonances a Superconducting QUantum Interference Device (SQUID) has been employed. It is a very sensitive detector whose characteristics will be discussed later.

Quadrupole Interaction

There are several interactions to be discussed that are relevant to the experiments in this thesis. The first of these is the quadrupolar interaction. The quadrupolar interaction arises from the interaction of the electric quadrupole moment of a spin I ≥ 1 nucleus with the surrounding electric field gradient. The electric field gradient is usually generated by electrons in non-spherically symmetric orbitals around the nucleus or by electronic charges on other nuclei near the nucleus of interest. The Hamiltonian is written as the product of the electric field gradient and the electric quadrupole moment.

$$H_Q = \frac{e^2qQ}{4I(2I-1)}[3I_z{}^2 - I^2 + \frac{\eta}{2}(I_+{}^2 + I_-{}^2)], \qquad 1.1$$

Equation 1.1 is written in the principal axis system of the quadrupole interaction, which is a coordinate system in which the interaction is diagonal. In this system, the components of the electric field gradient, V_{zz}, V_{xx}, and V_{yy}, correspond to the z, x, and y axes respectively. Since $V_{xx} + V_{yy} + V_{zz} = 0$, only two parameters are required to define the electric field gradient. By convention they have been chosen as

$$eq = V_{zz} \qquad \eta = (V_{xx}-V_{yy})/V_{zz} \qquad 1.2$$

The terms I_z, I_+, and I_- in equation 1.1 are the components of nuclear spin angular momentum in the principal axis system of the quadrupolar interaction.

Zeeman Interaction

The Zeeman interaction results when a nuclear magnetic dipole is placed in a static magnetic field, H_o. In a frame in which the field is along the z-axis, the Hamiltonian is

$$H_z = -\gamma\hbar I_z B_0. \qquad 1.3$$

The product of the gyromagnetic ratio, γ, and the field strength, H_o, is defined as the Larmor frequency $\omega_o = \gamma H_o$. If the quadrupole interaction is the dominant interaction, it is usually more convenient to write the Zeeman Hamiltonian in the principal axis system of the quadrupolar Hamiltonian,

$$H_z = -\gamma\hbar B_0(I_z\cos\theta + I_x\sin\theta\cos\phi + I_y\sin\theta\sin\phi). \qquad 1.4$$

In this equation, θ and ϕ are the polar and azimuthal angles respectively, which relate the direction of the magnetic field to the principal axis system of the quadrupolar interaction.

Rf Irradiation

We also need to consider the effect of a time-dependent radio frequency (rf) magnetic field, $H_1\cos\omega t$. If the field is applied along the x-axis of the frame in which we are interested, the Hamiltonian can be written,

$$H_1 = -\gamma\hbar B_1 I_x \cos(\omega t). \qquad 1.5$$

Since the field is applied along only one axis, it is a linearly polarized rf field. This thesis doesn't deal with circularly polarized rf fields, and so they will not be discussed.

Dipolar Interaction

Another important interaction to be considered is the dipolar interaction, the interaction between two magnetic dipoles. In the principal axis system of the dipolar interaction, the Hamiltonian for two spins I_1 and I_2 is written

$$H_d = \frac{\gamma_1 \gamma_2 \hbar^2}{r^3} (A+B+C+D+E+F) \tag{1.6}$$

where

$$A = (1 - 3\cos^2\theta)\, I_{1z} I_{2z}, \tag{1.7a}$$

$$B = -\frac{1}{4}(1 - 3\cos^2\theta)\,(I_1^+ I_2^- + I_1^- I_2^+), \tag{1.7b}$$

$$C = -\frac{3}{2}\sin\theta\cos\theta\, e^{-i\phi}\,(I_1^+ I_{2z} + I_{1z} I_2^+), \tag{1.7c}$$

$$D = -\frac{3}{2}\sin\theta\cos\theta\, e^{i\phi}\,(I_1^- I_{2z} + I_{1z} I_2^-), \tag{1.7d}$$

$$E = -\frac{3}{4}\sin^2\theta\, e^{-2i\phi}\,(I_1^+ I_2^+), \tag{1.7e}$$

$$F = -\frac{3}{4}\sin^2\theta\, e^{2i\phi}\,(I_1^- I_2^-). \tag{1.7f}$$

The angles θ and ϕ relate the principal axis system of the dipolar interaction to the laboratory frame, and r is the distance between nuclei. If the nucleus of interest is dipolar-coupled to more than one nucleus, equation 1.6 is modified to consist of the sum of the corresponding dipolar interactions.

Chemical Shift Interaction

The Zeeman coupling may be altered through the screening of the nucleus by the surrounding electrons via the chemical shift interaction and may be described in a manner similar to the Zeeman coupling,

$$H_{CS} = H_O \cdot \overline{\overline{\sigma}} \cdot I, \tag{1.8}$$

where $\overline{\overline{\sigma}}$ is the shielding tensor given as

$$\overline{\overline{\sigma}} = \gamma_I \begin{pmatrix} \sigma_{xx} & \sigma_{xy} & \sigma_{xz} \\ \sigma_{yx} & \sigma_{yy} & \sigma_{yz} \\ \sigma_{zx} & \sigma_{zy} & \sigma_{zz} \end{pmatrix}. \tag{1.9}$$

Since this coupling is much smaller than the Zeeman interaction, we need only consider the secular part, that is the part which commutes with H_Z. It is then

$$H_{cs} = \gamma_I H_o \sigma_{zz} I_z. \tag{1.10}$$

We may take this tensor to be symmetric (antisymmetric parts can only contribute a second order term). There is then a coordinate system in which σ is diagonal, which we call the principal axis frame. In this frame we will term the diagonal elements σ_{11}, σ_{22} and σ_{33}

where $\sigma_{11} \leq \sigma_{22} \leq \sigma_{33}$. Since these terms are generally very small we will measure them in parts per million (ppm) of the applied field. $\Delta\sigma = \sigma_{33} - 1/2(\sigma_{11} + \sigma_{22})$ is defined to be the anisotropy of the shielding tensor, $\eta = \sigma_{11} - \sigma_{22}$ the asymmetry, and $\sigma_{iso} = 1/3\mathrm{Tr}(\sigma) = 1/3(\sigma_{11} + \sigma_{22} + \sigma_{33})$ the isotropic shift.

Two characteristic times describing the spin systems will also be used. These are T_1 and T_2, whose operational definitions will be the time required for the spin system to exchange energy with the lattice and with other spins, respectively.

Three quite different experimental techniques have been employed and I have formed natural breaks of the chapters by the experimental method used. The experiments in chapter 2 have been performed on a CW-SQUID spectrometer. The local environments of ^{14}N and ^{2}H nuclei are probed via the quadrupolar interaction. The experimental technique of ^{14}N-^{1}H cross-relaxation is discussed and applied to several systems in order to study the changes in local environments for a number of compounds, including cocaine hydrochloride. The applicability of NQR as an analytical tool is also discussed. Chapter 3 describes efforts to combine optical pumping with a pulsed SQUID spectrometer to extend the range of experiments that can be performed. While the pulsed SQUID spectrometer has been demonstrated to be very effective in studying low-frequency (<3 MHz) resonances, it is limited to systems with bulk spin densities and relatively short spin-lattice relaxation times. It is hoped that the polarization enhancement obtained from optically pumping xenon will be beneficial in studying the quadrupolar interaction on systems with low spin densities (e.g. surfaces) and/or systems with spin-lattice relaxation times that make the non-pumped experiments prohibitively long. Chapter 4 is my brief foray into the world of conventional high field NMR. The results of investigations of the structure and dynamics of a series of organometallic compounds, $HfCp_4$, $ZrCp_4$, and $SnCp_4$, are discussed.

Chapter 2 Detecting ^2H and ^{14}N using a CW SQUID spectrometer

2.1 The spectrometer

The spectrometer used for the work in this chapter has been described before[21,22], so I will not describe it in great detail. It is briefly discussed here because the unique properties of this spectrometer are exploited in order for these experiments to be carried out. A highlight of the important aspects is therefore necessary for the completeness of this work.

2.1.1 The dc SQUID[23-26]

The dc SQUID (Superconducting QUantum Interference Device) consists of a pair of Josephson junctions connected in parallel, shown schematically in Figure 2.1. The flow of bound electron pairs (which exist in the superconducting state) through the junctions are responsible for the characteristics of the SQUID.[27] A very readable explanation of

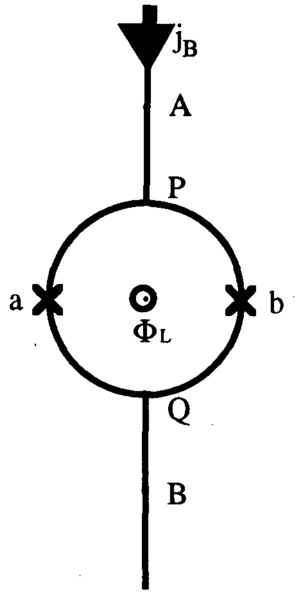

Figure 2.1 A dc SQUID consists of two Josephson junctions, a and b, connected in parallel. As electrons pairs tunnel through the junction, they acquire a phase which depends on the amount of magnetic flux threading the loop. Quantum interference between the pairs produces a periodic voltage across the SQUID which is a function of Φ_L.

superconductivity, flux trapping and quantization, and the Josephson effect is given in Chapter 21, Feynman Lectures in Physics, Volume III.[28] Junctions may be formed by inserting a thin layer of insulating material between two superconductors (used in this thesis), by a grain boundary (as is the case for high T_C SQUIDS), or by simply constricting a region of superconducting material.[24,29-32] The Josephson junctions in our SQUID were shunted with a small resistance in order to remove any hysteretic behavior. At V=0 there is a supercurrent, I_c, characteristic of the tunneling pairs. At high current ($>>I_c$) the Josephson junction is dominated by normal electrons and the resistance approaches that of the shunt resistance. When an integer flux quantum $\Phi_0=h/2e$ passes through the SQUID, the supercurrent is maximum. The supercurrent is minimized when the flux through the SQUID is a half-integer of the flux quantum as seen in figure 2.2. This is because of the phase shift caused by the induced current in the SQUID loop. This periodic behavior can be easily seen by biasing the SQUID at a current, I_b, greater than I_c. This causes a variation in the voltage across the SQUID that is a periodic function of flux (Figure 2.3).

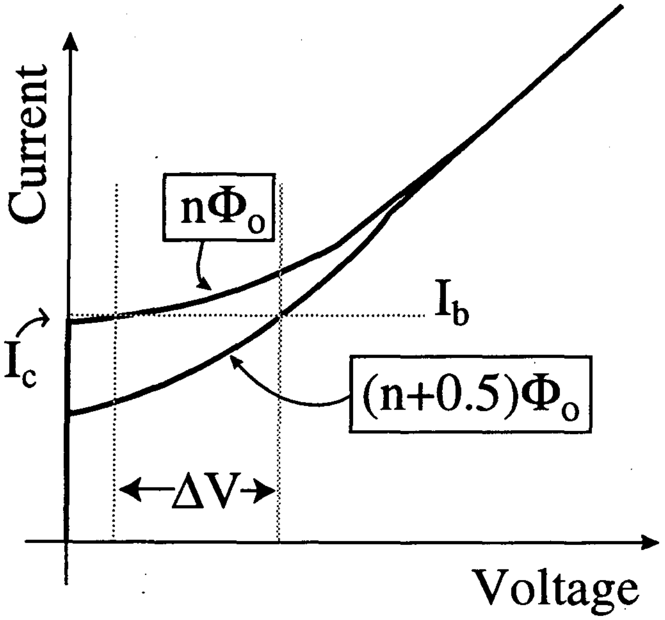

Figure 2.2 Current versus voltage characteristic of the dc SQUID.

The period is the flux quantum, Φo.

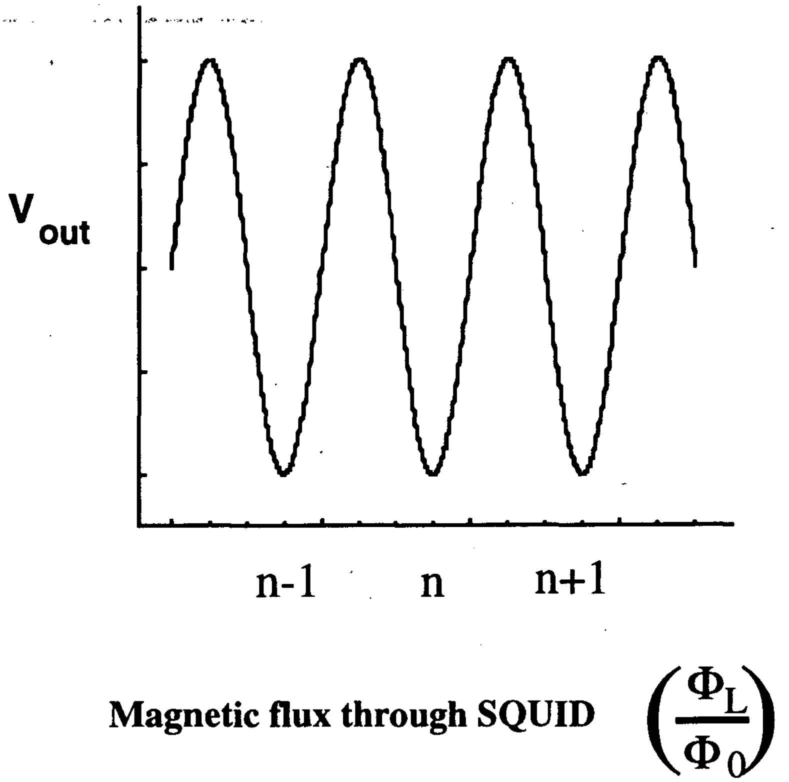

Figure 2.3 A V-Φ curve. The averaged voltage is a function of the magnetic flux threading the SQUID due to the quantum interference of the supercurrent through the two Josephson junctions.

The dependence of voltage on flux can be seen from the following equations. The supercurrents that flow through the junctions a and b will acquire a phase due to both the Josephson junction and the vector potential, A, of the magnetic field.

$$\Delta\phi_a(t) = \Delta_a(t) + \frac{2e}{\hbar c}\int_P^Q A ds, \qquad 2.1a$$

$$\Delta\phi_b(t) = \Delta_b(t) + \frac{2e}{\hbar c}\int_P^Q A ds. \qquad 2.1b$$

Because the current must be single valued we know that

$$\Delta\phi_b(t) - \Delta\phi_a(t) = 2\pi n. \qquad 2.2$$

For simplification we will set $n=0$. Thus

$$\Delta_b(t) - \Delta_a(t) = \frac{2e}{\hbar c} \oint A\, ds = \frac{2e}{\hbar c} \Phi_L, \tag{2.3}$$

where Φ_L is the flux penetrating the loop. We combine equations 2.2 and 2.3 to give

$$\Delta\phi_a'(t) = \Delta_a(t) - \frac{e}{\hbar c} \Phi_L, \tag{2.4a}$$

$$\Delta\phi_b'(t) = \Delta_b(t) + \frac{e}{\hbar c} \Phi_L. \tag{2.4b}$$

The total supercurrent, j_s, will then be

$$j_s = j_{sa} \sin(\Delta\phi_a'(t)) + j_{sb} \sin(\Delta\phi_b'(t)) \tag{2.5}$$

where j_{sa} and j_{sb} are the maximum supercurrents going through each half of the SQUID. For simplification we will assume that the two junctions are equivalent so that $j_{sa} = j_{sb} = j_{s0}$ and $\Delta_a(t) = \Delta_b(t) = \Delta(t)$. Thus

$$\begin{aligned} j_s &= j_{s0} \sin(\Delta(t) - \frac{e}{\hbar c} \phi) + j_{s0} \sin(\Delta(t) + \frac{e}{\hbar c} \Phi_L) \\ &= 2j_{s0} \sin(\Delta(t)) \cos(\frac{e}{\hbar c} \Phi_L). \end{aligned} \tag{2.6}$$

Therefore the supercurrent is a sinusoidal function of the magnetic flux.

The voltage, $V(t)$, across the SQUID is related to the normal current (the difference between the bias current and the supercurrent so long as $j_b > 2j_{s0}$):

$$V(t) = R(j_b - 2j_{s0} \sin(\Delta(t)) \cos(\frac{e}{\hbar c} \Phi_L)). \tag{2.7}$$

It is important to note that $\Delta(t)$ is a function of the voltage and oscillates at a very high frequency. In our dc SQUID spectrometer, a junction is biased by several microvolts giving oscillations in the gigahertz range. However, a narrowband detector will only observe the time averaged voltage.

The time averaged voltage can be calculated by examining the change in phase with respect to time across a Josephson junction. It can be shown that a variation of the phase with time can be described by

$$\frac{\partial\delta}{\partial t}=\frac{2eV}{\hbar}. \qquad 2.8$$

Rearranging to find the period, T, of one oscillation gives

$$\begin{aligned}T&=\int_0^T dt=\frac{\hbar}{2e}\int_0^{2\pi}\frac{d\delta(t)}{V(t)}\\&=\frac{\hbar}{2e}\int_0^{2\pi}\frac{d\delta(t)}{R\left(j_b(t)-2j_{s0}\sin(\delta(t))\cos\left(\frac{e}{\hbar c}\Phi_L\right)\right)}\end{aligned} \qquad 2.9$$

We can also calculate the time averaged value of the voltage over one period as

$$V=\frac{1}{T}\int V(t)dt=\frac{\hbar}{2eT}\int\frac{d\delta(t)}{dt}dt=\frac{\hbar}{2eT}2\pi. \qquad 2.10$$

Combining equations 2.9 and 2.10 gives

$$V=\frac{\hbar}{2e}2\pi\frac{2eR}{\hbar}\left(\int\frac{d\delta(t)}{\left(j_b(t)-2j_{s0}\sin(\delta(t))\cos\left(\frac{e}{\hbar c}\Phi_L\right)\right)}\right)^{-1}. \qquad 2.11$$

Which upon evaluation of the integral leaves

$$V=R\sqrt{j_b^2-\left(2j_{s0}\cos\left(\frac{e}{\hbar c}\Phi_L\right)\right)^2}. \qquad 2.12$$

Therefore, the time averaged voltage is also a function of the magnetic flux penetrating the SQUID. Figure 2.3 plots the voltage dependence of the magnetic flux.

2.1.2 The Probe

The SQUID as a null detector

The SQUID can be used as a detector in several different ways. If the changes in magnetic flux are much greater than a single flux quantum, it is possible to count the number of oscillations in the voltage to obtain the number of flux quanta in the signal. If the changes in magnetic flux are much smaller than a single flux quantum, the SQUID can be operated on the maximum slope of the flux versus voltage curve. For small changes in flux, the voltage change will be a linear function of flux. Another alternative is to operate the SQUID as a null detector in a negative feedback loop[33] (see Figure 2.4). The magnetic flux through the SQUID remains constant and the size of the signal in terms of number of flux quanta is no longer an issue as long as the electronics can react fast enough to keep the level constant. The negative feedback scheme has the advantage of continuously operating in a regime where the output voltage is directly proportional to the flux. Because the SQUID detector does not have a frequency dependence, the detection of low-frequency

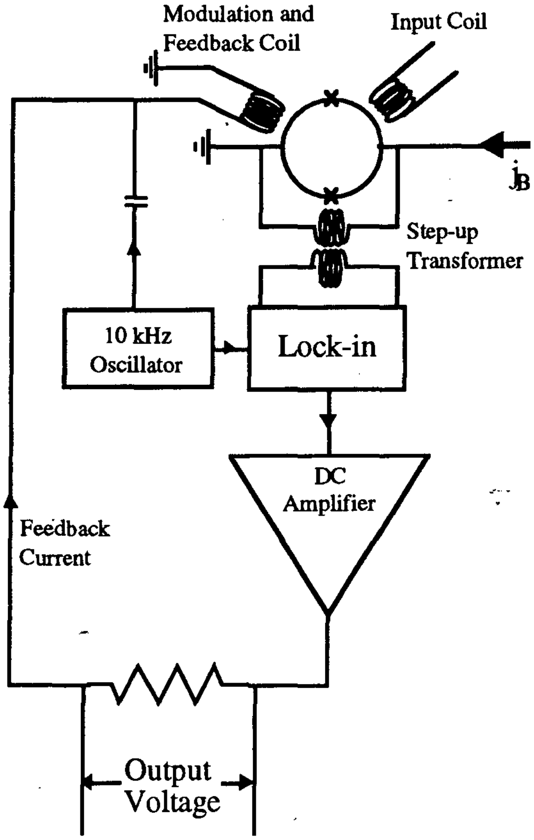

Figure 2.4 Circuit for SQUID detection scheme including the modulation and feedback coil.

resonances is better than with standard NMR and NQR techniques. Standard NMR and NQR techniques use a Faraday detector which measures the changes in the oscillating magnetic flux as a function of time ($d\Phi/dt$), which is frequency dependent.

Frequency modulation

One problem with detecting at low frequencies (close to dc) is that the system's noise power has a 1/f characteristic which dominates at low frequencies[34]. Since the change in magnetization of our sample typically occurs over several seconds, the frequencies that we wish to detect are very close to dc. This is dealt with by frequency modulation[35]. The low frequency signal is mixed with a carrier wave, which is a signal of higher frequency. The signal is detected at this higher frequency with only characteristic white noise. The frequency modulation is limited by stray reactances in the detection and feedback circuits. This is not a problem for us since the signals are always near dc.

Flux Transformer

Now we consider the problem of coupling the flux we want to measure into the SQUID. The most straightforward arrangement would be to place the sample directly into the SQUID loop[36]. There are several problems with this idea, however. The SQUID used in the experiments in this chapter is hermetically sealed. Also, because modern SQUIDs are on the order of micrometers in size, the size of the sample must be very small. Additionally, the application of magnetic fields across the tunnel junctions suppresses the critical current, although some new recent designs have been effective in reducing this problem.[37] Other factors to take into consideration is that samples are not easily changed, and that the sample must stay at the same temperature as the SQUID. If the sample is moved some distance out of the loop, then several of these factors are mitigated. A new development in the Clarke group has been the construction of a microscope with a SQUID located approximately 50 μm from a room temperature sample. Plans are underway to construct a similar instrument to do NQR experiments on small (<1 mg) samples.

An alternative solution is to use a flux transformer to couple flux generated from a larger sample to the SQUID. This is the method employed in the CW-SQUID system. While all the SQUID experiments done in this chapter are conducted at liquid helium temperatures (4.2 K), it is possible to construct a probe in which the sample is maintained at a different temperature than the SQUID[38]. The circuit consists of two superconducting coils made from a single piece of superconducting wire. One coil surrounds the sample and the other is inductively coupled to the SQUID. A change in sample magnetization produces a change in magnetic flux through the pickup coil. According to the BCS theory of superconductivity, the flux through a superconducting coil is constant. This means that a supercurrent is generated in the wire to oppose the change in flux in the coil which is inductively coupled to the SQUID. The magnetic flux generated in the pickup coil by a sample of magnetization, M, is

$$\Phi_p = 4\pi^2 f r_p^2 N_p M \tag{2.13}$$

where f is the filling factor, r_p is the radius of the pickup coil, and N_p is the number of turns in the pickup coil. This magnetic flux will induce a current in the superconducting circuit of

$$I_p = \frac{\Phi_p}{(l_s + l_p)}, \tag{2.14}$$

where l_s and l_p are the inductances of the coil around the SQUID and the pickup coil, respectively. The amount of flux ultimately coupled into the SQUID depends on the mutual inductance between the coupling coil and the SQUID, M_{cs}, as given by

$$\Phi_s = I_p M_{cs} = \frac{M_{cs}}{(l_p + l_s)} * (4\pi^2 f r_p^2 N_p M). \tag{2.15}$$

It has been shown previously that the maximum signal is achieved when $l_p = l_s$ for a given sample size[34]. For the spectrometer I am currently describing $l_s = 2\mu H$, so the pickup coil has been wound to produce an inductance of $2\mu H$.

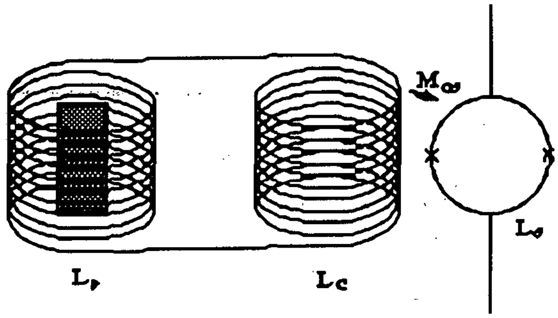

Figure 2.5 Schematic of the flux transformer used to couple the signal from the sample into the SQUID. A supercurrent is generated in response to a change in magnetic flux in the sample. This produces a change in flux in the coil inductively coupled to the SQUID.

2.1.3 Spectrometer overview

As depicted in Figure 2.6, the 0.6 cm diameter pickup coil is supported on a macor form and is made of 14 turns of NbTi wire which is superconducting at liquid helium temperatures. Surrounding the pickup coil is a second form which contains two Helmholz rf coils, designed to provide two channels of rf irradiation for the experiments. These two coils are orthogonal to each other and the pickup coil. It has, however, proved more practical to mix two channels in the frequency synthesizer and send them through a single rf coil. This is because the rf tolerance of the system varies according to which channel we use. The "rf tolerance" is the maximum amount of rf irradiation that we can apply and still maintain a functioning SQUID system. We can maximize the rf tolerance for one channel or settle for a significantly smaller rf tolerance for the two channels. The programmable frequency sweeper (Hewlett-Packard 3326A Two Channel Synthesizer) can provide two separate rf channels for frequency sweeps up to 13 MHz at an output level of up to 10 V with sweep times varying from 1 ms to 1000 s.

Because the rf field is on during detection and can never be made completely orthogonal to the pickup coil, a low pass filter is used to eliminate the rf that is coupled into the pickup coil[39,40]. The filter eliminates rf that is coupled into the SQUID at the expense of injecting additional noise into the system. This places a lower limit on the frequency of rf irradiation that can be used of approximately 100 kHz. Lowering the cutoff frequency would allow us to study resonances that are lower in frequency. However, an unacceptable level of noise would be injected into the SQUID.

For NMR applications, a static magnetic field is required in order to carry out experiments. In fact, a static magnetic field is necessary for the NQR experiments performed on this spectrometer as well. The magnetic moment of integer spin nuclei is quenched in zero magnetic field. Therefore, a field is required to induce a nuclear magnetic moment. Additionally in this thesis, signals from ^{14}N can be observed by their effect on adjacent protons, which have a magnetic moment. For odd half-integer spin, which are not discussed in this work, the quadrupolar transitions are degenerate and a small magnetic field is a necessary perturbation to observe a spectrum. A small dc field is generated by passing current through a copper solenoid wound around a lead tube in the non-superconducting state. The probe is then cooled below the critical temperature of lead, the field is trapped, and the current is turned off. The field can be changed by warming the probe above the critical temperature of lead, applying a new current through the copper coil, and returning the probe to the liquid helium bath.

The dc SQUID (BTi Model DP probe with Model DSQ DC Hybrid SQUID) is hermetically sealed inside a niobium shield. The pickup coil leads can be attached to the coupling coil of the SQUID via two screws tapped into a niobium block. The SQUID is connected to a room temperature feedback controller (BTi Model 400). The signal from the SQUID is passed through the feedback unit to the SQUID controller (BTi Model 40) where it is amplified (x1, x10, x100, x1000) and filtered (5 or 50 kHz bandwidth). That signal is then sent through a home built low-pass filter with a bandwidth from 200 to 0.02 Hz and a variable gain from 10 to 120. It is then transmitted into an AT clone computer through a digital oscilloscope (Rapid Systems Model R1000). The spectra can be stored and analyzed on the computer (see Figure 2.7).

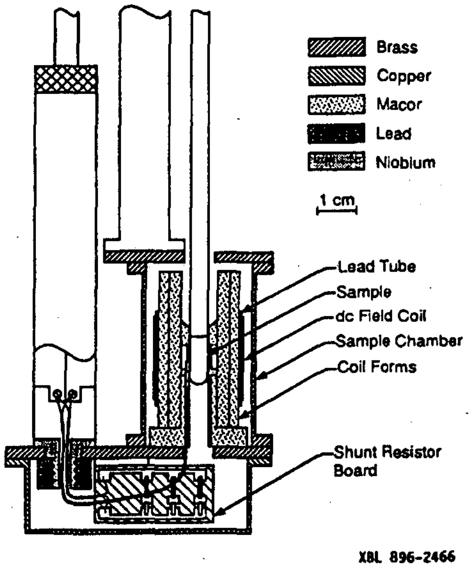

Figure 2.6 Cross-section of the cw-SQUID probe. The dc SQUID is on the left hand side.

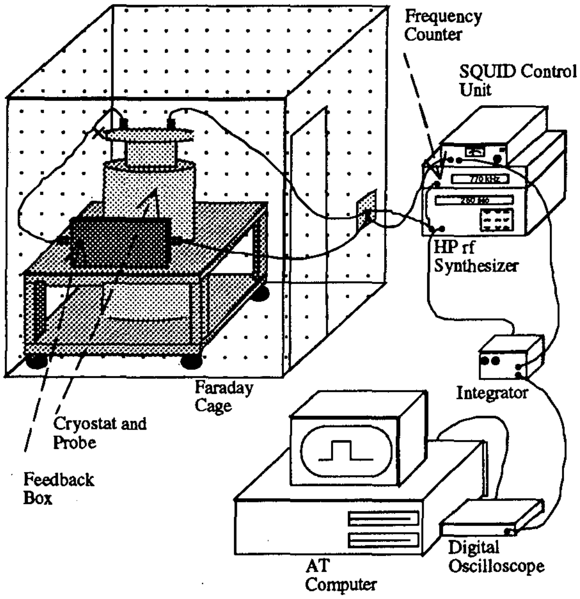

Figure 2.7 An overview of the cw-dc SQUID spectrometer system.

2.2 The Quadrupolar Interaction

The quadrupolar interaction can be used as a structural probe of the local nuclear environment. It is sensitive to the distribution of bonds between the quadrupolar nucleus and its neighbors. Specifically, it is the interaction of the electric quadrupole moment of a nucleus with the electric field gradient that is generated by an asymmetric charge distribution surrounding the nuclei[41]. While the asymmetric charge distribution arises primarily from the bonds, it can also result from defects in the lattice, intermolecular packing, and grain boundaries. In fact, if the sensitivity of NQR can be enhanced, it should prove to be a powerful tool in the study of surfaces. This is due to the fact that the field gradients at surfaces and interfaces should vary greatly from that of the bulk. Experiments to this end are in progress. If a transfer of polarization from highly polarized optically pumped ^{129}Xe to other, less abundant spin species can be accomplished and be detected with a SQUID, it may be possible to probe the local structure of surfaces using NQR. Preliminary steps to these experiments have been taken are outlined in Chapter 3.

The electric field gradient at the origin of a set of Cartesian axes may be represented by a Cartesian tensor, **V**, whose *ij*th element is given by

$$V_{ij} = \int \frac{\partial^2}{\partial x_i \partial x_j}\left(\frac{\rho(\mathbf{r})}{r}\right) d\tau \qquad 2.16$$

where $\rho(\mathbf{r})$ is the charge density at a point **r** relative to the origin. This means that the electric field at the nucleus is produced entirely by charges wholly external to the nucleus.

The tensor is symmetric and is diagonal in a suitable set of axes known as the principal axes, which are labeled according to the convention $|V_{zz}| \geq |V_{yy}| \geq |V_{xx}|$. As the tensor is also traceless[42], the corresponding diagonal elements (the eigenvalues) sum to zero. The field gradient can therefore be completely specified by the orientation of the principal axes and two parameters derived from the diagonal elements in the principal axis system. These parameters are taken to be the "principal value", V_{zz}, and the "asymmetry parameter", $\eta=(V_{xx} - V_{yy})/ V_{zz}$, which lies in the region from 0 to 1.

The Hamiltonian that describes the interaction between an electric quadrupole moment and the electric field gradient is given by

$$H_Q = \frac{eQ}{6I(2I-1)\hbar}\sum_j [3I_j^2 - I^2], \qquad 2.17$$

which, when combined with the Laplace equation $\Sigma V_{ii} = 0$ gives

$$H_Q = \frac{e^2qQ}{4I(2I-1)} \; [3I_z^2 - I^2 + \frac{\eta}{2}(I_+^2 + I_-^2) \;]. \qquad 2.18$$

Thus, the quadrupolar interaction can be characterized by two parameters: C_q, which is defined as the quadrupole coupling constant e^2qQ/h, characterizes the strength of the interaction; η characterizes the asymmetry of the electric field gradient.

Recently, simulations from first principles to calculate the electric field gradient have been introduced and can provide a physical insight into the origin of the electric field gradient.[43] The precision of these calculations is still not good enough to be able to make quantitative predications. However, the magnitudes of the parameters give us a qualitative insight to deviations from expected lattice symmetry. No effort has been made to compare experimentally determined parameters with theoretical predictions.

If $\eta = 0$, then the z-axis has at least C_3 symmetry. An example of C_3 symmetry is shown in figure 2.8. This figure shows the configuration of an isolated CNH_3^+ group and the principal axis. Theoretically, this is the case for terminal nitrogens in amino acids and peptides, both of which exist as zwitterions. In reality, inter- and intramolecular interactions create appreciable inequivalence between the three N-H bonds.[44] If there are two perpendicular C_3 axes, then $V_{zz} = V_{xx} = V_{yy} = 0$ and the electric field gradient vanishes. Another way of saying this is that the field gradient is isotropic and the principal axes and η are undefined. If $\eta=1$, then $V_{xx} = 0$ and the electric field gradient is limited to the zy-plane with the symmetry of the color group C_4.

The electric quadrupole moments of most nuclei typically vary over only two orders of magnitude. However, C_q can range from zero to hundreds of megahertz. This variation is determined by the polarizability of the electron cloud surrounding the nucleus and paramagnetic atoms.[45] Because of this wide range in frequency, the size of the interaction with respect to other interactions determine the manner in which the quadrupolar interaction is studied.

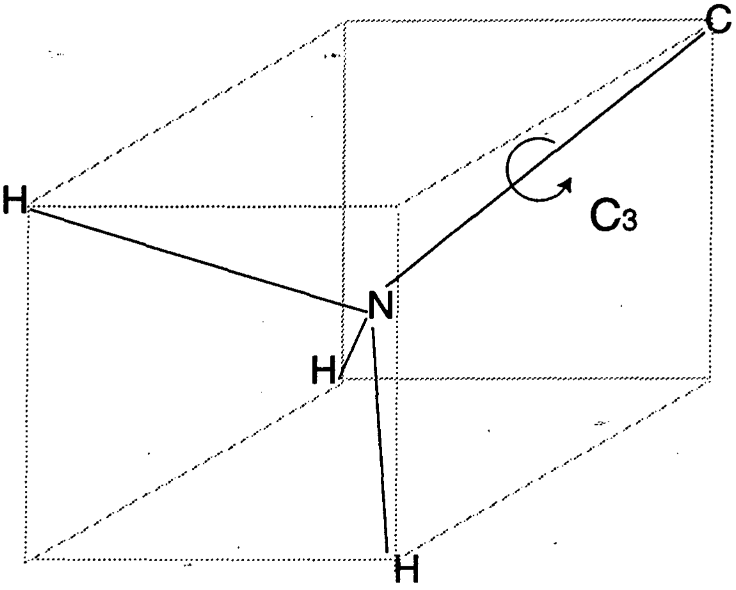

Figure 2.8 The configuration of an isolated CNH_3^+ group showing the principal axis.

Case I. $\omega_z >> \omega_q$[46]

Historically, this is the case for small quadrupole moments and/or near cubic symmetry. In the last 10 years, new high field NMR experiments such as Dynamic Angle Spinning (DAS)[7,47] and DOuble Rotation (DOR)[8,48,49] have been developed that extend the measured range of quadrupole coupling constants that are able to be measured. Currently, $C_q*4I(2I-1)$ has an upper limit of approximately 20 MHz for odd half-integer spin nuclei. These techniques rely on the selective excitation of the central transition (1/2 -> -1/2). The quadrupolar information is contained in the second-order quadrupolar broadening effects. Information is extracted by simulating the lineshape of the central transition and determining which parameters give the best fit. There is, however, no central transition for spin I=1 nuclei. Therefore, in order to study the quadrupolar broadening, one must excite the entire quadrupolar interaction. Typical excitations for current hardware typically limit the spectral width to less than 200 kHz. Therefore, while it is often possible to extract information on integer spin nuclei whose C_q are small, this severely restricts the number of compounds available for investigation. Deuterium, because of the typically small size of its C_q, has been the subject of many investigations.[50] The application of high-field NMR to ^{14}N, whose interactions in general are much larger and range from 0-6 MHz, has been very limited.

Case II. $\omega_q >> \omega_z$

Conventional pure NQR falls into this case. Pure NQR is carried out in the absence of a magnetic field. Unfortunately, standard techniques suffer when trying to measure low-frequency resonances. Most spectrometers employ a Faraday detector, a coil which measures the voltage produced by the Faraday effect as the transverse magnetization oscillates after rf irradiation at the resonance frequency. The sensitivity of the Faraday effect is proportional to the rate of change in magnetization ($d\Phi/dt$). Thus, the voltage decreases linearly with frequency. For quadrupole resonances below 3 MHz, these experiments become difficult due to the small amplitude of the signal, although several systems that are capable to measuring to < 1 MHz have been developed.[17,18] These methods tend to require brute force techniques of large numbers of averages and/or large sample volumes. Field cycling is a technique that has successfully been used to measure low-frequency resonances[19,20]. Spins are polarized in a high magnetic field, adiabatically demagnetized, irradiated at a specific frequency, and adiabatically remagnetized for detection. However, this is inherently a point-by-point technique.

This is also the regime where the NQR is carried out with the cw-SQUID spectrometer for the ^{14}N experiments that will be described in Section 2.5[4,51,52]. The applied magnetic field is necessary for cross-relaxation between the nitrogen nuclei and the protons. The fields that are used for the experiments in this chapter (50-200 Gauss) barely perturb the quadrupolar energy levels of ^{14}N. (Figure 2.9) The effect of the applied field can be corrected analytically[53].

Case III. $\omega_q \sim \omega_z$

In this case, a perturbation treatment is useless. Therefore, the Hamiltonian that describes this regime is the combination of the Zeeman plus the quadrupolar Hamiltonians. For spin I=1 nuclei, which are the nuclei dealt with in this chapter, the transition frequencies can be calculated analytically.[53] The computer program Specsim that was used to determine quadrupole coupling constants and asymmetry parameters in the presence of a magnetic field is found in Appendix 1. Section 2.5 illustrates the effect that the application of a magnetic field has on the quadrupole energy levels for deuterated hexanoic acid, $CH_3CD_2CD_2CD_2CD_2CO_2D$.

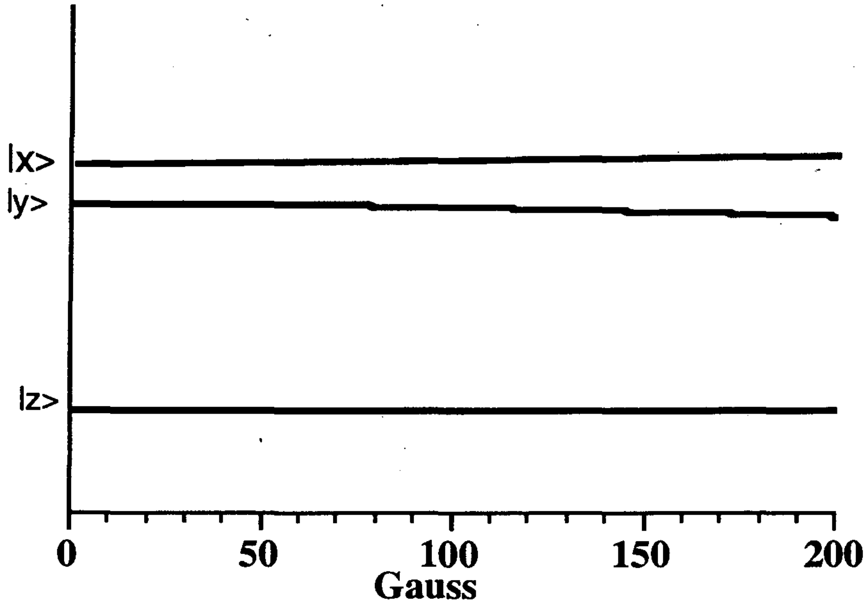

Figure 2.9 Effect of applied magnetic field on the quadrupolar eigenstates in the range of applied fields for the cw SQUID spectrometer. The magnetic field barely perturbs the energy levels. These perturbations can be calculated analytically and the spectrum corrected.

2.3 Z-axis cw magnetization

The simplest magnetic resonance experiment that can be performed on the cw SQUID spectrometer is simply to sweep an rf field through the resonance frequency of a two level system and monitor the change in longitudinal magnetization of the spin system[54]. A two-level energy-level diagram for a spin I = 1/2 nucleus in a magnetic field with energy splitting $\hbar\omega_z$ is shown in figure 2.10. The change in longitudinal magnetization is a result of the change in the populations of the two energy levels. The populations at thermal equilibrium are given by the Boltzmann distribution. Under our experimental conditions the ratio $\hbar\omega_o/kt$ is very small. Therefore, using the high-temperature approximation, the exponential is truncated to only the first term in the expansion.

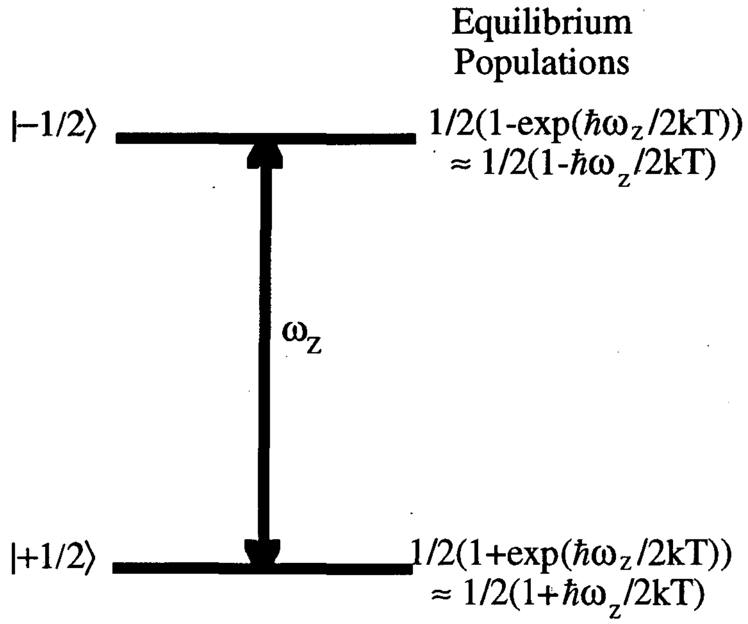

Figure 2.10 Energy level diagram and equilibrium populations of a spin-1/2 nucleus in a magnetic field, $B_0 = \omega_z/h\gamma$.

At thermal equilibrium, the longitudinal magnetization can be calculated by summing the products of populations of each level by its respective I_z value.

$$M_z = N\gamma\hbar \sum_i (P_i I_{zi}) \qquad 2.19$$

where N is the number density of spins. For the case of spin I = 1/2 nuclei,

$$M_z = \frac{N\gamma\hbar^2\omega_z}{4kT}. \qquad 2.20$$

This magnetization produces a fixed dc output from the SQUID. As an rf field is swept through resonance, the populations of the two levels equalize, or saturate. If the resonance is completely saturated (i.e. the rf field adds energy to the spin system faster than it can be dissipated by heat leaks to the lattice), the magnetization is destroyed. Therefore the net change in magnetization is simply M_z. An idealized spectrum for a single crystal, isolated, spin I = 1/2 nuclei in a magnetic field with no relaxation effects is shown in figure 2.11. Note that the spectrum looks like a step function, as the output of the SQUID changes from one level to another at resonance. In practice, powder averages[42], dipolar couplings[55], spin diffusion[56,57], and spin-lattice relaxation[21] distort this shape. Forward (low to high frequency) and reverse (high to low frequency) sweeps are combined to remove experimental artifacts that may be present in the spectrum.

This is the also the spectrometer response to the ^{14}N quadrupole transition frequencies that are observed. Because the magnetic moment of spin I=1 nuclei is quenched in zero field, and the application of a small applied field is unable to induce a sufficient magnetic moment, we observe the nitrogen transition via its effect on the proton system. In the deuterium system, the quadrupolar levels are mixed strongly by the application of a Zeeman field and therefore, have sufficient magnetic moment to be detected directly. Excitation of a single transition can be described in the same formalism as a two-level system.

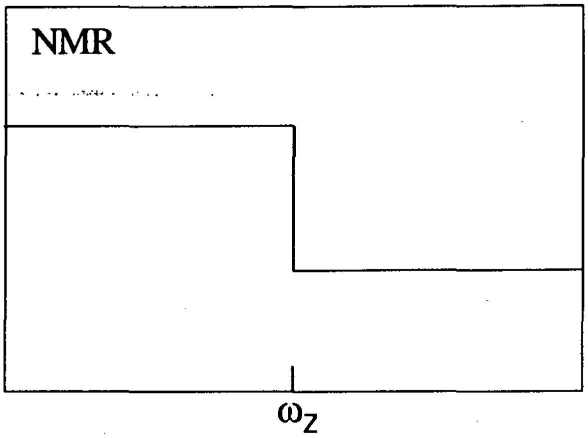

Figure 2.11 Idealized NMR spectrum from the cw SQUID spectrometer.

The spin I=1 problem

Non-degenerate states have a vanishing magnetic moment in zero magnetic field[20]. Since these states have no z-axis magnetization any transition between the quadrupolar levels will result in no net change of sample magnetization and therefore no signal detected. This can be seen through the calculation of eigenvalues and eigenstates from the quadrupolar Hamiltonian

$$H_Q = \frac{e^2qQ}{4I(2I-1)} \left[3I_z^2 - I^2 + \frac{\eta}{2}(I_+^2 + I_-^2)\right]. \qquad 2.21$$

For I = 1, the eigenstates are

$$|x> = \frac{1}{\sqrt{2}}(|+1> + |-1>), \qquad 2.22a$$

$$|y> = \frac{1}{\sqrt{2}}(|+1> - |-1>), \qquad 2.22b$$

$$|z> = 0, \qquad 2.22c$$

with eigenvalues

$$\frac{hC_Q}{4}(1 + \eta), \qquad 2.23a$$

$$\frac{hC_Q}{4}(1 - \eta), \qquad 2.23b$$

$$-\frac{hC_Q}{2}, \qquad 2.23c$$

respectively, where $C_Q = \frac{e^2qQ}{h}$. This leads to three transitions

$$\nu_+ = \frac{C_Q}{4}(3 + \eta), \qquad 2.24a$$

$$\nu_- = \frac{C_Q}{4}(3 - \eta), \qquad 2.24b$$

$$\nu_0 = \frac{C_Q}{2}\eta. \qquad 2.24c$$

The corresponding energy level diagram is given in figure 2.12. Note that all three eigenstates have no magnetic moment (i.e. $<\Psi^*|I_z|\Psi> = 0$). A magnetic field resulting in a Zeeman splitting on the order of the asymmetry splitting is sufficient to induce a detectable magnetic moment, but those fields are large enough to significantly distort the spectrum making the quadrupolar information difficult to extract. In the case of ^{14}N, the required field is too large to be applied with the current experimental apparatus. Another, very elegant way of demonstrating the vanishing magnetic moment by using group theory and time reversal symmetry is given in Bruce Black's thesis[58]. Because of the difficulties in directly detecting ^{14}N resonances, indirect detection will be discussed in section 2.5.

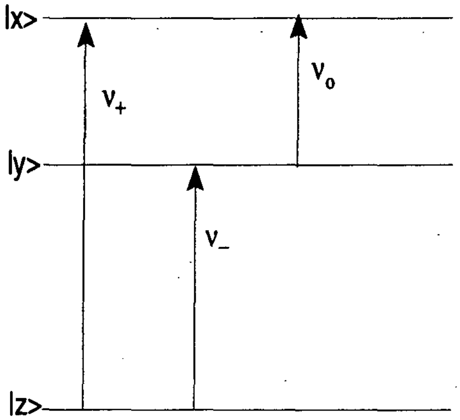

Figure 2.12 Energy level diagram for a spin I=1 system with non-degenerate eigenstates.

2.4 Direct detection of deuterium quadrupolar nuclei

It has previously been shown that direct detection of spin I=1 quadrupole transitions have been measured for degenerate eigenstates (|x> = |y>) by the cw SQUID spectrometer.[58] Another way of stating this is that it is possible to detect quadrupole resonances when $\eta = 0$ (or at least very close to zero). This was demonstrated with α-N2 which has an η with an upper limit of $\eta < 0.00016$.[59] In this case, the application of a perturbing static magnetic field lifts the degeneracy in a manner similar to work done on odd half-integer spin nuclei with the cw SQUID spectrometer.[21,22,58]

It is possible to apply a larger magnetic field to break the time reversal symmetry and induce a magnetic moment to directly detect deuterium resonances from non-degenerate eigenstates. Because the effect of a magnetic field on spin I=1 quadrupolar eigenstates can be calculated analytically[53], it is possible to extract the quadrupolar information.

In order to study the effect of an applied magnetic field on the quadrupolar eigenstates, we begin by constructing the eigenstates for a Hamiltonian consisting of the quadrupolar and the Zeeman interactions. We will deal with the simplest case, a single crystal with the principal axis aligned along the static magnetic field:

$$H_Q + H_z = \frac{e^2qQ}{4I(2I-1)}[3I_z{}^2 - I^2 + \frac{\eta}{2}(I_+^2 + I_-^2)] - \gamma \hbar I_z B_0. \qquad 2.25$$

Diagonalizing this matrix

$$\begin{bmatrix} \frac{C_Q}{4} - \gamma B_o & 0 & \eta\frac{C_Q}{4} \\ 0 & -\frac{C_Q}{2} & 0 \\ \eta\frac{C_Q}{4} & 0 & \frac{C_Q}{4} + \gamma B_o \end{bmatrix} \qquad 2.26$$

yields eigenvalues of

$$E_x = \frac{C_Q + \sqrt{16B_o^2\gamma^2 + \eta^2 C_Q{}^2}}{4}, \qquad 2.27a$$

$$Ey = \frac{C_Q - \sqrt{16B_o^2\gamma^2 + \eta^2 C_Q{}^2}}{4}, \qquad 2.27b$$

$$Ez = \frac{-C_Q}{2}. \qquad 2.27c$$

Figure 2.13 illustrates the effect of an applied magnetic field on the quadrupolar energy levels for a deuterium nucleus. In order to calculate the magnetic moment, we define a quantity

$$f = \frac{\gamma B_0}{\frac{e^2 qQ\eta}{4h}}, \qquad 2.28$$

and rewrite the eigenvalues as[60]

$$E_x = \frac{C_Q}{4}[1 + \eta(1 + f^2)^{1/2}], \qquad 2.27a'$$

$$E_y = \frac{C_Q}{4}[1 - \eta(1 + f^2)^{1/2}], \qquad 2.27b'$$

$$E_z = \frac{-C_Q}{2}, \qquad 2.27c'$$

with eigenstates

$$|x\rangle = \cos\theta|+1\rangle + \sin\theta|-1\rangle, \qquad 2.29a$$

$$|y\rangle = \sin\theta|+1\rangle - \cos\theta|-1\rangle, \qquad 2.29b$$

$$|z\rangle = |0\rangle, \qquad 2.29c$$

where

$$\cos\theta = \frac{1}{\sqrt{2}}[1 + f^2 + f(1 + f^2)^{1/2}]^{-1/2}, \qquad 2.30a$$

$$\sin\theta = \frac{1}{\sqrt{2}}[1 + f^2 - f(1 + f^2)^{1/2}]^{-1/2}. \qquad 2.30b$$

The Zeeman field mixes the $|+1>$ and $|-1>$ eigenstates and the magnetic moment is no longer zero. If we calculate the expectation values of the wavefunctions we find that

$$\langle I_x\rangle = \langle I_y\rangle = 0, \qquad 2.31a$$

$$\langle z|I_z|z\rangle = 0, \qquad 2.31b$$

and

$$\langle x|I_z|x\rangle = -\langle y|I_z|y\rangle = -\frac{f}{(1 + f^2)^{1/2}} = -F(f). \qquad 2.32$$

This factor, F(f), is the magnetic moment of the |x⟩ and |y⟩ states. This is what the SQUID will measure when a nucleus is excited from, for example, the |z⟩ to the |x⟩ state. Figure 2.14 shows the deuterium resonances at 157 kHz and 200 kHz. The location of these resonances shift with applied magnetic field. This spectrum is a combination of four forward and four reverse sweeps. Because the SQUID was not very stable when this sample was run, the spectrum shows "flux jumps', where the SQUID temporarily loses lock. These flux jumps are distinguishable as single data points above the ouput level of the SQUID since the sample magnetization changes much slower than the time required to take a single data point. There appear to be many of them in this spectrum because eight scans have been combined and the flux jumps from all of the scans appear in the spectrum. Figure 2.15 is a plot of resonance frequency versus magnetic field. The closed circles represent the frequencies obtained from the spectra, while the open circles represent the calculations of resonances with a quadrupole coupling constant of 184 kHz and η of 0.17.

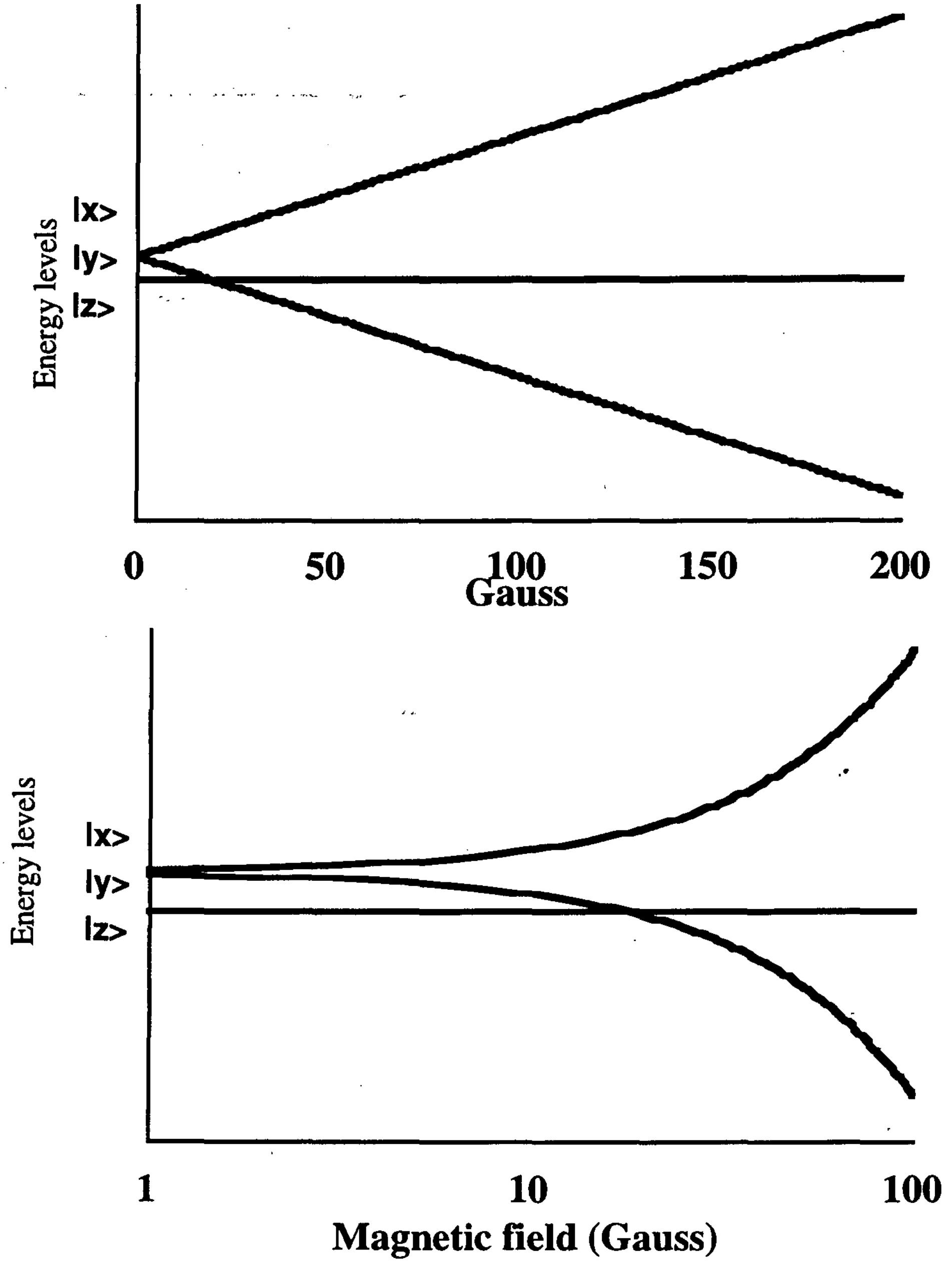

Figure 2.13 Quadrupolar eigenstates becoming more distorted by the application of a static magnetic field. The bottom figure is a semi-log plot of the beginning of the top curve.

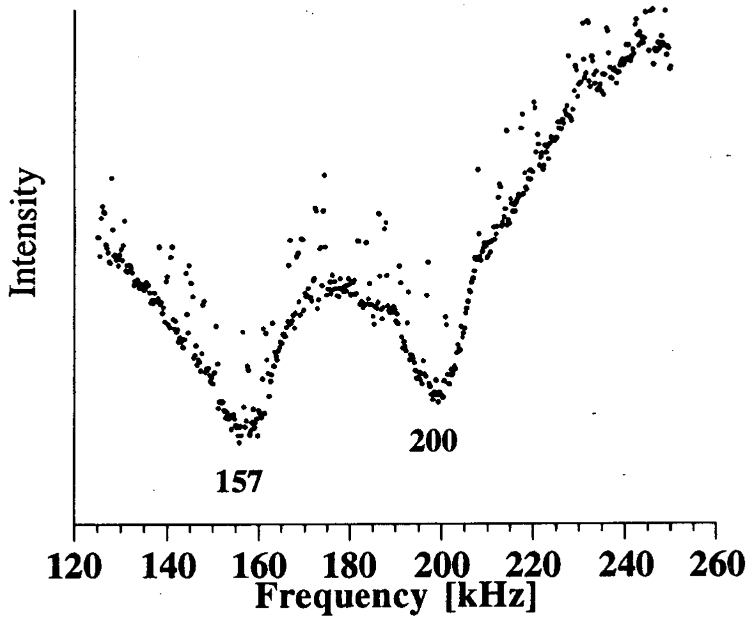

Figure 2.14 Representative spectrum of deuterium quadrupole mixed with Zeeman resonances.

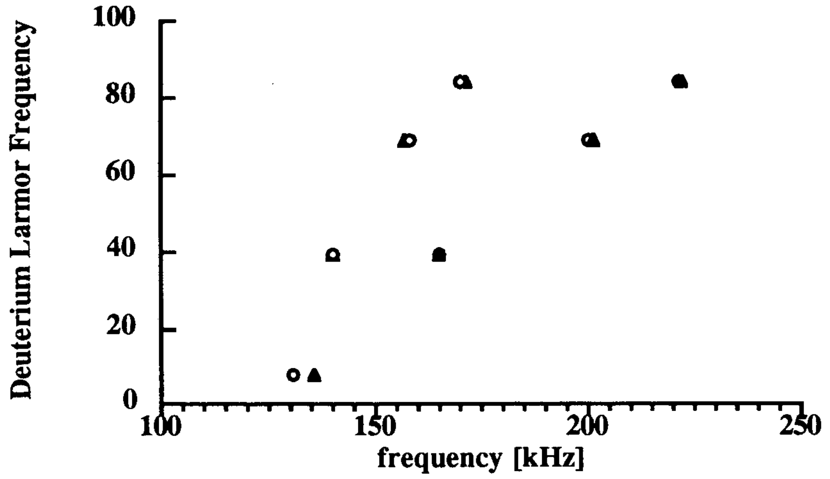

Figure 2.15 Magnetic field versus deuterium frequency. The closed circles represent frequencies obtained experimentally. The open circles are from a simulation based on an η of 0.17 and C_q of 184 kHz.

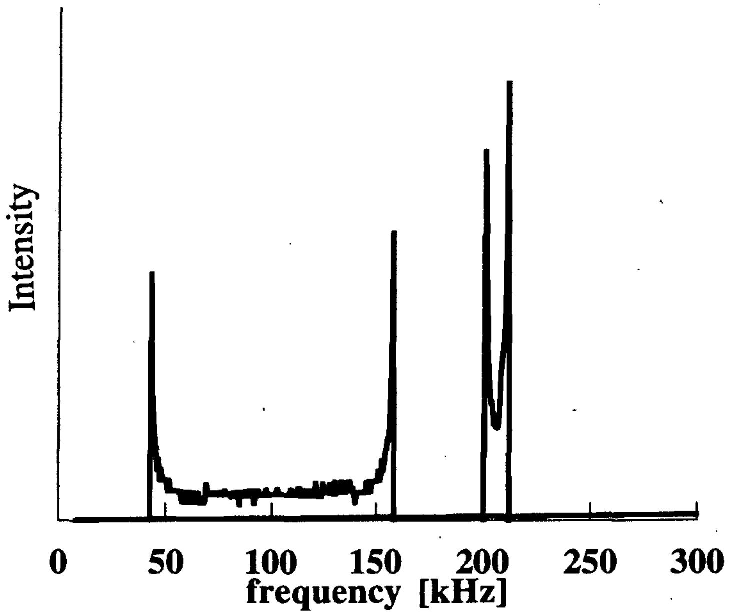

Figure 2.16 Simulation of deuterium spectrum for $\eta = 0.17$ and $C_q = 184$ kHz. The spectrum is broadened by a distribution of crystallites.

2.5 ^{14}N cross-relaxation

2.5.1 Introduction

It has been shown previously that ^{14}N signals are able to be observed directly with the application of a small static magnetic field when $\eta = 0$ (or very close to zero). The static magnetic field breaks the degeneracy of the $|+1>$ and $|-1>$ eigenstates and induces a magnetic moment that is detectable by the spectrometer.[58]

Because the low effective magnetic moments of ^{14}N nuclei (even with the application of a small magnetic field) is insufficient for SQUID detection, an indirect method (cross-relaxation to adjacent protons) is employed. It should be noted that pulsed techniques which detect the transverse magnetization are not troubled by a vanishing magnetic moment [17,61]. Conventional NQR techniques which employ Faraday detection are inhibited by the low ^{14}N transition frequencies (0-6 MHz). Therefore, indirect detection schemes have been employed as well. This has primarily taken the form of field cycling[19,20,62,63]. A pulsed SQUID spectrometer has been used to detect directly ^{14}N in ammounium perchlorate[64]. The spectrometer has recently been modified to allow detection of resonance frequencies of $\leq$ 3 MHz[65]. However, ^{14}N-^{1}H cross-relaxation still has additional advantages. Because the cw SQUID spectrometer detects the change in magnetization of the protons the intensity of the signal is increased by a factor of γ_H/γ_N (~15). Additionally, most samples contain more protons than nitrogen nuclei. The higher spin density also contributes more intensity to the spectra if the proton spin diffusion is sufficiently rapid.

Before explaining the technique of ^{14}N-^{1}H cross-relaxation using the cw SQUID spectrometer, a brief introduction to the concept of spin temperature as distinct from lattice temperature is in order[66]. The concept of spin temperature is a pictorial description of a saturation experiment, which is the kind of experiment performed with this spectrometer. A spin temperature is an equilibrium temprature higher than that of the bath which represents a balance between two competing processes: the input of energy into the spin system, and the energy transfer from the spin system to the lattice. To put this into a quantitative explanation, suppose that we have a two level system with populations P_1 and P_2. Prior to the application of rf, the spins are in thermal equilibrium, and so their populations are governed by the Boltzmann distribution. Using the high temperature approximation, we find

$$P_1 - P_2 = \frac{h\nu_{12}}{kT}. \qquad 2.33$$

The application of an rf field decreases the population difference below thermal equilibrium values. If P_1 and P_2 become the new steady-state values of the population, we can define a spin temperature, T_s, higher than the lattice temperature as

$$\frac{P_1}{P_2} = \exp\left(\frac{h\nu_{12}}{kT_s}\right). \qquad 2.34$$

Note that if the spin system is completely saturated (i.e. $P_1 = P_2$), the spin temperature is infinite.

In order for this technique to be carried out, an applied magnetic field is set such that a multiple of the Larmor frequency ($n\nu_L{}^H$; n=1,2,3) for a spin I=1/2 proton is matched to a nitrogen quadrupole transition frequency (ν_0, ν_-, or ν_+) as shown in figure 2.17a. One of the non-matched transitions is excited with rf irradiation, which changes the population of one of the spin states of the level matching transition. Thus, the nitrogen spin reservoir associated with the level matching is either heated or cooled. Since the nitrogen spin subsystem is coupled to the proton spin system via the heteronuclear dipolar interaction, cross-relaxation will occur until the proton system and nitrogen subsystem equilibrate to a new common spin temeprature. The change in proton magnetization, which results from the cross-relaxation, creates a detectable signal for the SQUID spectrometer.

2.5.2 Theory

Single Sweep

To examine the level matching experiment in more detail, we will begin with the simplest example, a single sweep with complete saturation, no spin-lattice relaxation, and spin diffusion among the protons and cross-relaxation between the proton and the nitrogen spin baths that is faster than the timescale of the sweep through resonance. At thermal equilibrium, we define the populations of the nitrogen eigenstates as

$$N_z = \frac{N}{3}, \qquad 2.35a$$

$$N_y = \frac{N}{3}(1-a), \qquad 2.35b$$

$$N_x = \frac{N}{3}(1-b), \qquad 2.35c$$

where

$$1-a = \exp(-\frac{h\nu_-}{kT}) \approx 1 - \frac{h\nu_-}{kT}, \qquad 2.36a$$

$$1-b = \exp(-\frac{h\nu_+}{kT}) \approx 1 - \frac{h\nu_+}{kT}, \qquad 2.36b$$

and the populations of the zeeman proton eigenstates as

$$P_+ = \frac{P}{2}, \qquad 2.37a$$

$$P_- = \frac{P}{2}(1-a). \qquad 2.37b$$

If we choose to match a Larmor frequency to the ν_- transition and saturate the ν_+ transition by rf irradiation (figure 2.17a) then some fraction of the nitrogen spins, Ns/3, will be transferred from the N_z to the N_x energy level which alters the spins temperature of the N_y,N_z spin sybsystem. Recall that for the proton-nitrogen spin subsystem the spin temperature of protons, T_{proton}, will equilibrate with the spin temperature of the nitrogen subsystem, $T_{nitrogen}$. This means that some fraction, Nr/3, of spins will be transferred from the N_y to the N_z energy levels while PRr/2 proton spins will be transferred from the P_+ to the P_- level until a new common spin temperature is reached. R is the factor to account for the different number of spins in the proton and nitrogen spin states and is given by

$$R = \frac{N}{3}\frac{2}{P} = \frac{2}{3}\frac{N}{P}. \qquad 2.38$$

The final populations, assuming no spin-lattice relaxation are

$$N_z = \frac{N}{3}(1-s+r), \qquad 2.39a$$

$$N_y = \frac{N}{3}(1-a-r), \qquad 2.39b$$

$$N_x = \frac{N}{3}(1-b+s), \qquad 2.39c$$

$$P_- = \frac{P}{2}(1-a+Rr), \qquad 2.39d$$

$$P_+ = \frac{P}{2}(1-Rr). \qquad 2.39e$$

Assuming that the rf completely saturates the ν_+ transition

$$N_z = N_x, \qquad 2.40$$

and that thermal equilibrium between the proton and nitrogen spin baths is maintained,

$$T_{proton} = T_{nitrogen}, \qquad 2.41$$

the change in magnetization produced can be estimated. Two conditions exist at the end of the experiment. Since the proton Larmor frequency in this case is matched to the ν_- transition

$$\frac{1}{\nu_h}(1 - \frac{P_-}{P_+}) = \frac{1}{\nu_-}(1 - \frac{N_y}{N_z}). \qquad 2.42$$

reduces to

$$\frac{P_-}{P_+} = \frac{N_y}{N_z}. \qquad 2.43$$

Substituting 2.39a and 2.39b into the first condition results in

$$\frac{N}{3}(1-s+r) = \frac{N}{3}(1-b+s) \qquad 2.44$$

$$s = \frac{(b+r)}{2}. \qquad 2.45$$

The second condition gives

$$\frac{\frac{P}{2}(1-Rr)}{\frac{P}{2}(1-a+Rr)} = \frac{\frac{N}{3}(1-s+r)}{\frac{N}{3}(1-a-r)}, \qquad 2.46$$

which leads to

$$s(1-a+Rr) = r(2-a+2R). \qquad 2.47$$

In the high temperature limit, the population differences are very small. Thus, $a,r<<1$. By rewriting equation 2.47 with negligible terms eliminated, we find

$$r = \frac{s}{(2+2R)}. \qquad 2.48$$

Combining equations 2.45 and 2.36b gives

$$r = \frac{b}{(4R+3)} = \frac{\hbar\nu_+}{kT(4R+3)}. \qquad 2.49$$

The change in magnetization results from the PRr/2 proton spins that have flipped,

$$\Delta M = -\frac{\gamma\hbar PRr}{2} = -\frac{\gamma\hbar^2 PR\nu_+}{2kT(4R+3)}$$

$$= -\frac{\gamma\hbar^2 PR}{2}\frac{3}{4}\frac{e^2qQ(1+\frac{\eta}{3})}{kT(4R+3)}. \qquad 2.50$$

Note that

$$\Delta M \propto \nu_+. \qquad 2.51$$

In general,

$$\Delta M \propto \pm\nu_{obs.} \qquad 2.52$$

The change in magnetization can be positive or negative depending on whether the nitrogen spin reservoir is heated or cooled.

Figure 2.17 illustrates the different sets of conditions under which experiments have been carried out. Table 2.1 summarizes the changes in populations under the different conditions. This is not an inclusive list, but is representative of the experiments performed.

Single sweep with $2\nu_L{}^H$

If, for example, the ν_- nitrogen quadrupole transition frequency is matched to $2\nu_L{}^H$, then two proton spins flip for every nitrogen spin that relaxes. The initial and final nitrogen populations are the same as the previous case. The initial proton populations are

$$P_+ = \frac{P}{2} \qquad 2.37a$$

$$P_- = \frac{P}{2}(1-\frac{a}{2}), \qquad 2.37b'$$

while the final proton populations are

$$P_- = \frac{P}{2}(1-\frac{a}{2}+2Rr), \qquad 2.39d'$$

$$P_+ = \frac{P}{2}(1-2Rr). \qquad 2.39e'$$

The thermal equilibrium condition becomes

$$2(1 - \frac{P_-}{P_+}) = (1 - \frac{N_y}{N_z}). \qquad 2.42'$$

The change in magnetization due to the 2rRP/2 proton spins that flip is calculated to be

$$\Delta M_{2vh} = -\gamma \hbar PrR = -\frac{\gamma \hbar^2 PR\nu_+}{kT(16R+3)}. \qquad 2.53$$

It should be noted that this change in magnetization cannot be compared with the change in magnetization for the matching to the Larmor transition. The transition matrix elements for the experiments are smaller corresponding to the higher order terms of the dipolar interaction that are needed to accommodate 3 spins (2 proton and 1 nitrogen).

Double sweep

The double sweep can increase the intensity of the transition by irradiating the third transition in the nitrogen spin system. This facilitates the observation of weak resonances such as the ν_0 transition which typically has a low transition frequency. This method is restricted to samples with a long spin-lattice relaxation time relative to the sweep time of the spectrum. However, a second specific transition frequency does not need to be known in order for experiments to be carried out. In the double sweep method, a sweep through one resonance is followed by a sweep of a second resonance. For the case shown in figure 2.17c, the ν_+ transition is irradiated first. In ideal circumstances, the resulting populations after the sweep are the same as in a single sweep situation. When the ν_0 transition is swept, Ns'/3 spins are transferred from |y> to |x> due to rf irradiation and Nr'/3 spins are relaxed by the protons. The final populations, assuming no spin-lattice relaxation are given in Table 2.1.

The final conditions will be

$$N_y = N_x, \qquad 2.40''$$

$$\frac{1}{\nu_h}(1 - \frac{P_-}{P_+}) = \frac{1}{\nu_-}(1 - \frac{N_y}{N_z}). \qquad 2.42''$$

The formula for the change in magnetization can be generalized to

$$\Delta M = -\frac{\gamma \hbar^2 PR}{2kT}\left(\frac{\pm\nu_{obs} \pm \frac{2R+3}{4R+3}\nu_{irr}}{4R+3}\right). \qquad 2.54$$

In comparing the signal intensity of the double sweep with the single sweep, it should be noted that the double sweep method does not always result in a signal enhancement.

Double irradiation

Double irradiation is the simultaneous irradiation of two channels of rf. The first, ν_{irr}, is held constant at the frequency of a known transition in order to saturate the transition before and during the sweep of the second rf channel, which possibly contains the third resonance, ν_{obs}. Unlike the double sweep, this method enhances the intensity of any resonance and does not require a spin-lattice relaxation time longer than the sweep time of the experiment. Therefore, it is useful in detecting low intensity transitions (such as ν_o) and establishing connectivities between two resonances, which becomes necessary when more than one nitrogen site is present in a sample. However, it requires a known transition, which is not necessary for the double sweep experiment.

The simultaneous irradiation of the two non-level matching transitions under ideal conditions leads to equilibration of the populations in the enegy levels. Thus,

$$N_x = N_y = N_z = \frac{N}{3}, \qquad 2.55$$

$$P_+ = P_- = \frac{P}{2}, \qquad 2.55b$$

$$\frac{P_-}{P_+} = \frac{N_y}{N_z} = 1. \qquad 2.56c$$

Assuming complete cross-relaxation and spin diffusion, the proton spins are entirely saturated at the end of the experiment. The number of proton spins flipped in the transition is the difference between the final population and the population after irradiation of ν_{irr},

$$P_-(\text{end}) - P_-(\text{intermediate}) = \frac{P}{2}(a - \frac{Rb}{4R + 3}), \qquad 2.57$$

with a final change in magnetization of

$$\Delta M = -\frac{\gamma\hbar^2 PR}{2kT}(\nu_{cr} \pm \frac{R\nu_{irr}}{4R + 3}). \qquad 2.58$$

Level matching conditions

The cw SQUID spectrometer provides an alternative to field cycling, which is an inherently two-dimensional technique. In field cycling, the applied magnetic field is swept at each rf frequency irradiated. It should be noted that the level matching technique used here is also an inherently two-dimensional technique. The rf frequency is swept at each applied magnetic field. The magnetic field may have to be changed several times before a transition is found. However, the level of difficulty in searching for unknown quadrupolar resonances is reduced by the following: First, the transition has to be matched to a multiple of a Larmor frequency within the strength of the dipolar coupling, which broadens the proton spectrum considerably. Typical Larmor lines have linewidths of 80-100 kHz, while twice the Larmor frequency has a linewidth of ~50 kHz. Although $3\nu_L{}^H$ is not able to be observed directly, a nitrogen transition in close proximity will result in a sufficient change in magnetization to be observed. Thus, because of the broad proton lines and the ability to use overtones of the Larmor line, the field can be stepped coarsely when searching for resonances. Second, we have a priori knowledge of the range of resonance frequencies expected for a nitrogen nucleus in a particular bonding environment. This is illustrated in figure 2.18. Finally, when one resonance frequency is found, the field can be set to match that transition in the search for the other two connected transitions.

	Single Sweep (fig 2.17a)		Double Sweep (fig 2.17c)		
	Before	After	Before	After sweep1	After sweep 2
N_x	N(1-b)/3	N(1-b+s)/3	N(1-b)/3	N(1-b+s)/3	N(1-b+s+s')/3
N_y	N(1-a)/3	N(1-a-r)/3	N(1-a)/3	N(1-a-r)/3	N(1-a-s'-r-r')/3
N_z	N/3	N(1-s+r)/3	N/3	N(1-s+r)/3	N(1-s+r+r')/3
P_-	P(1-a)/2	P(1-a+Rr)/2	P(1-a)/2	P(1-a+Rr)/2	P(1-a+Rr+Rr')/2
P_+	P/2	P(1-Rr)/2	P/2	P(1-Rr)/2	P(1-Rr-Rr')/2
	Single Sweep $2\nu_L{}^P$ (fig 2.17b)		Double Irradiation (fig 2.17c)		
	Before	After	Before	Intermediate	After
N_x	N(1-b)/3	N(1-b+s)/3	N(1-b)/3	N(1-b+s)/3	N/3
N_y	N(1-a)/3	N(1-a-r)/3	N(1-a)/3	N(1-a-r)/3	N/3
N_z	N/3	N(1-s+r)/3	N/3	N(1-s+r)/3	N/3
P_-	P(1-a/2)/2	P(1-a/2+2Rr)/2	P(1-a)/2	P(1-a+Rr)/2	P/2
P_+	P/2	P(1-2Rr)/2	P/2	P(1-Rr)/2	P/2

Table 2.1 Summary of the population changes of ^{14}N cross-relaxation under different conditions.

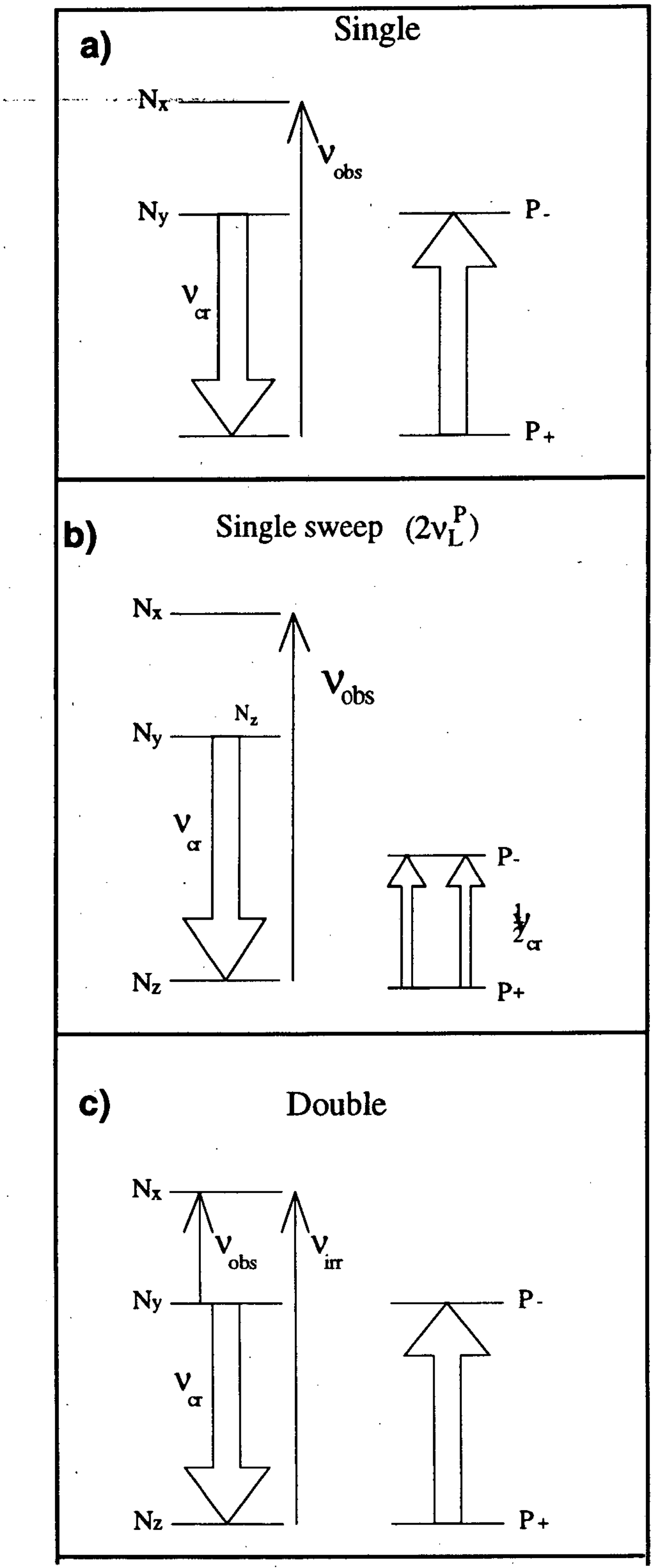

Figure 2.17 Level Matching schematics for ^{14}N-^{1}H cross-relaxation.

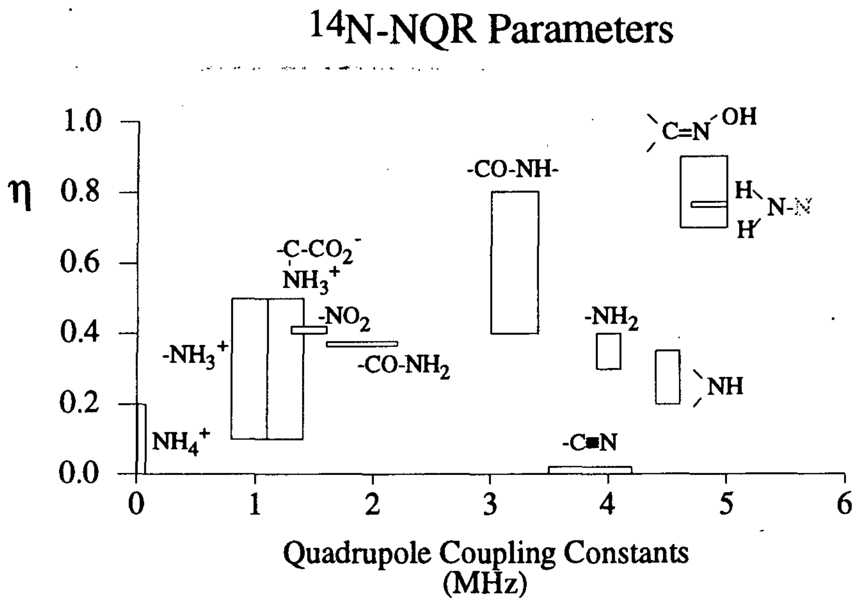

Figure 2.18 The range of C_q and η that nitrogen nuclei in different types of bonding arrangements are found.

2.5.3 Results

Table 2.2 summarizes ^{14}N NQR resonances in peptides that have been measured in the course of this work. When available, literature references to measurements by other techniques have also been provided. Earlier resonances, particularly those of amino acids as well as some higher frequency resonances for other compounds may be found in Bruce Black's thesis[58]. In addition, some systems will be discussed in greater detail below.

Optically Active Isomers

The sensitivity of the nitrogen NQR frequency to small changes in the nitrogen environment can be demonstrated by comparing the spectra of the optically active isomers L-serine and D-serine ($CH_2(OH)CH(NH_3^+)CO_2^-$) to the spectra of the racemic mixture DL-serine. The NH_3^+ groups of D-serine and L-serine have identical resonance frequencies $\nu_+ = 979 \pm 4$ kHz and $\nu_- = 895 \pm 4$ kHz (figure 2.19), as expected. Because the crystal structures are related by reflection, the nitrogen quadrupolar parameters are identical e^2qQ/h

Name	Site	ν_+ (kHz)	ν_- (kHz)	ν_0 (kHz)	CQ(kHz)	η	Ref.	T(K)
Diglycine	NH_3^+	2590 ±3	1972 ±3	—	3041 ±3	0.407 ±0.005		4.2
		(2585)	(1975)	(620)	(3030)	(0.41)	20	(77)
	NH	1058 ±3	—	—	—	—		4.2
		(1090)	—	(260)	(1280)	(0.41)	20	(77)
Triglycine	?	1167 ±6						4.2
	?	898 ±8						4.2
	?	843 ±7						4.2
	NH	(2900)		(1175)	(3080)	(0.76)	20	(77)
	NH	(2620)		(720)	(3010)	(0.48)	20	(77)
	NH_3^+	(1025)		(275)	(1180)	(0.46)	20	(77)
L-alanyl-L-histidine	NH_3^+	1203 ±6	933 ±4	—	1424 ±5	0.379 ±0.007		4.2
	NH_3^+	1160 ±3	834 ±4	327 ± 5	1329 ±4	0.491 ±0.006		4.2
	NH	1550 ±3	—	—	—	—		4.2
	NH	1477 ±3	953 ±7	524 ± 7	1620 ±6	0.647 ±0.008		4.2
L-alanyl-diglycine	NH_3^+	1033 ±13	837 ±5	183 ± 6	1247 ±9	0.314 ±0.014		4.2
Cocaine HCl	N...H+	966 ±3	815 ±3	—	1186 ±3	0.252±0.005		4.2
		(961)	(813)		(1182)	(0.250)	4	295

Table 2.2 Polypeptide and cocaine hydrochloride ^{14}N results. Literature values are given in parentheses below our experimental results.

= 1223 ± 4 kHz, η=0.194 ± 0.01 (literature [20] for T = 77 K: e^2qQ/h= 1215 ± 4 kHz, η = 0.184 ± 0.003). On the other hand, the racemic mixture of DL-serine crystallizes in a different structure that accommodates both isomers. This leads to intermolecular nitrogen environments that differ from those of the optically pure crystals. However, the D- and L-molecules within this racemic crystal (P21/a symmetry) are related by reflection on a mirror plane[67], so they experience identical electric field gradients and have the same quadrupole parameters. The quadrupole transition frequencies are shifted by 23 kHz (ν_- = 882 ± 3 kHz) and -18 kHz (ν_+ = 961 ± 3 kHz) away from those of the optically active isomers. The derived quadrupole parameters e^2qQ/h= 1227 ± 2 kHz, η = 0.128 ± 0.005 change only slightly in the magnitude of the quadrupole constant, but significantly in the anisotropy parameter. The anisotropy parameter is a consequence of the changes in the hydrogen bonds in which the nitrogen atoms participate, cause mainly by the intermolecular crystal packing around the ammonium group. The small difference between the current data for the quadrupole parameters and the literature values[20] for T = 77 K (e^2qQ/h = 1217 ± 1 kHz, η = 0.118 ± 0.003) probably result from the different temperatures at which the data were obtained.

A mixture of 25% D-serine and 75% L-serine was dissolved and reprecipitated from aqueous solution. The high resolution of the transition frequencies from the pure and racemic compounds can be used to determine whether the 25:75 precipitate contains both isomers in random positions, or whether it crystallizes into conglomerates. The conglomerates can be composed of either the chiral crystals D- and L-serine or of the racemic crystal and the excess L-serine. Crystals containing the serine isomorphs in random position would cause a broad distribution of resonances, while conglomerates of the pure materials should give resonances at the frequencies of the pure chiral or racemic materials.

The precipitate was collected in two fractions, the first one containing the crystals that formed early, the second one consisting of the remainder. The first precipitate shows resonances close to those of DL-serine (878 ± 8 kHz and 961 ± 5 kHz). The resonance frequencies of the second crystallization fraction resemble mostly those of the optically pure isomer (857 kHz and 979 kHz). These results show that most of the racemic crystallization has taken place first, leaving the excess L-serine to crystallize last. The preference of the crystallization into the racemic mixture indicates a greater stability of the DL crystal form, in agreement with earlier results[68].

L-alanine and L-histidine forming L-Ala-L-His

L-Alanine The results of combining two different amino acids into a dipeptide is illustrated by the formation of L-Ala-L-His from the amino acids L-alanine and L-histidine (figure 2.20) All three transitions of L-alanine ν_+ = 988 ± 3 kHz, ν_- = 828 ±4 kHz and ν_o = 160 ± 4 kHz can be detected. The signal for the ν_o resonance (160 ± 4 kHz), which is

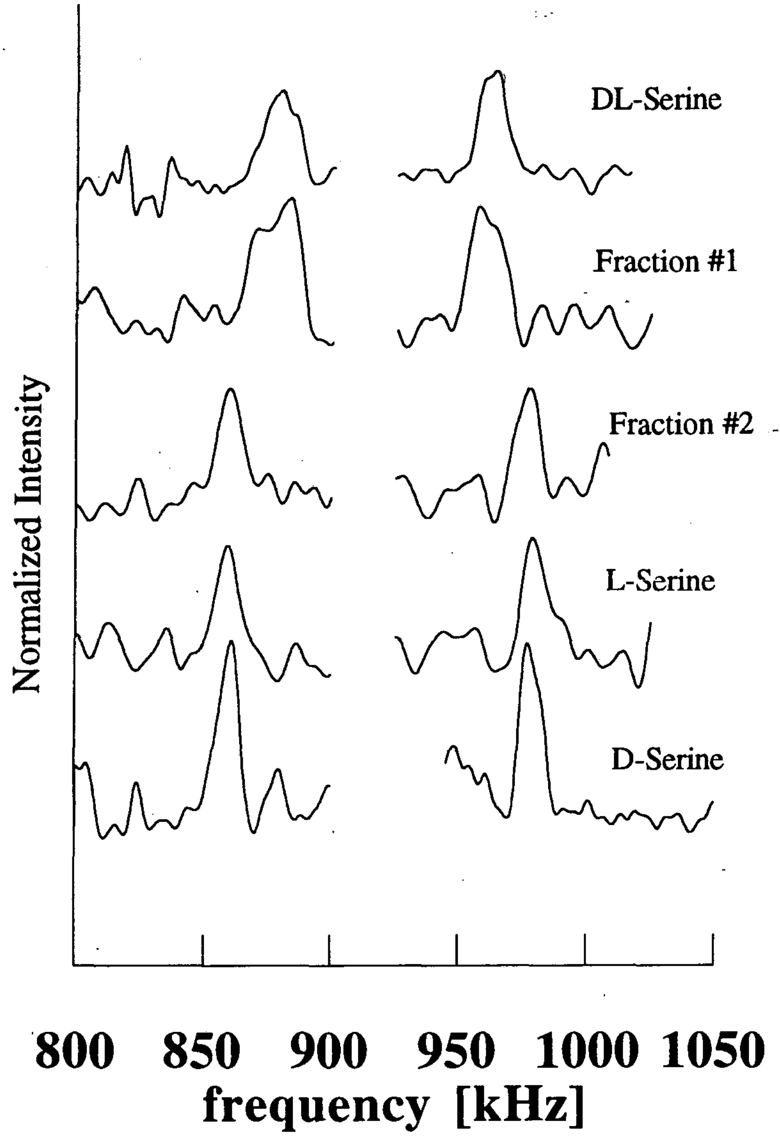

Figure 2.19 ^{14}N NQR spectra (normalized derivatives of SQUID detected continuous wave sweeps) of D- and L-serine in different degrees of optical purity. The crystals from a solution of 75% L-serine and 25% D-serine were collected in two fractions. The spectra were acquired by matching the nitrogen transitions ν_- and ν_+ with the proton resonance frequencies $2\nu_L^H$, and observing the remaining ν_+ and ν_- resonances, respectively.

too weak to be detected under single irradiation techniques, can be enhanced sufficiently by exciting the ν_+ resonance (988 ± 3 kHz) [51]. The experimentally determined quadrupolar parameters e^2qQ/h = 1208 ± 3 kHz, η = 0.267 ± 0.005 agree well with previous results at 77K giving e^2qQ/h = 1205 ± 1 kHz, η = 0.261 ± 0.003[20].

L-Histidine The L-histidine spectra show five resonance frequencies at 908 ± 2 kHz, 939 ± 2 kHz, 982 ± 3 kHz, and 1410 ± 3 kHz. The dependences of the signal intensities on the magnetic field strength allow us to identify connected transitions: The resonances at 908 ± 2 kHz and 982 ± 3 kHz result from one terminal nitrogen site while the resonances at 939 ± 2 kHz and 1030 ± 3 kHz originate from a second terminal nitrogen atom giving quadrupolar parameters e^2qQ/h = 1258 ± 2 kHz and η = 0.115 ± 0.005 and e^2qQ/h = 1312 ± 2 kHz, η = 0.140 ± 0.005, respectively. Since the existence of two different sites with e^2qQ/h = 1251 ± 3 kHz and η = 0.113 ± 0.006 and e^2qQ/h = 1305 ± 3 kHz,η= 0.143 ± 0.006 (at T=77 K) was reported earlier and traced back to a mixture of orthorhombic and monoclinic L-histidine[69], respectively, no further effort was invested to separate those compounds. The transition frequencies connected with the site causing the resonance at 1410 ± 2 kHz have not been identified. However, using the matching condition of one nitrogen resonance with the proton Larmor frequency, $\nu_L^{H,}$ or one of its multiples, the lower transition frequencies can be estimated to be in the range between 610-670 kHz and 720-780 kHz. This explains why the peak at 1410 kHz becomes visible at fields with proton Larmor frequencies ν_L^H = 636 kHz, 746 kHz, and with $2\nu_L^H$ = 740 kHz (i.e. ν_L^H = 370 kHz), respectively, but cannot be observed at a field with proton Larmor frequency ν_L^H = 702 kHz (figure 2.21). Earlier results for higher temperatures at T=77 K, e^2qQ/h = 1437 ± 1 kHz, η = 0.915 ± 0.003 fall within the range of the estimated quadrupole coupling constants e^2qQ/h = = 1452 ± 30 kHz, η = 0.88 ± 0.07. The magnitude of the quadrupole coupling constant and the anisotropy parameter suggest that this nitrogen resonance is caused by an imidazole nitrogen in the histidine ring. The fact that the resonance is sharper than those of the terminal nitrogen atoms is consistent with a smaller dipole-dipole coupling due to a single proton as opposed to the larger dipolar interaction of the terminal nitrogen atoms bonded to three protons. We do not find any further resonances from the second imidazole nitrogen atom, probably the one without directly bonded protons. The hydrogen bonding between the imidazole nitrogen and a proton from a neighboring molecule is probably insufficient for the cross-relaxation necessary for detection in our technique.

L-Ala-L-His The L-Ala-L-His spectra show eight resonances. Field dependent studies and double irradiation allow us to assign the following transition frequencies: 327 ± 5 kHz, 832 ± 4 kHz and 1160 ± 3 kHz (e^2qQ/h = 1324 ± 3 kHz, η = 0.49 ± 0.005) to one terminal nitrogen: and 931 ± 4 kHz and 1205 ± 4 kHz (e^2qQ/h = 1423 ± 3 kHz, η = 0.384 ±).005), to a second terminal nitrogen site. The resonance frequencies at 1477 ± 2 kHz and 524 ± 4 kHz originate from one imidazol nitrogen with e^2qQ/h= 1619 ± 2 kHz and η = 0.646 ± 0.005. The signal at 1550 ± 2 kHz shows sharp features, similar to the transition in the imidazole ring both in L-Ala-L-His and L-histidine indicating that it probably also results from an imidazole resonance. The field dependence of the resonance seems to indicate a slightly higher quadrupole coupling constant. To our knowledge no literature values are available for this compound. In summary, we find evidence for two different terminal nitrogen sites and two imidazole nitrogen sites.

In the L-Ala-L-His peptide, the terminal nitrogens are members of the L-alanine fraction of the molecule. The quadrupole parameters of these terminal nitrogens are larger both in magnitude and asymmetry parameter than those of pure L-alanine indicating a more distorted environment. This arises probably mainly from a change of the hydrogen bonds to the neighboring molecules. Similarly, the environment of the imidazole nitrogens is more asymmetric than that in the pure L-histidine crystal structure. The asymmetry parameter here reflects mostly the imidazole ring structure. The lower value of the asymmetry parameter indicates a greater deviation from planar symmetry, which means that the ring also is deformed by the crystal packing of the peptide.

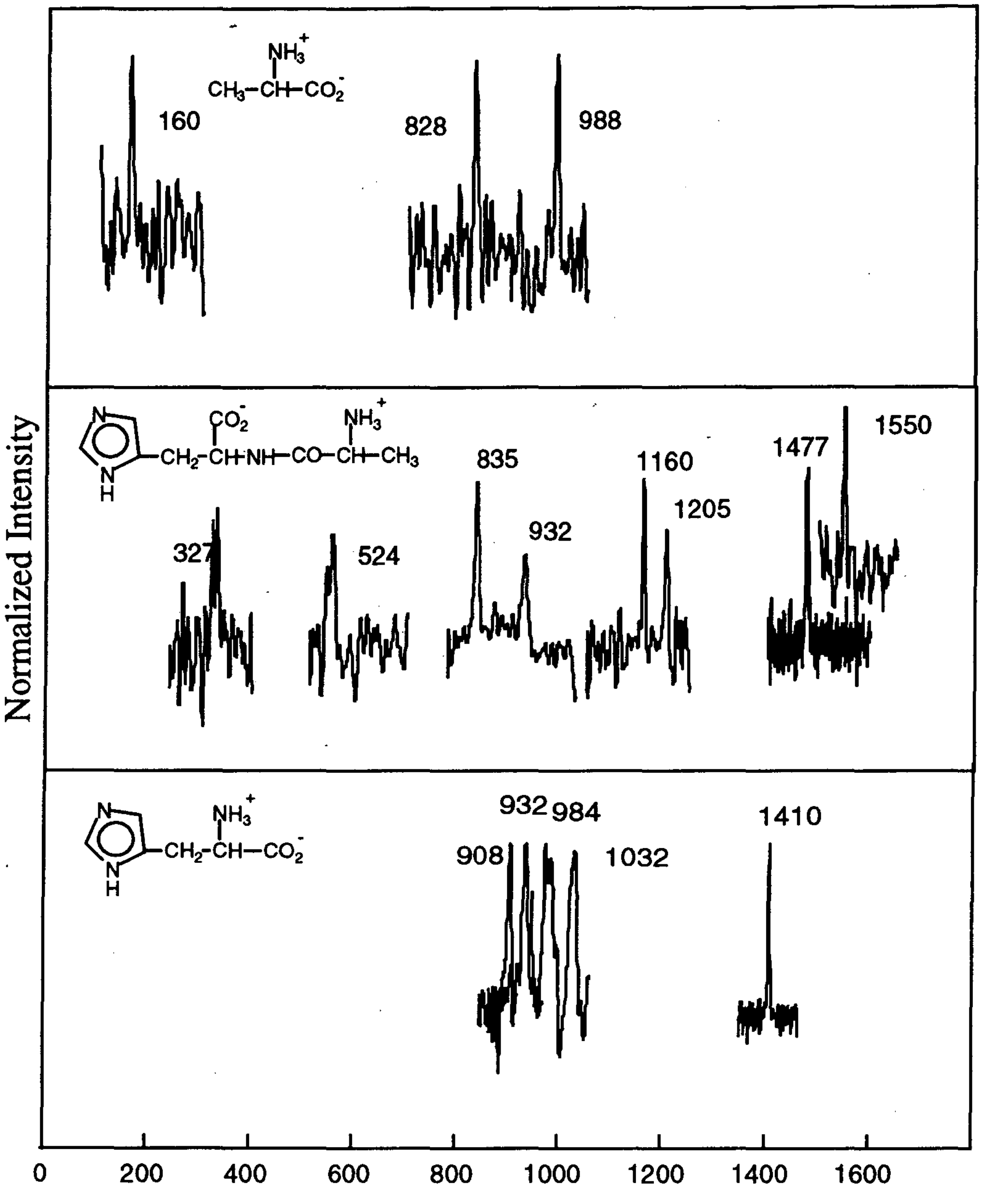

Figure 2.20 ^{14}N spectra (normalized derivatives of sweeps) for L-alanine (top), L-Ala-L-His (center) and L-histidine (bottom).

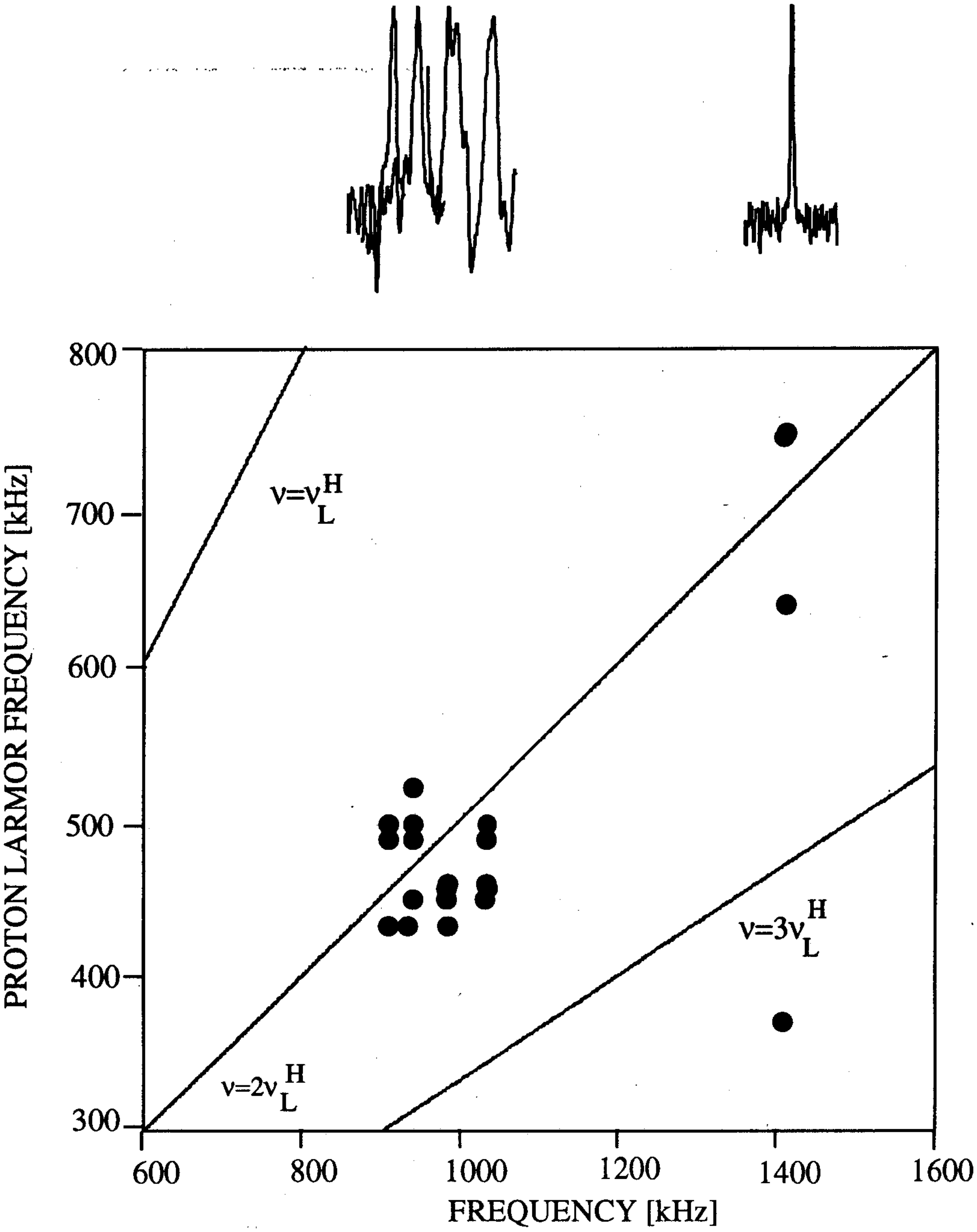

Figure 2.21 Dependence of the nitrogen resonances of L-histidine on the matching with the proton Larmor frequency ν_L^H.

Cocaine hydrochloride

Figure 2.22a shows a spectrum for cocaine hydrochloride of the ν_+ (966 kHz) and ν_- (813 kHz) transitions. The transitions were observed by matching the ν_- transition to the $3\nu_L{}^H$ Zeeman transition. The ν_o transition, although searched for, could not be seen. This could, in part, be due to the fact that the resonance frequency occurs near the lower limit of the spectrometer. Figure 2.22a is a combined spectrum representing forward and reverse sweeps (four of each). Figure 2.22b presents the data with 1 kHz Gaussian broadening applied, followed by taking the derivative of figure 2.22a. This is done to easily locate the peak location. After correcting for magnetic field, C_q was calculated to be 1.186 MHz with $\eta = 0.252$. ν_+ and ν_- were subsequently observed by Garroway and co-workers at both 77 K (961 and 813 kHz, respectively; C_q=1.182 with η=0.250) and 295 K (961 and 806 kHz, respectively; C_q=1.178 MHz with η=0.263). After 150K number of scans, representing a week worth of run averaging, they finally observed the transitions at 295 K with a conventional NQR spectrometer. The sensitivity of NQR to its surrounding environment is well demonstrated by comparing cocaine hydrochloride to cocaine free base. The quadrupolar parameters for cocaine free base have been measure to be 5.0228 MHz, with η=0.0395[4].

The crystal structure of cocaine hydrochloride is orthorhombic with space group $P2_12_12_1$ and Z=4. Low-frequency Raman spectra of this compound have been reported at room temperature and 9K and assigned; no evidence of any change in the crystalline phase between these temperatures was mentioned. The piperidine ring of the tropane nucleus has the chair form, with the CH_3 group of the N equatorial; the C-N bonds and C-N-C angles are close to normal (see Figure 2.23). Although the lcoation of the acidic hydrogen atom could not be determined, the short N-Cl bond distance (306.9 pm) suggests the presence of a hydrogen bond between the nitrogen and the chlorine, not necessarily a linear one.

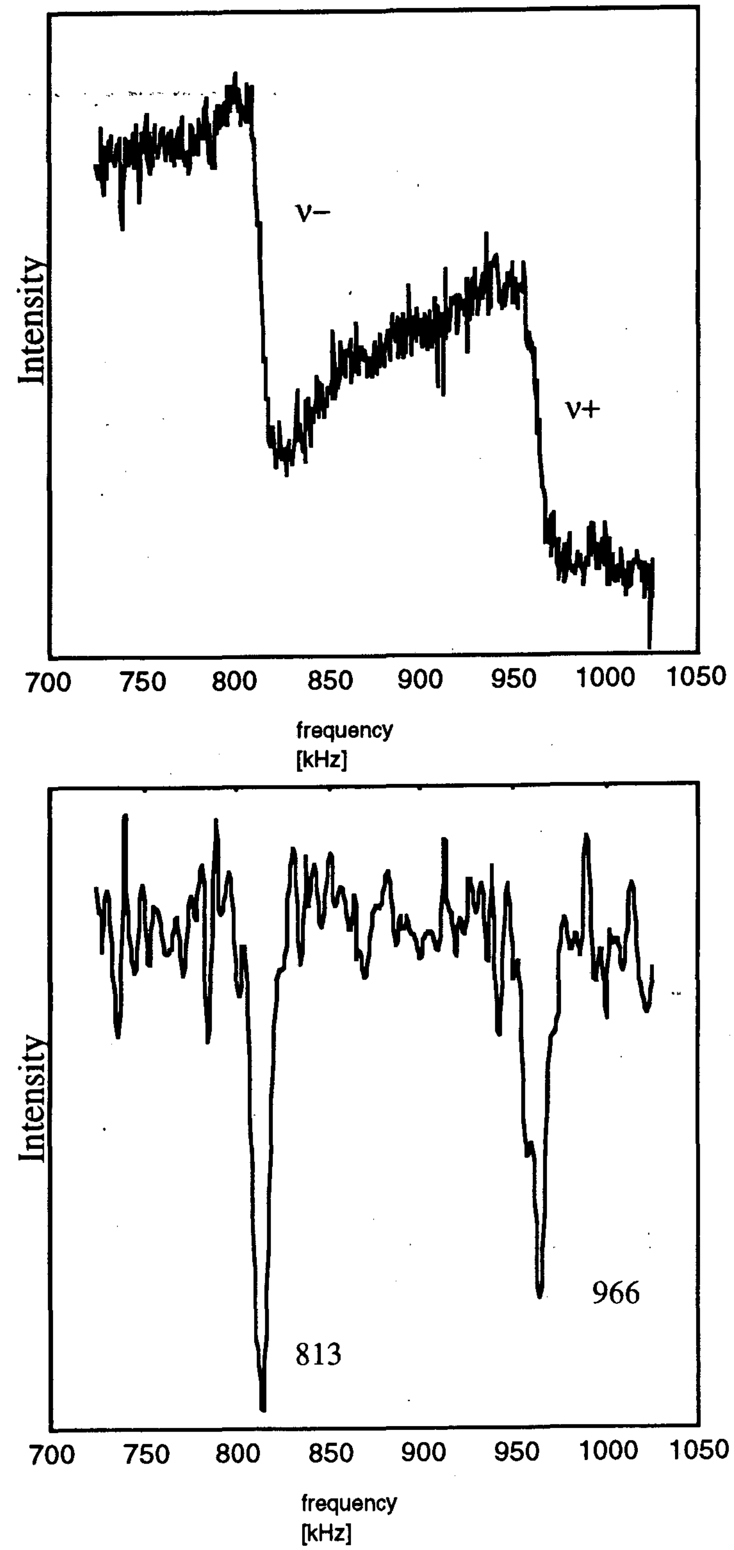

Figure 2.22 a) Raw data for cocaine hydrochloride. The spectrum was obtained by matching the ν_- transition to the $3\nu_L{}^H$ Zeeman transition. The ν_- (813 kHz) and ν_+ (966 kHz) transitions correspond to a C_q of 1.186 MHz and η of 0.252. b) Derivative mode of raw spectrum emphasizing peak position

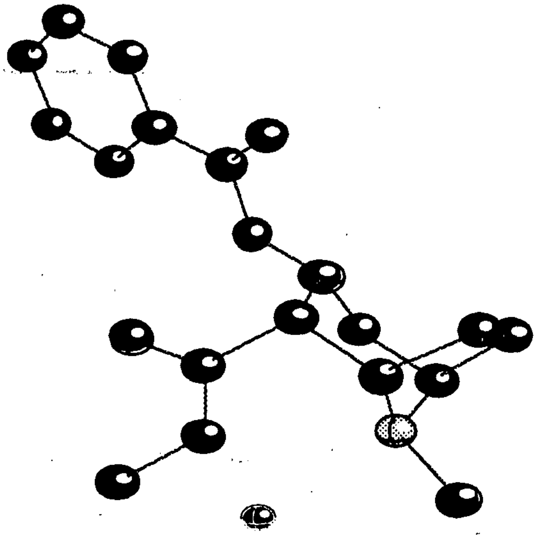

Figure 2.23 Structure of cocaine hydrochloride, from coordinates of X-ray crystallographic data. Hydrogen atoms are not shown, including the unlocated acidic hydrogen atom. Although the location for the acidic hydrogen atoms could not be determined, the short N-Cl bond distance (3.0690 Å) suggests the presence of a hydrogen bond between the nitrogen and chlorine, not necessarily a linear one.

2.5.4 ^{14}N NQR as an analytical tool

NQR has a number of advantageous characteristics as an analytical technique, since it is: (1) highly specific with regard to the chemical and crystalline form of a substance; (2) non-destructive; (3) quantitative; (4) capable of detecting compounds heterogeneously distributed over large volumes; (5) able to yield results quickly (in favorable cases), with no sample preparation; and (6) sensitive to the presence of co-crystallized impurities in the sample. Some of these advantages may, in a different context, instead be weaknesses (points 1 and 6 in particular). Also, one serious limitation to the more widespread use of pure NQR as an analytical technique is the general requirement of samples containing many grams or tens of grams of the compound being detected, although SQUID detection has been advantageous in the size of samples used. Furthermore, it is usually time consuming, and often impracticable, to use pure NQR to search for unknown NQR transition frequencies. Because the SQUID spectrometer is a broadband, untuned spectrometer, large frequency ranges can easily be swept in the search for and identification of NQR resonances. The main drawbacks to the more mainstream use of the SQUID as an alternative to pure NQR detection are: (1) It is operated at 4.2 K. In addition to needing access to liquid helium, the spin-lattice relaxation times of many compounds become unreasonably long; and (2) because the nitrogen nuclei are detected by their effect on neighboring protons mediated by the heteronuclear dipolar interaction, other information about ^{14}N (such as ^{14}N T_1s) are lost.

Nitrogen is present as a heteroatom in many compounds of pharmacologic and biological interest. The stable isotope of nitrogen (^{14}N) has a natural abundance of 99.635%, a nuclear spin $I = 1$ with a corresponding nuclear electric quadrupole moment, and pure NQR transitions at frequencies ranging from 0-6 MHz. From an analytical point of view, knowledge of the ^{14}N NQR frequencies and other parameters is important because of the possibilitiy of using ^{14}N NQR as a *compound-selective* technique for the identification of specific crystalline substances in the solid state. The number of reported ^{14}N NQR resonance frequencies taken from a database of ~10,000 compounds (not necessarily containing nitrogen) reaches a maximum of ~600 in the range from 2.5-3.0 MHz (figure 2.24). For representative ^{14}N NQR linewidths of < 1 kHz, it is apparent that few "NQR interferences" should arise within this set of compounds. Where such interferences do arise, observation of two connected transitions in the same sample provides a virtually unique signature. .

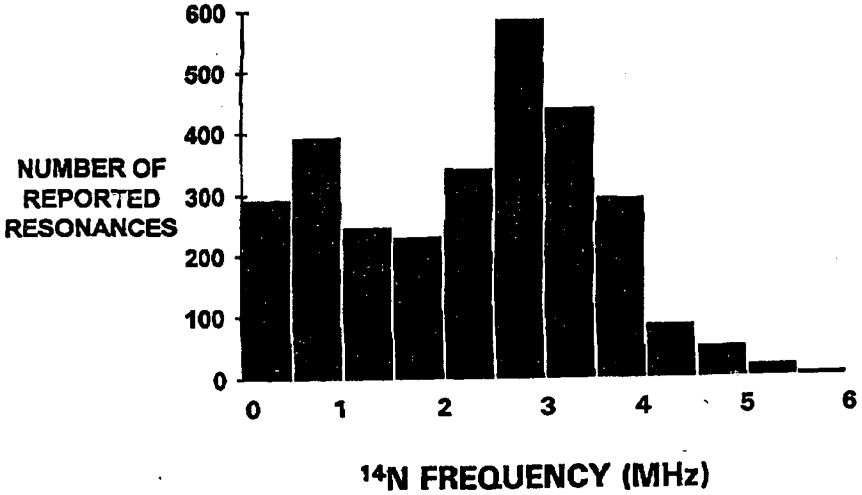

Figure 2.24 Histogram showing the reported ^{14}N resonances taken from a database of approximately 10,000 resonances (not necessarily containing nitrogen). The number of reported resonances reaches a maxium of ~600 in the range from 2.5-3.0 MHz.

Chapter 3 Low-frequency ^{129}Xe NMR with a dc SQUID spectrometer

Xenon is a favorable nucleus to study by NMR because it is very sensitive to its local environment. Because the electrons surrounding the nucleus are very polarizable, xenon has a very large (6000 ppm) chemical shift range. Consequently, xenon has been used as a "spy" of the local environment, directly probing the local environment via the chemical shift interaction. Chemical shifts are on the order of parts per million (ppm) of the applied static magnetic field (measured in terms of Larmor frequency). Since the SQUID spectrometer does not have the resolution to measure ppm of Larmor frequencies that are in the kHz range, this is not applicable for investigations using our spectrometer.

Additionally, the transfer of polarization from optically pumped ^{129}Xe to other spin species is an important application in magnetic resonance experiments. A high degree of polarization (up to 35%) of ^{129}Xe has been achieved by laser pumping and spin exchange with rubidium. Cross-polarization from ^{129}Xe to another nucleus of interest (e.g. ^{13}C or ^{14}N) is a topic of intense investigation at the present time[70-72] and has several important benefits. (1) Increasing the polarization of other spin species increases the sensitivity with which they are detected. If a significant fraction of ^{129}Xe polarization can be transferred to another spin species, then it is possible to study systems with low spin densities that have been beyond the realm of conventional NMR and NQR. (2) Polarization is only transferred to spin species in direct contact with the polarized ^{129}Xe , making selective polarization possible. The ultimate goal of this SQUID project is to use this technique to study low spin density quadrupolar systems, such as quadrupolar nuclei on a surface. As discussed in Chapter 2, the quadrupolar interaction is a very sensitive probe of the local structure surrounding the nucleus. The electric field gradients that surround a surface nucleus should differ greatly from that of the bulk. Therefore, it is anticipated that the difference between surface and bulk NQR resonances should be well-resolved. The SQUID has been used to measure resonances low frequency ^{14}N resonances in 1 cm^3 of ammonium perchlorate. In order to investigate systems with a smaller spin densities, an additional enhancement in sensitivity is needed. Additionally, because spin-lattice relaxation times at 4.2 K may be unreasonably long, an enhancement in sensitivity could eliminate the necessity of run averaging and increase the number of compounds available for investigation. The use of laser polarized ^{129}Xe is one way of increasing the nuclear polarization, and thus, the sensitivity in these systems.

3.1 Theory of Optical Pumping and Spin Exchange

Optical pumping, the transfer of angular momentum from polarized light to an atomic system in a magnetic field leading to non-equilibrium population distributions, was first proposed by Alfred Kastler in 1949[73]. He subsequently received the Nobel Prize for this work in 1966[74]. In NMR, where equilibrium population differences between Zeeman levels are very small (ppm), optical pumping can greatly enhance the signal intensity.

The basic idea of optical pumping can be understood in terms of a hypothetical alkali atom without nuclear spin (and, therefore, no hyperfine structure) that has an energy level diagram shown in figure 3.1. The ground state is labeled by the term symbol $^2S_{1/2}$ and the first excited state by $^2P_{1/2}$. In a magnetic field the $^2S_{1/2}$ and $^2P_{1/2}$ energy levels are each split into two magnetic sub-levels, connected by the D1 transition ($^2S_{1/2} \rightarrow {}^2P_{1/2}$). Since the D1 transition is electric dipole allowed, it has a large absorption cross-section and the transfer of angular momentum from a photon to an atom is extremely efficient.

In an optical pumping experiment the atoms are excited by circularly polarized light propagating along the magnetic field. Photons have spin I=1 with m = ±1. If the electric vector of the light is a right-handed helix, the light is said to be right circularly polarized which corresponds to m=1 by convention. The selection rules for electric dipole transmission are $\Delta \ell = \pm 1$ and $\Delta m = 0$ (linearly polarized light); ±1 (circularly polarized light). The selection rules of the circularly polarized light also depend on the direction of the magnetic field with respect to the direction of propagation of the light. If right circularly polarized light produces $\Delta m = +1$ transitions, it is termed $\sigma+$ light.

If σ+ light is used, transitions are excited from the ground m=-1/2 state to the excited m=+1/2 state. Spontaneous emissions from the excited m=1/2 state can take place to either ground state. In the absence of excited state collisional mixing, the branching ratios for the decay are given by the Clebsch-Gordon coefficients to be 1/3 and 2/3 to the m=1/2 and m=-1/2 states, respectively. More realistically, there is rapid excited state mixing due to atomic collisions at the pressures at which optical pumping experiments are performed. As a result, the branching ratios for spontaneous emission become 1/2 and 1/2. If the electron returns to the m=-1/2 ground state, it can be reexcited by another photon. If the electron decays into the m=+1/2 ground state, it remains there for the lifetime of that state. The m=+1/2 ground state becomes highly polarized if the relaxation time of the ground state (~1 s for Rb) is much greater than the time it takes for spontaneous emission from the excited state (~30 ns for Rb).

Rubidium presents a good system with which to conduct optical pumping. ^{85}Rb (I = 5/2; 72.12% abundant) and ^{87}Rb (I = 3/2; 27.85% abundant) both possess a $^2S_{1/2}$ ground state and a $^2P_{1/2}$ first excited state. The D1 transition used for optical pumping has a wavelength of 794.7 nm, which is accessible with our relatively inexpensive CW tunable diode laser. In addition to the splitting of states by a magnetic field into two magnetic sublevels, the interactions of the nucleus with the electrons result in hyperfine splittings. The resulting energy level diagram is given in figure 3.2. The coupling to the nuclear spin may be neglected since the Doppler broadening at the temperatures at which optical pumping is performed is greater than the hyperfine splitting. The resulting fluorescence spectrum is shown schematically in figure 3.3. However, the pressure broadening that results from having >100 torr Xe in the pumping cell renders a single featureless absorption. It should also be noted that the effects of spin orbit coupling may be neglected because the $^2P_{3/2}$ energy level is split by ~15 nm from the $^2P_{1/2}$ energy level which, at 780 nm, is completely out of resonance.

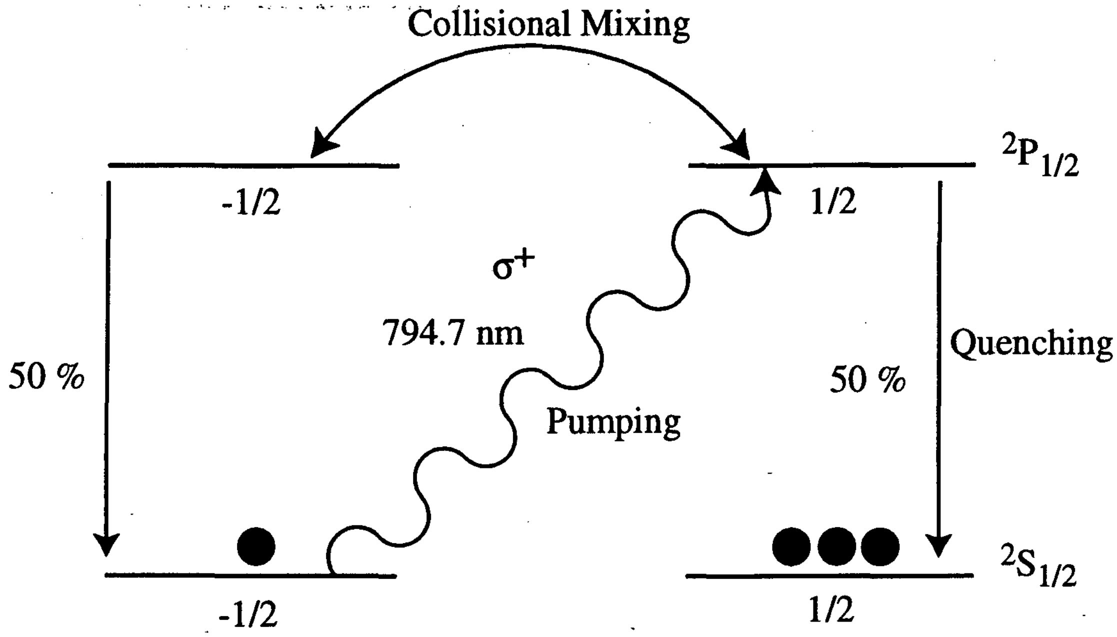

Figure 3.1 Hypothetical optical pumping schematic for an alkali atom without nuclear spin. Circularly polarized light excites the m=-1/2 -> m=+1/2 transition. While spontaneous emission may occur to either state, only electrons in the m=-1/2 state may be excited, leading to polarization of the m=+1/2 state.

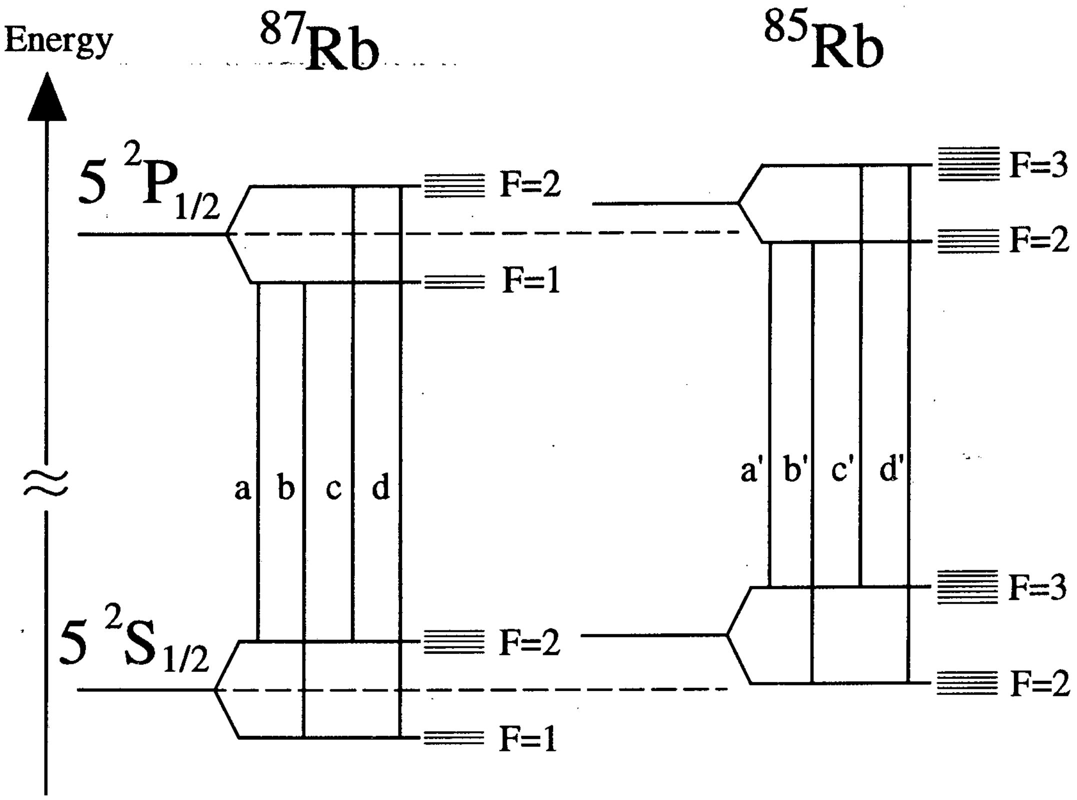

Figure 3.2 Energy level diagram of rubidium with the hyperfine transitions identified.

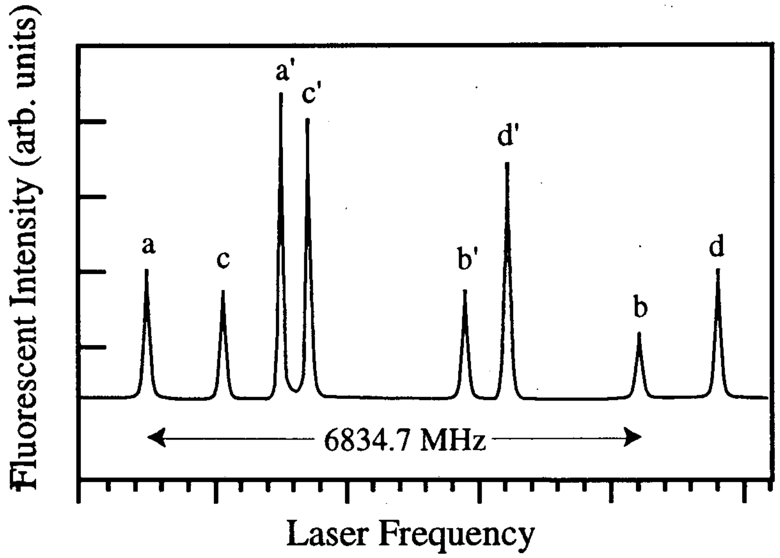

Figure 3.3 Expected fluorescence spectrum for natural abundance rubidium. The letters above the resonances correspond to the transitions in figure 3.2.

The practical applications of optical pumping were advanced with the discovery of spin exchange, the transfer of electronic polarization to nuclear polarization. The earliest experiments were performed by Dehmelt, who observed that optically pumped sodium atoms in the presence of free electrons subsequently became polarized[75]. Spin-exchange makes it possible to polarize systems that cannot be polarized directly. For example, of the noble gases, only ^{3}He is able to be polarized directly[76], making spin-exchange a very important technique. Happer and coworkers have extensively studied high xenon nuclear spin polarization in rubidium pumping cells[77,78]. Xenon is a particularly favorable spin-exchange partner with Rb because it forms long lived van der Waal's complexes[79-82]. The Hamiltonian is given by

$$\mathrm{H} = A\vec{S}\cdot\vec{I} + \gamma\vec{S}\cdot\vec{N} + \alpha\vec{S}\cdot\vec{K} + g_S\mu_B\vec{B}\cdot\vec{S} + g_I\mu_B\vec{B}\cdot\vec{I} + g_K\mu_B\vec{B}\cdot\vec{K} + \ldots \qquad 3.1$$

where $\vec{I}$, $\vec{S}$, $\vec{K}$, $\vec{N}$, are angular momentum vectors for the rubidium nuclear spin, the rubidium electron spin, the xenon nuclear spin, and the rotational angular momentum of the complex respectively. Their relationship is depicted schematically in figure 3.4. A is the isotropic hyperfine interaction between the Rb electron spin (S) and the Rb nuclear spin (I), γ is the spin-rotation constant for the complex, α is the isotropic hyperfine interaction between the rubidium electron spin (S) and the nuclear spin of xenon (K), μ_B is the Bohr magneton, and g_I, g_S, and g_K represent the g-factors for the spin species I, S, and K, respectively.

The Fermi contact interaction, $\alpha\vec{S}\cdot\vec{K}$, can be expanded in a spherical basis and written as

$$\alpha\vec{S}\cdot\vec{K} = \frac{8\pi}{3}\gamma_e\gamma_{Xe}|\Psi(0)|^2\left[K_zS_z + \frac{1}{2}(K_+S_- + K_-S_+)\right] \qquad 3.2$$

where γ_e and γ_{Xe} represent the gyromagnetic ratios of the electron and the xenon nucleus respectively. $|\Psi(0)|^2$ is the probability of finding unpaired spin density at the xenon nucleus. The exchange terms K_+S_- and K_-S_+ lead to polarization transfer from the rubidium electron spin to the xenon nuclear spin. Polarization not transferred to the xenon is lost to rotational angular momentum of the complex, which is subsequently dissipated as translational energy when the complex is broken apart in another collision. The Fermi contact interaction is particularly large for xenon due to the polarization of the Xe core s orbitals by Rb 5s electrons during a collision[83,84]. The van der Waals mechanism (figure 3.5) is dominant when the collision limited lifetime of the complex is long and the magnetic field strength < 100 G. In higher fields and/or at higher pressures, the dominant mechanism for spin-exchange becomes binary collisions[85].

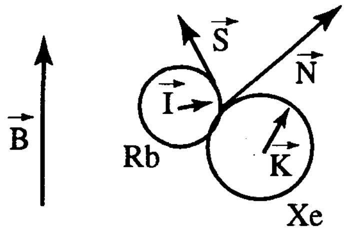

Figure 3.4 Schematic of Rb-Xe van der Waal's molecule with the angular momentum vectors labeled.

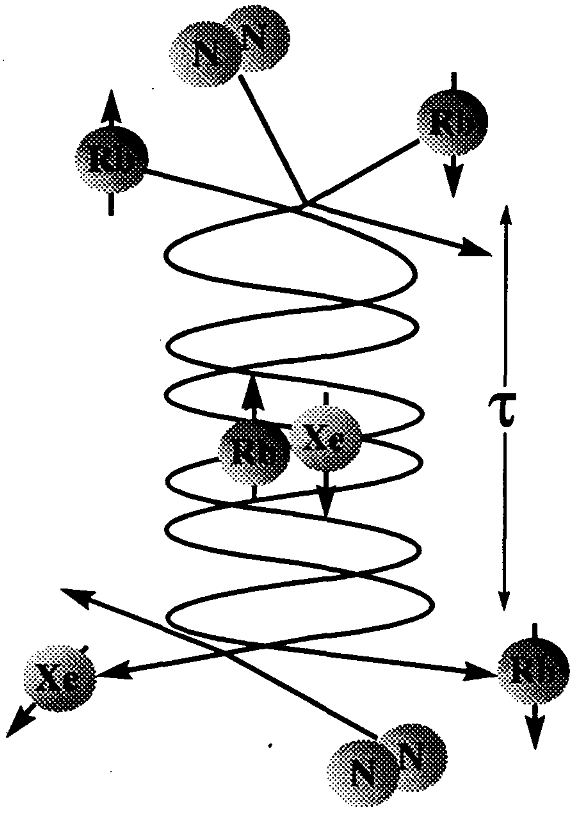

Figure 3.5 Schematic of Rb-Xe spin van der Waals interaction.

3.2 Hardware

3.2.1 Xenon preparation

The optical pumping apparatus, shown in figure 3.6, is similar in design to that of Raftery et al.[15] The optical pumping cell, a 10 cm^3 glass cylinder, is placed in a magnetic field (~30 G) generated by a pair of Helmholz coils and is connected to the sample tube through glass transfer lines and separated by stopcocks for convenient gas handling. The pumping cell is coated with a thin film of rubidium and can be heated by flowing nitrogen gas at 70-90 °C to increase the rubidium vapor pressure to approximately 6×10^{-6} torr to absorb the laser light. The xenon gas is stored in a sidearm of the pumping cell that also contains rubidium. The xenon is purified by this rubidium which reacts with impurities in the gas. Typically, 200-400 torr of xenon (approximately 10^{20} xenon atoms) are loaded into the pumping cell and irradiated for 30 minutes. The cell is then cooled to below 40 °C to lower the rubidium vapor pressure. The xenon gas is introduced to the sample tube with the tip submersed in liquid nitrogen in a 1 kG magnetic field. The sample tube is inserted into the SQUID spectrometer and NMR signals are acquired. Both isotopically enriched ^{129}Xe (80% , EG+G Mound) and natural abundance xenon have been used for optical pumping.

The cell is illuminated by circularly polarized light of 0.5 W from a CW tunable diode laser (Spectra Diode Laboratories). Circular polarization is achieved with the insertion of a quarter wave plate in the path of the pumping beam. Deviations from linear polarization of the infra red laser light are minimized by the insertion of a linear polarizer inserted in the beam path prior to the quarter wave plate. The laser wavelength is tuned to the rubidium D1 optical transition at 794.7 nm and the fluorescence is monitored with an infrared viewer.

The SDL-8630 tunable cw laser diodes are designed to emit high-power near-diffraction-limited wavelength tunable beams. The output power (0.5 W), beam diameter (2mm FWHM), beam divergence (0.5 mrad FWHM), operating current (2.0 A), tuning range (25 nm), series resistance (0.25 Ω) and spectrum (≤ 10 GHz) are comparable to, though slightly lower and less flexible than argon ion laser-pumped titanium-sapphire or dye lasers. The SDL-8630 does not require a pump laser. Rather, it is electrically-pumped using a low amperage dc current source. Instead of being water cooled, the system is air-cooled by a 12V, 0.5 A muffin fan. Therefore, this laser is portable. The external-cavity tunable laser is formed using a tapered amplifier semiconductor chip as the active medium and a bulk diffraction grating as the tunable element. The conceptual design of the laser cavity and the beamshaping optics are described in the operations manual. The laser can be operated in a) single-mode operation or b) multi-mode operation. In multi-mode operation several external-cavity modes are observed, spaced at approximately 2 GHz intervals. Under single-mode operation, the instantaneous linewidth is expected to be ≤ 1 MHz. Currently, we are operating the laser in single mode. One important operating point that should be stressed is that a static-free environment is highly recommended since static discharge through the diode may result in irreparable damage. The diode on this laser is by far the most expensive component to replace. The price tag of this laser is perhaps its most attractive feature. The argon ion/titanium-sapphire laser system in the lab has a price tag of ~$70K, ($25-30K for the Ti:Sapphire and $45K for the argon ion laser that pumps it). The cost of the SDL-8630 is $15K. Furthermore, it does not require extensive connections to water and power. In order to minimize the startup cost of our experiments, an old SDL-820 laser driver that was already in lab was modified to function as a SDL-824 laser driver, which is designed to power the SDL-8630 laser. A nice feature of both drivers is that the power requirement is only a single 120 VAC line outlet, making the laser/driver system completely portable. The only differences between the laser drivers are a warning light control, remote interlock control, and cooling fan driver. The cooling fan driver is critical to the operation of the diode laser. Power is supplied by a 12 V, 0.5 A external power supply routed into pin 5 of the cable, with the negative running to ground.

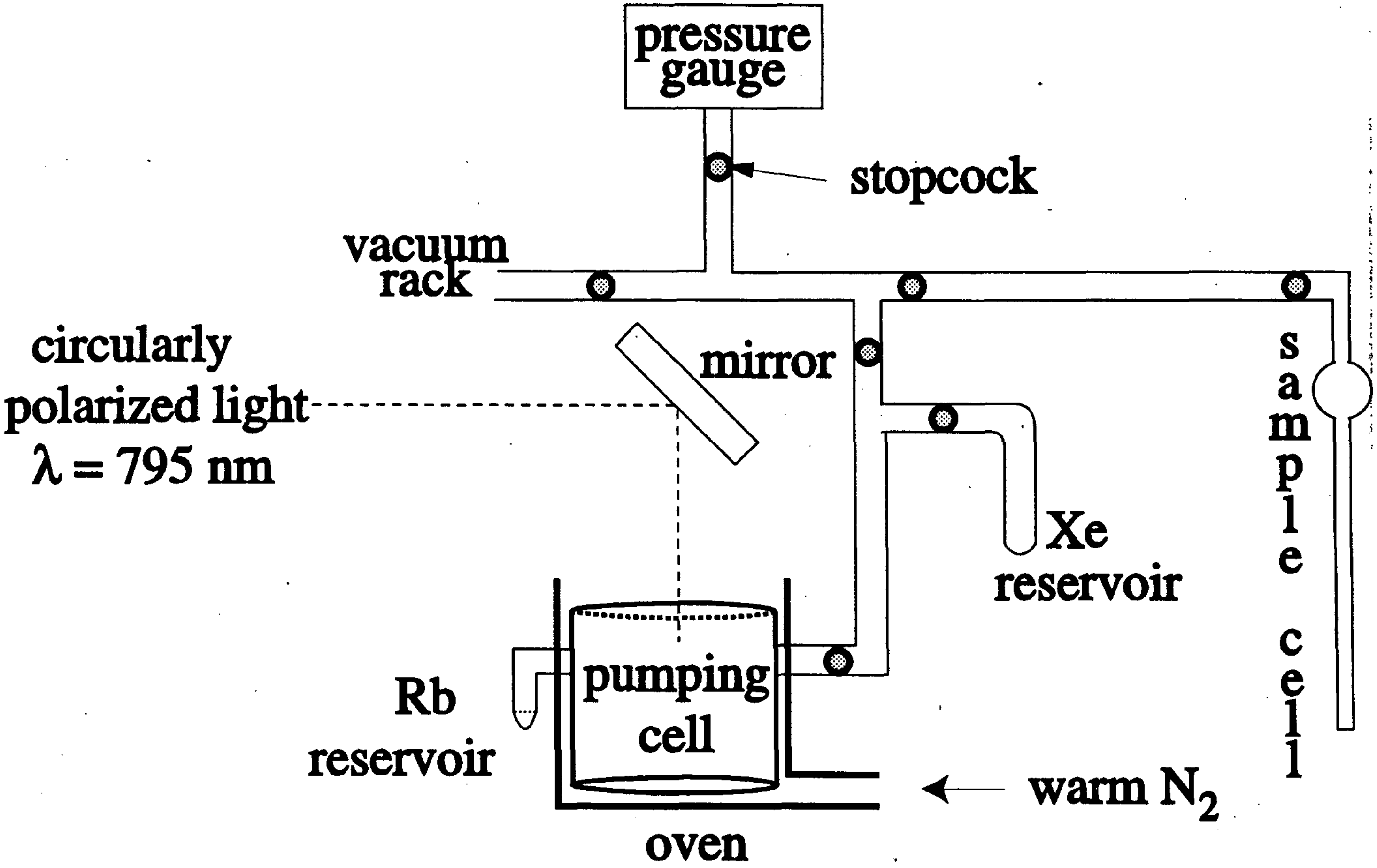

Figure 3.6 Schematic diagram of the optical pumping cell. Circularly polarized 794.7 nm laser light is steered through the optical pumping cell. The heated flowing nitrogen gas that is used to maintain the pumping temperature is depicted in the bottom of the figure.

3.2.2 Spectrometer overview

Figure 3.7 shows a schematic of the pulsed SQUID NMR probehead. A detailed description of the spectrometer, developed by TonThat and Clarke, can be found in ref [65]. The probehead containing the SQUID, sample, pickup circuit and rf and static magnetic field coils are immersed in liquid helium. The pickup circuit, a nonresonant superconducting circuit, acts as a flux transformer, which couples the sample to the SQUID input coil. The pickup coil (the sample part of the pickup circuit) is a saddle coil which surrounds the sample. A second saddle coil surrounds the pickup coil and is used to generate the B_1 field by RF excitation. This coil is oriented orthogonally to the pickup coil to minimize the mutual coupling of the excitation pulse into the SQUID. The pickup coil, RF coil, and sample are surrounded by a superconducting solenoid which generates a magnetic field up to 100 G. The magnetic field may be changed by the use of a persistent current switch. This represents an improvement over the CW probe described in Chapter 2, in which the entire probe was lifted out of the liquid helium bath to make the solenoid non-superconducting.

A schematic of the SQUID spectrometer is shown in figure 3.8. The SQUID is operated in a modified flux-locked loop using a modified version of the Direct Offset Integration Technique (DOIT) introduced by Drung[86]. An Additional Positive Feedback (APF) scheme is employed in order to produce a larger transfer function ($\Delta V/\Delta\Phi$) to maximize the operation of the spectrometer[87]. The signal, which is fed back to the SQUID to maintain a constant flux, is connected to a buffer amplifier to reduce feedback of external noise.

In the CW spectrometer described in Chapter 2, the RF excitation frequency in theory is limited only by the low pass filter used to remove the coupling of rf into the pickup circuit. The change in longitudinal magnetization as a result of RF excitation was near dc. The pulsed spectrometer detects transverse magnetization at frequencies that are close to the frequency of rf excitation, so the interactions that are studied must fall within the bandwidth of the spectrometer which is ~1.5 MHz. Its frequency response is limited by the readout electronics, specifically the gain bandwidth product of the preamplifier.

Since the SQUID is directly connected to the input of a room temperature amplifier, it is important that the amplifier have a low input voltage noise and be stable against current and voltage fluctuations, which can result in an interruption of flux locked operation. The voltage noise can be reduced at the expense of the current noise by a factor of $1/\sqrt{n}$ by connecting n preamplifiers in parallel. This is an effective means of reducing voltage noise as long as the current noise does not dominate. The AD797 preamplifiers currently in use have a voltage noise of 1 nV/$\sqrt{\text{Hz}}$. Because of the low impedance of the SQUID, the voltage noise dominates.

Precession of spins is induced by a magnetic field pulse with the feedback circuit disabled. An analog switch is used to short the integrator during a pulse in order to minimize the signal fed into the integrator to prevent it from saturating. After a pulse, flux locked operation is restored and the SQUID amplifier measure the signal produced by the free induction decay. Figure 3.9 illustrates the timing of the pulsed experiments with this spectrometer.

The spectrometer is run from a Macintosh computer which is interfaced to a Tecmag ARIES unit. The Tecmag ARIES comes equipped with its own internal 10 MHz clock, 12-bit ADC, and pulse programmer. The pulse programmer consists of a microcontrol word with a length of 78 bits that defines the state of the spectrometer at each instant. The position of these bits are defined and can be grouped together in the file CONFIG.CON. The ARIES also contains a slow input/output (SIO) module that can control various functions such as the frequency of one synthesizer, or different filter settings. A 12-bit general purpose register is also provided. In addition to the 12-bit general purpose register on the SIO module, the ARIES also provides 22 TTL lines on the spectrometer module available for the user (LP47-LP40 (8 bits), LP84-LP80 (5 bits), LP94-LP95 (2 bits), and LP127-LP121 (7 bits)). Through the use of the general purpose register and the 22 additional TTL lines in the spectrometer module, we have customized the ARIES to run our homebuilt spectrometer. Table 3.1 outlines the current configuration of the general purpose register on the SIO module and 22 TTL lines on the spectrometer module.

The ARIES is connected to a Sciteq DDS-1 Waveformer, which is a single-chip integrated direct digital synthesizer which includes all modulation capabilities. Through the Tecmag, we control the phase, frequency, and amplitude of the rf signal generated. The Sciteq frequency synthesizer works well for our frequency range, but because it is a nonstandard NMR frequency synthesizer (there are no standard synthesizers in the kHz range), we must manipulate the TTL configurations in order to interface the frequency synthesizer to the ARIES.

The frequency synthesizer provides 32 bits for the frequency. If all 32 bits are used in the user's application, the DDS-1 has a frequency range of 45% of the clock speed ($F_{clock} \leq 25$ MHz) supplied from an external source and a resolution of $F_{clock}/2^{32}$. The 10 MHz clock supplied by the Tecmag unit would provide essentially dc to 4.5 MHz with a frequency resolution of 2 mHz if all the bits were in use. Due to the limited number of TTL lines available for use, and the limited bandwidth of the spectrometer, our present configuration has a frequency range up to 2.5 MHz with a resolution of 19 Hz. This configuration uses 17 frequency bits starting with the third most significant bit. The frequency bits are split on the Tecmag, with 12 of them assigned to the general purpose register of the SIO module, and the remaining five assigned to TTL lines on the spectrometer module. This makes it somewhat inconvenient to input the frequency, since we cannot just type in the desired frequency. The SIO module requires input in hexadecimal format from the dashboard, while the spectrometer module requires input in decimal form in the pulse sequence. In order to compute the input parameters quickly, I have written a program that outputs the hexadecimal number that is input into the SIO module, the decimal number that is supplied to the TTL lines on the spectrometer module, and the actual frequency that is being output (which will be the desired frequency within the frequency resolution of our configuration).

The phase and the frequency share the 16 most significant bits. If all 16 bits are in use, then we have a phase resolution of <0.006 degree steps. Since current experiments do not require this degree of control, only the two most significant bits are used. This gives us a phase control of 0-90-180-270. The mode control words (MCW) and register control words (RCW) are required to toggle back and forth between phase and frequency. They can also be used to accumulate phase and frequency, althought this is not a feature of the synthesizer that we use.

There are 11 bits which control the amplitude, which is output at a maximum of 1 V. Therefore, if all the bits are in use, the DDS-1 provides an amplitude resolution of $1/2^{11}$ volts or ~0.0058 dB. Currently, we are using the eight most significant bits, providing a resolution of 0.004 V. The amplitude is strobed on and off by the use of one TTL line, which we have defined in the pulse sequence as an "amplitude control word" (ACW).

The signal that is generated in the Sciteq is passed through a low pass filter with a 3 dB point at 2.5 MHz. All output signals generate their alias frequency (F_{clock} - F_{out}) plus harmonics which can be removed with a low pass filter set to the highest operating frequency (usually 45% of clock frequency).

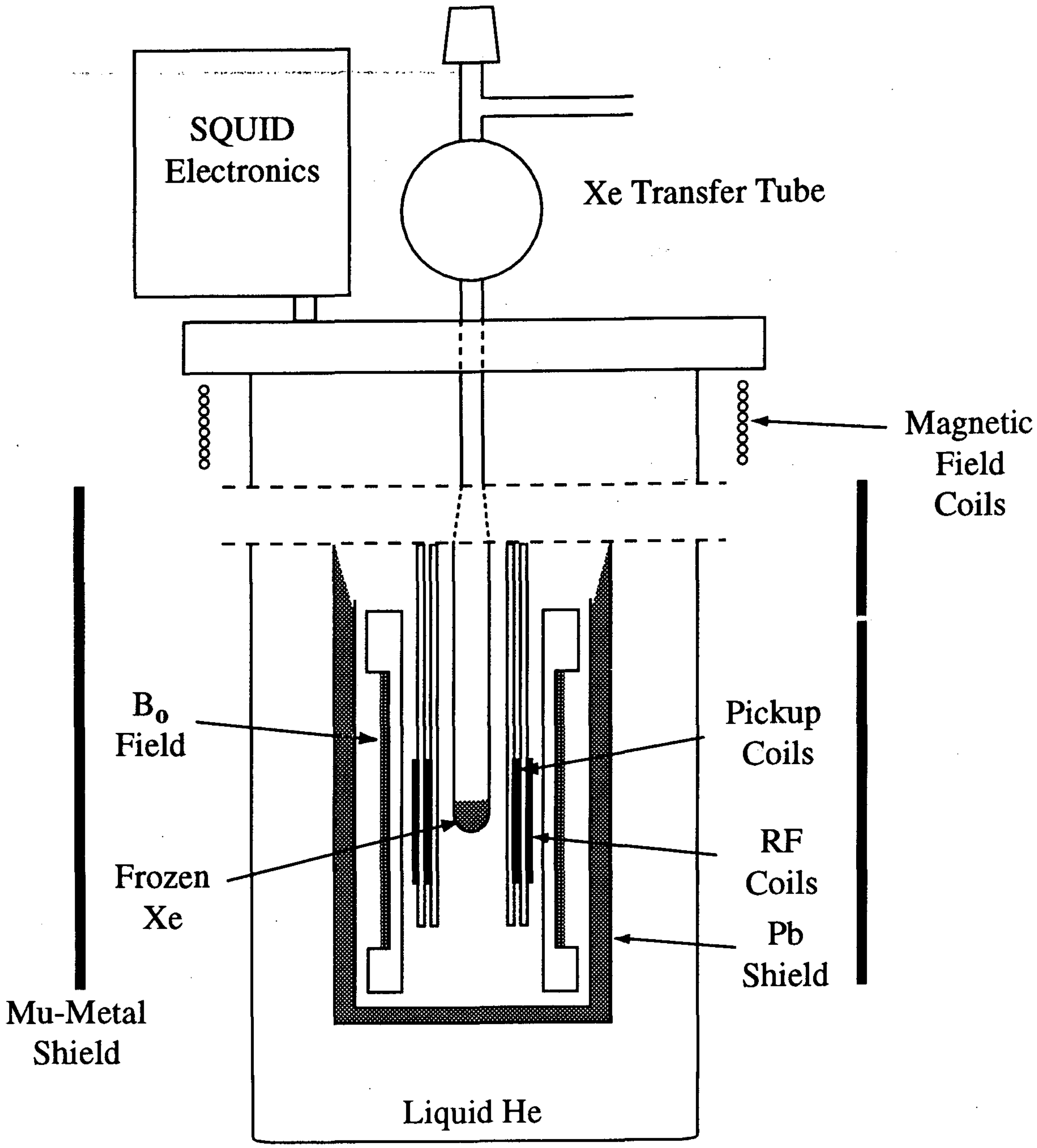

Figure 3.7 Schematic of pulse SQUID probehead.

Spectrometer Schematic

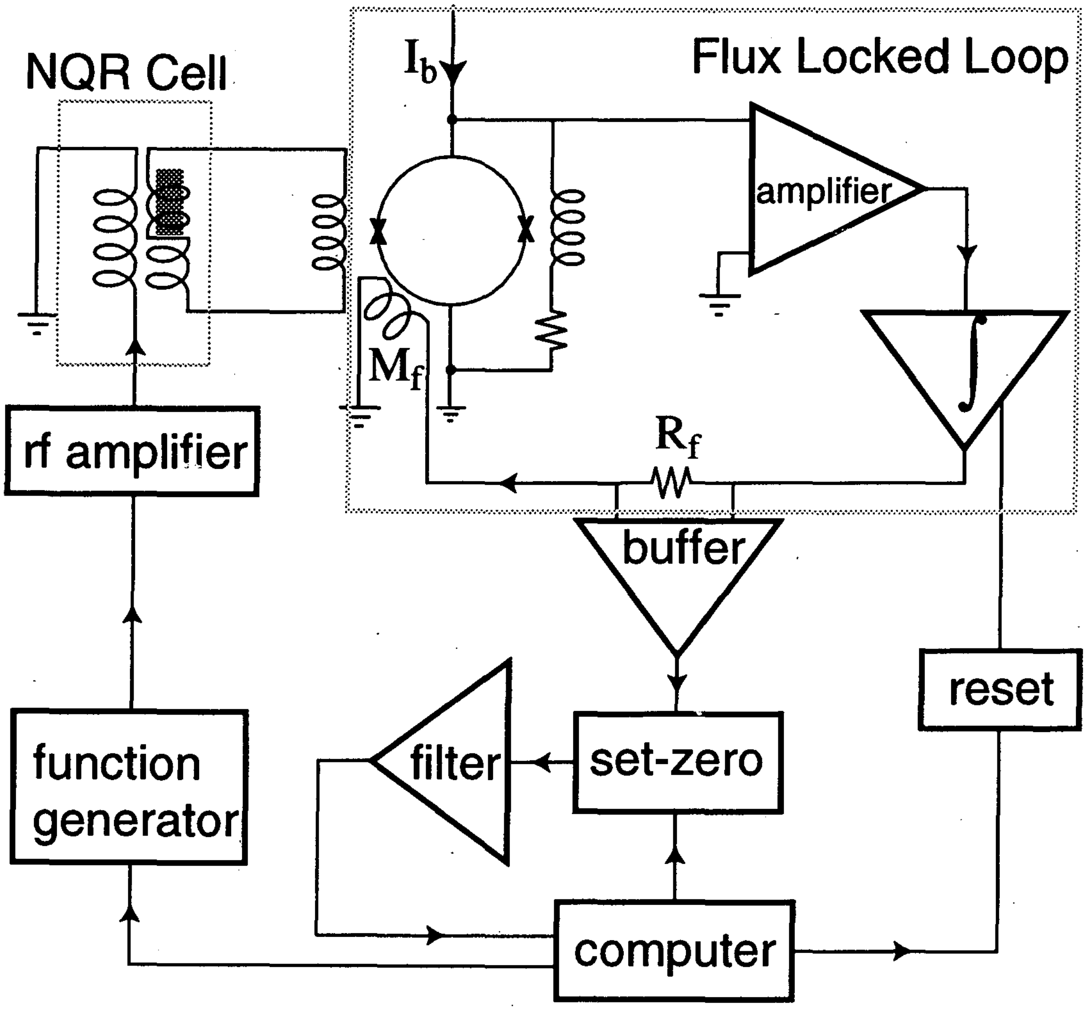

Figure 3.8 Schematic of SQUID spectrometer.

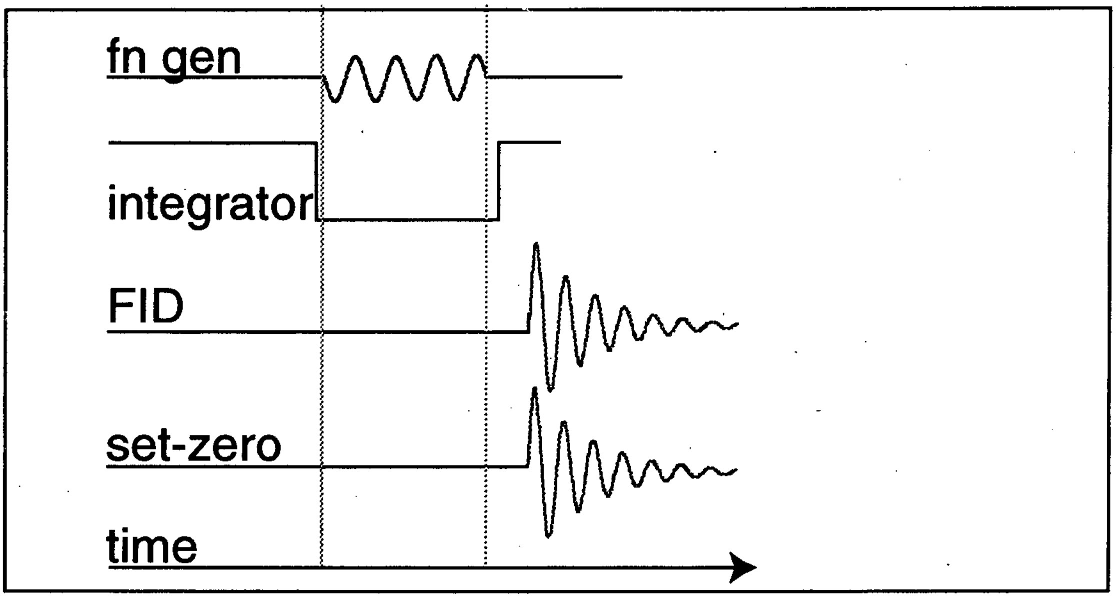

Figure 3.9 Timing diagram for pulsed SQUID spectrometer experiments.

parameter	# bits	TTL lines used
amplitude	8	LP40-LP47
phase	2	LP80-LP81
RCW	2	LP83-LP84
MCW	2	LP94-LP95
amplitude strobe	1	LP82
trigger 1	1	LP121
trigger 2	1	LP122
frequency *(spectrom. module)*	5	LP123-127
(gen. purp. register)	12	GP00-GP11

Table 3.1 TTL assignments for spectrometer parameters

3.3 Experiments and results

As was stated earlier, the ultimate goal of this project is to detect quadrupolar resonances from low spin density systems. To this end, some initial factors need to be established. First, we need to know the amount of polarization of the ^{129}Xe spins with our optical pumping apparatus and experimental setup. Second, we need to characterize the behavior of the polarized ^{129}Xe under our experimental conditions, specifically the polarization lifetime of ^{129}Xe at 4.2 K and the low magnetic fields that are generated by our spectrometer. Finally, we need to establish the necessary conditions and carry out the transfer of polarization from the laser-pumped ^{129}Xe to other spin species. We will first try this with some model systems ($^{13}CO_2$ and ^{131}Xe), and then progress to systems of interest to us.

3.3.1 Determining polarization enhancement with our optical pumping setup

The most straightforward approach to determining the polarization of ^{129}Xe with our apparatus would be to compare samples of ^{129}Xe with and without optical pumping. There are several difficulties associated with this approach. Given the size of our sample, it is not possible to acquire a single shot spectrum of ^{129}Xe without optical pumping. Because spin-lattice relaxation times at 4.2 K are very long (generally >1000 seconds), it is not practical to acquire a spectrum by run averaging. It is also not practical to increase the size of the non-pumped ^{129}Xe signal by increasing the number of spins because the size of the sample is fixed by the physical constraints of the spectrometer. Therefore, we turn to a comparison of the optically pumped xenon with unpumped xenon in the gas phase in a high field magnet. A standard containing 2.5 atms of enriched ^{129}Xe mixed with 100 torr O_2 (used to reduce the spin-lattice relaxation time of the ^{129}Xe) was used for comparison with our optically pumped sample. The standard was sealed in a sample tube designed to fit one of the probes used in the high field magnets. Our optically pumped sample, instead of being frozen into our sample tube, was collected into a sample tube identical to the tube containing the ^{129}Xe standard without freezing. The sample is quickly transported to and placed in the magnet and a spectrum is acquired. Because the high field magnets are located in a different room than our optical pumping apparatus, it is possible that some relaxation may occur, although this isn't expected to be large. Differences in the spin density are taken into account as well as any attenuation that is necessary to keep the free induction decay from clipping. While this method does not allow us to directly compare the polarization under our experimental conditions, it does allows us to monitor the efficiency of our optical pumping apparatus without having to cool the probe and consume liquid helium, which would simply be wasted when the pumping is not efficient. Figure 3.10 illustrates high field spectra comparing ^{129}Xe with and without optical pumping. The spectra were acquired with a chemical shift spin echo sequence. The optically pumped ^{129}Xe sample was 90 torr. 20 dB attenuation was used to acquire the optically pumped spectrum. The laser was operating in multi-mode. This particular spectrum represents a 4000 enhancement over the non-pumped spectrum.

Once the optical pumping efficiency is optimized, we need to measure the intensity of the signal with our spectrometer. Figure 3.11 shows a series of Larmor lines taken at different magnetic fields. Note that because we no longer have a Boltzmann distribution , the size of the signal is not dependent on the population differences of the energy levels, and therefore does not vary with applied magnetic field. The intensity of the Larmor lines is dependent on the efficiency of the optical pumping and of the subsequent handling and transfer to the spectrometer, so there may be variations in the signal to noise. These Larmor lines were acquired with an 8° pulse. A 90° pulse would result in a larger intensity, but at the expense of destroying all the longitudinal magnetization created by the polarization. Future cross polarization experiments will require a 90° pulse to maximize the transfer of polarization to another spin species, but for characterization of ^{129}Xe , a pulse with an 8° tipping angle allows us to pulse multiple times without having to repump the ^{129}Xe . These spectra were acquired immediately after the sample was inserted into the spectrometer. As the polarization decays, the relative intensity of the Larmor lines to each other will vary because of the strong magnetic field dependence on the polarization lifetime.[88] Note that an applied magnetic field of 1 G produces a Larmor frequency in ^{129}Xe of ~1 kHz, so the Larmor frequencies are also an indication of the applied magnetic field.

3.3.2 ^{129}Xe polarization relaxation measurements

At sufficiently low magnetic fields, the nuclear spin relaxation times depend strongly on magnetic field. At 4.2 K, the dependence on field persists up to 1 kG.[88] Gatzke *et al.* have argued that at temperatures below 20 K the cross relaxation of ^{129}Xe to ^{131}Xe is the source of the ^{129}Xe spin-lattice relaxation due to the dipolar spin-spin interactions. The isotope ^{131}Xe has spin I=3/2 and therefore a nuclear quadrupole moment which interacts strongly with electric field gradients producing rapid nuclear spin relaxation in accordance with van Karanendonk's theory[89,90]. Cross relaxation at low temperatures relies on a degeneracy of the energy levels of the two magnetic species and the presence of dipolar spin-spin interactions which can induce spin exchange transitions between them[91]. This degeneracy is a result of static ^{131}Xe quadrupole interactions with imperfections in the lattice, which previous studies have measured to be equivalent to the ^{131}Xe Zeeman energy at 7 G[92]. The reason that this field dependence persists up to 1 kG is that nuclei near grain boundaries are expected to have very large quadrupolar interactions, which are strong enough to produce the cross relaxation even in higher fields.

Gatzke *et al.* have reported long values of T_1 measured in frozen ^{129}Xe in the range from 50 G to 1000 G.[88] The theory of ^{131}Xe cross relaxation was confirmed by their observation of large ^{131}Xe polarization created. We have measured the spin-lattice relaxation times, T_1, of ^{129}Xe from the decay of the ^{129}Xe signal after optical pumping. The decays are significantly nonexponential. This is consistent with the expectation that the only sites where quadrupole interactions are likely to be strong enough to produce cross relaxation are localized near the surfaces of crystal grains, and that the transport of spin to these surfaces by spin diffusion is the limiting relaxation mechanism.[93] The decay curves are plotted as a function of time in figure 3.12. Figure 3.13 summarizes the spin lattice relaxation times calculated by an exponential fit of the initial decay in signal. For reference, the T_1 values acquired by Gatzke *et al.* are also plotted. We have found that the field dependence of T_1 saturates below 10 kHz at a value of approximately 2000 s. The long T_1 values even at small magnetic fields are promising for polarization transfer experiments.

3.3.3 Polarization transfer experiments

Up to this point, polarization transfer experiments have not been successful. This section is simply a summary of what has been previously attempted. We have tried to observe polarization created in ^{131}Xe and $^{13}CO_2$, both of which have been reported previously.[70,88]

The attempt to transfer polarization to ^{131}Xe was done by optically pumping natural abundance Xe following the same procedure as followed in the relaxation experiments of ^{129}Xe. It is possible that with the much larger concentration of ^{131}Xe , the cross relaxation is occurring faster than the timescale of the experiment. The presence of ^{131}Xe in the sample may make it much more sensitive to the change in magnetic field as the sample is brought from the horshoe magnet (which is at 1 kG) into zero field and then into the smaller field of the spectrometer.

The cross relaxation to $^{13}CO_2$ by low field thermal mixing has been done by Bowers *et al.* followed by detection of the chemical shift in high magnetic fields. We attempted to measure a ^{13}C Larmor line due to the cross polarization that was anticipated. Since the gyromagnetic ratios of ^{13}C and ^{129}Xe are very similar the static field was set high enough so that we could selectively excite either ^{129}Xe or ^{13}C. A new sample tube (figure 3.14) was constructed that had separate reservoirs for $^{13}CO_2$ and polarized ^{129}Xe. The ^{129}Xe was expanded into the bulb without freezing and in essentially zero magnetic field. The stopcocks between the two reservoirs were then opened and the gases allowed to mix. After the mixing period, the stopcock was opened to the evacuated tube with a precooled tip and the mixture was allowed to freeze in the bottom. We may not have seen a transfer of polarization because the ^{129}Xe relaxed before we could observe a signal, there wasn't sufficient mixing of the gases before freezing down, or that the $^{13}CO_2$ and ^{129}Xe were not well distributed in the frozen mixture.

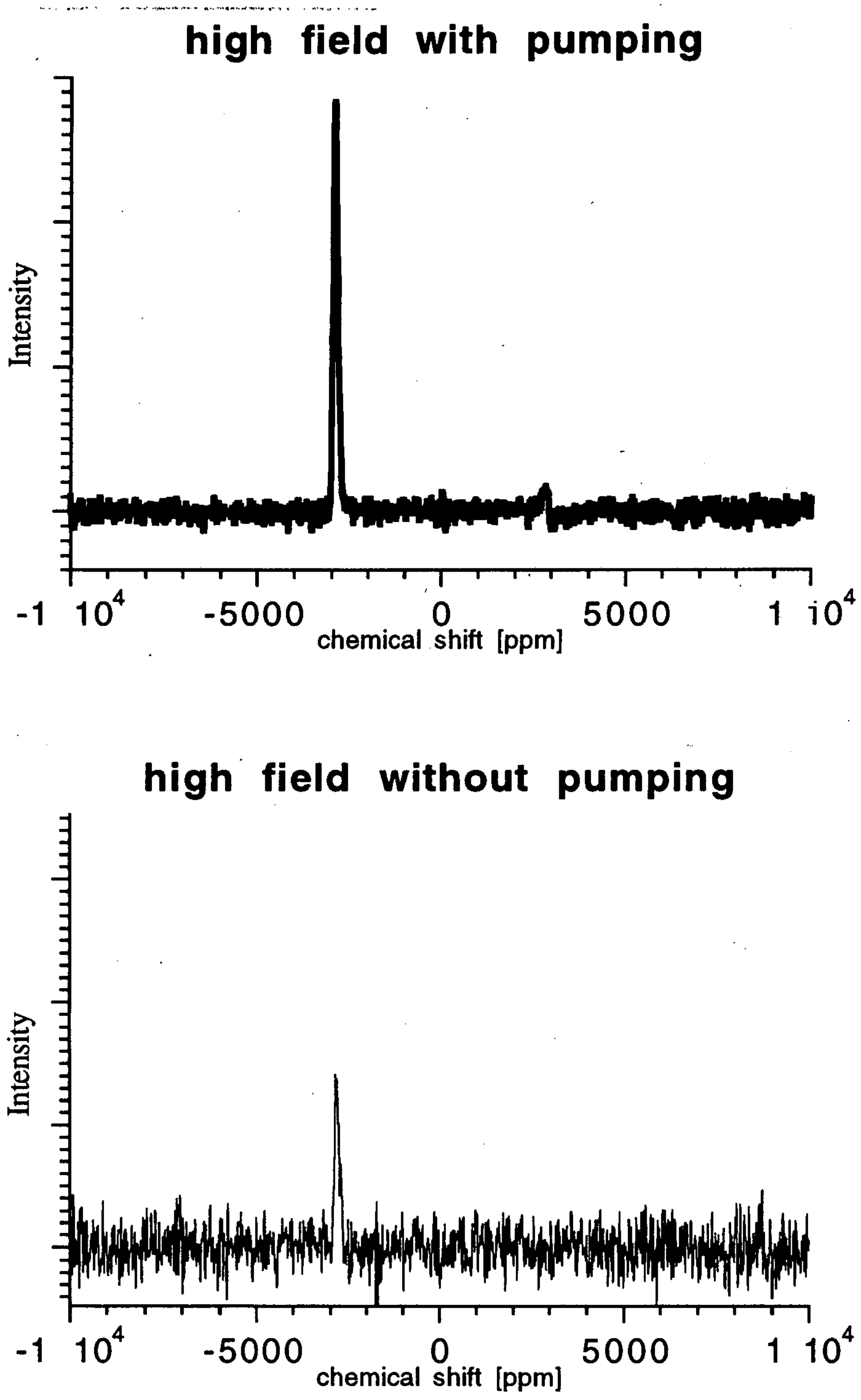

Figure 3.10 Demonstration of the enhancement of optical pumping. The spectrum with pumping represents an enhancement of 4000 over the spectrum without optical pumping.

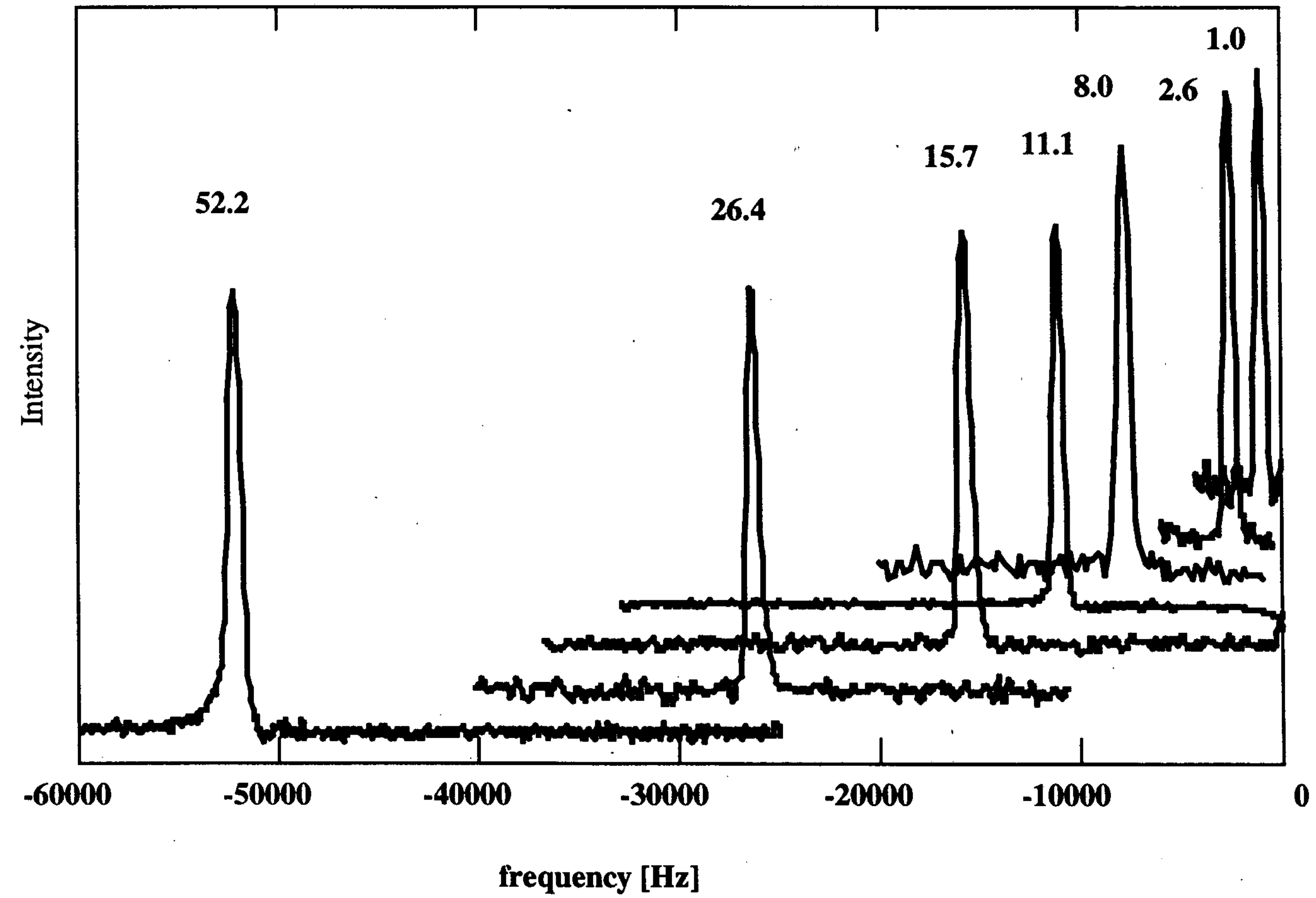

Figure 3.11 ^{129}Xe Larmor lines in the frequency range of the experiment

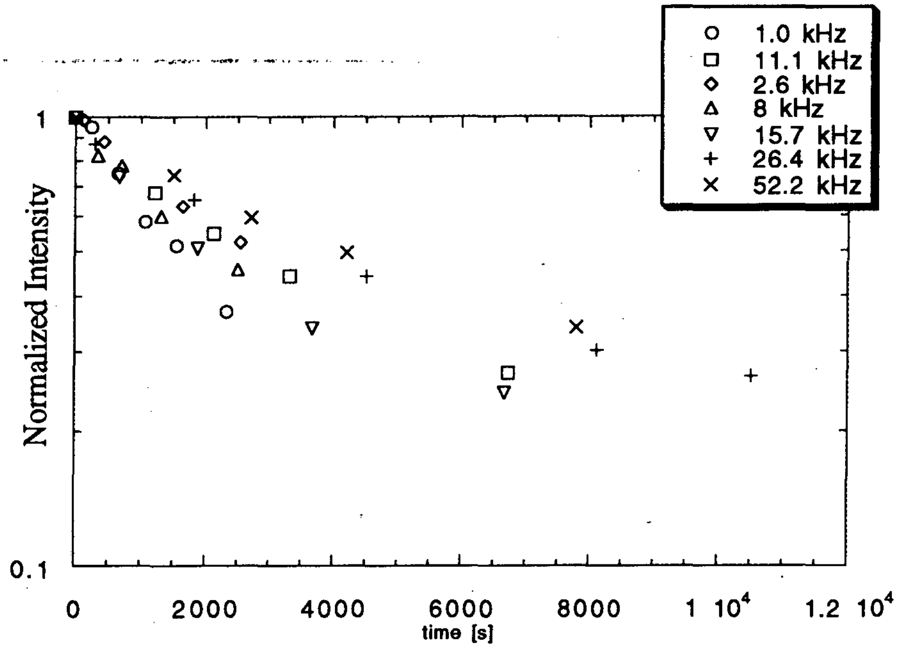

Figure 3.12 Relaxation curves for ^{129}Xe. The decays display significant nonexponential behavior.

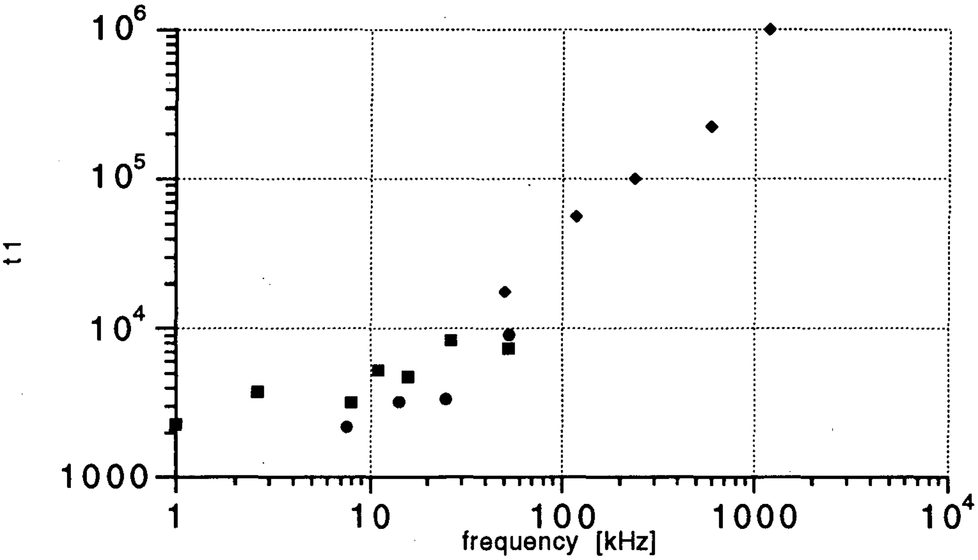

Figure 3.13 Summary of ^{129}Xe relaxation times as a function of magnetic field. The times were determined by fitting the initial decay to an exponential. The data is displayed in terms of the Larmor frequencies of the ^{129}Xe. The diamonds represent the data from Gatzke *et al.* The squares and circles represent two different data sets.

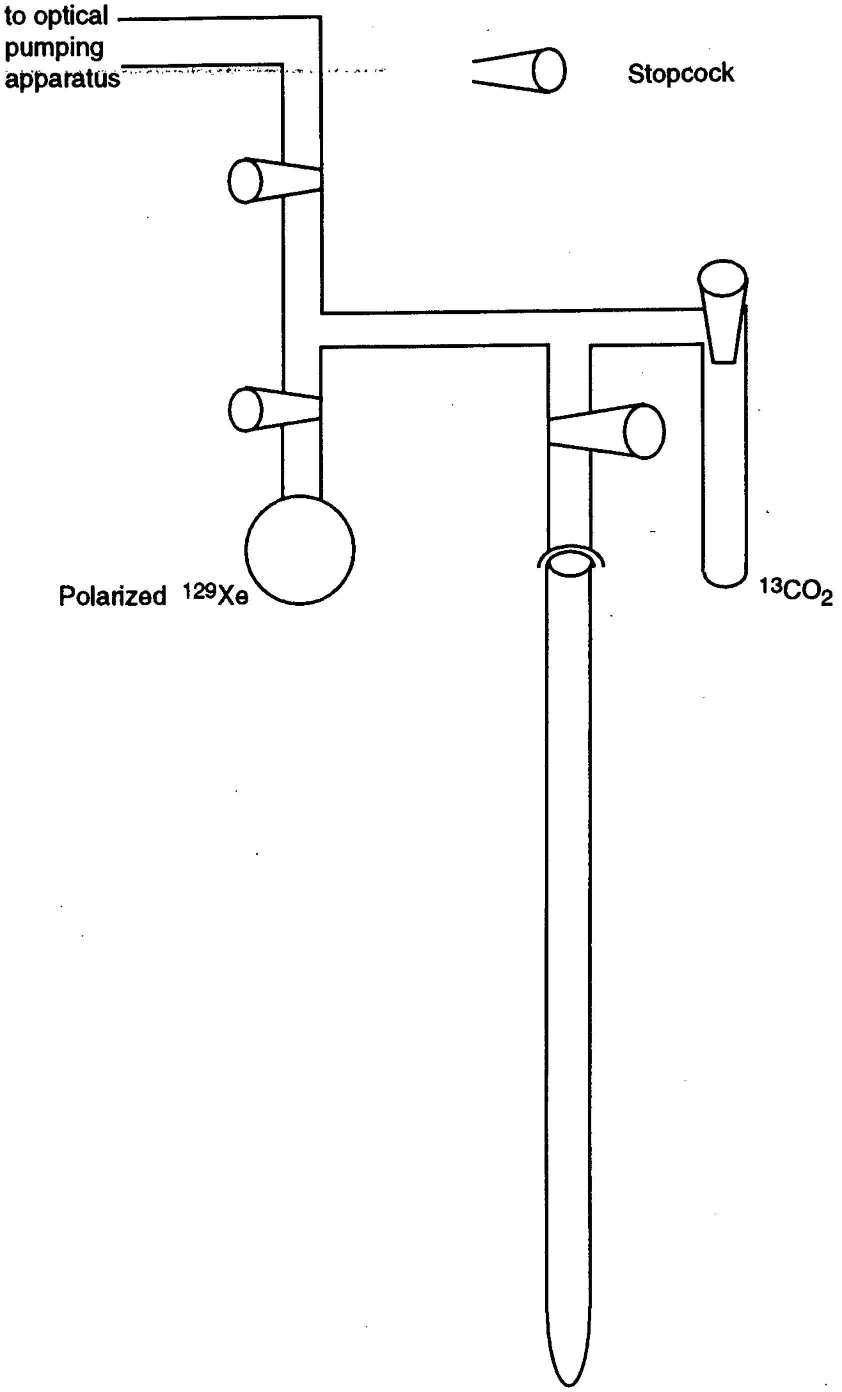

Figure 3.14 Sample tube constructed to cross polarize from ^{129}Xe to $^{13}CO_2$.

Chapter 4 ^{13}C Variable-Temperature CP/MAS Studies of $Hf(\eta^5-C_5H_5)_2(\eta^1-C_5H_5)_2$, $Zr(\eta^5-C_5H_5)_3(\eta^1-C_5H_5)$ and $Sn(\eta^1-C_5H_5)_4$ in the Solid State

Many organometallic compounds have been found to exhibit stereochemical nonrigid or fluxional behavior. For clarity[94], stereochemical nonrigidity is used in reference to molecules that undergo intramolecular rearrangements rapidly enough to influence NMR line shapes at temperatures within the practical range of experimentation. Fluxional behavior is characteristic of a large and important subclass of stereochemically nonrigid molecules in which all interconverting species that are observable are chemically and structurally equivalent. Fluxional motion in stereochemically nonrigid organometallic molecules has fascinated inorganic chemists since its discovery in $(\eta^1-C_5H_5)(\eta^5-C_5H_5)Fe(CO)_2$ by Piper and Wilkinson in 1956[95,96]. Based on the inert gas rule as well as chemical and infrared evidence, one pentahapto, $\eta^5-C_5H_5$, and one monohapto, $\eta^1-C_5H_5$, cyclopentadienyl (Cp) ring were anticipated. Therefore, it was anticipated that the proton NMR spectrum should consist of a singlet with relative intensity of 5 (due to the pentahapto Cp ring), an AA'BB' multiplet with relative intensity of 4, and a singlet with relative intensity of 1 (for the proton attached to the carbon sigma bonded to the metal center). When two singlets of equal intensity were observed, Wilkinson proposed that the monohapto group was involved in continual shifting of the Fe-C σ bond with concomitant rearrangements of the double bond system, or "ring whizzing", which was sufficient to cause spectrum averaging. This was subsequently confirmed ten years later by Bennett in a temperature-dependent study in which the expected spectrum was observed at -80° C and coalesced into a single peak when the temperature was raised[97]. It is somewhat remarkable that Wilkinson proposed such an explanation nine years before the publication of the theory which explained such a rearrangement by Woodward in 1965[98].

Considerable effort has been invested in studying the fluxional motion of cyclopentadienyl rings σ-bonded to metal centers in solution[94,99] and in the solid state[12,19,50,55]. Because these motions occur on an NMR timescale, a variety of techniques have been used to answer fundamental questions. (1) What is the activation energy of the rearrangement process, and (2) by what mechanism is it rearranging? Solution-state ^{1}H NMR has been used extensively in investigations of monohaptocyclopentadienyl-containing compounds. The majority of these techniques observe exchange broadening and coalescence or magnetization transfer[94,100]. These questions also arise in the solid state. Additionally, one may ask which fluxional processes exist in the solid state and to what extent do the activation energies of the two environments (solid and solution) differ. In the solid state, however, the problem is much more difficult as dipole-dipole interactions rule out high-resolution ^{1}H NMR and sites that are crystallographically inequivalent create difficulties in peak assignments. Fyfe and co-workers have detected sigmatropic rearrangements of the $(\eta^{1}\text{-}C_5H_5)$ rings of $Fe(CO)_2(\eta^{1}\text{-}C_5H_5)(\eta^{5}\text{-}C_5H_5)$ and $XHg(\eta^{1}\text{-}C_5H_5)$ (X= Cl, Br, I and $(\eta^{1}\text{-}C_5H_5)$) by ^{1}H wideline NMR[53,55]. Wemmer and Pines used double resonance NMR techniques coupled with lineshape analysis to study decamethylferrocene and hexamethylbenzene[50,56]. Heyes and Dobson have used ^{13}C cross-polarization (CP)/magic angle spinning (MAS) magnetization transfer experiments to study $Ti(\eta^{5}\text{-}C_5H_5)_2(\eta^{1}\text{-}C_5H_5)_2$, an analogous compound to $Hf(\eta^{5}\text{-}C_5H_5)_2(\eta^{1}\text{-}C_5H_5)_2$[101]. Recently two-dimensional (2D) exchange spectroscopy has been used to study fluxional motion in organometallic compounds in the solid state[102-106]. Two-dimensional experiments are desirable because they give information about all of the exchanging sites in the molecule simultaneously in contrast to magnetization transfer experiments which only provide information about exchange occurring at one site.

This chapter describes the solid-state variable-temperature (VT) 1D and 2D ^{13}C CP/MAS NMR of $Hf(\eta^{5}\text{-}C_5H_5)_2(\eta^{1}\text{-}C_5H_5)_2$, $Zr(\eta^{5}\text{-}C_5H_5)_3(\eta^{1}\text{-}C_5H_5)$ and $Sn(\eta^{1}\text{-}C_5H_5)_4$, which will be referred to as $HfCp_4$, $ZrCp_4$, and $SnCp_4$ respectively.

4.1 Sigmatropic rearrangements

Among the best understood of fluxional processes is the rearrangement of σ-polyenyl-metal systems including the rearrangements of σ-cyclopentadienyl complexes. In these compounds, the ring has been observed to undergo either a ring flip or a sigmatropic rearrangement, which shifts the identity of the carbon atom attached to the metal center[101,102]. A sigmatropic rearrangement [p,q] is defined as a concerted rearrangement in which a bond between two conjugated systems is broken at the same time that a new one is formed at the pth atom of one of the systems and the qth atom of the other[107]. In other words, in a sigmatropic rearrangement, a σ-bond formally migrates from one end of a π-system to the other, and the number of double or triple bonds reamins the same. If the migrating bond occurs across the same face of a π-system, the migrating bond is said to be *supra*facial. If the migrating bond bridges opposite faces of the π-system, it is said to be *antara*facial. A two-number classfication system is used for sigmatropic rearrangements. The numbers, which are set in brackets ([p,q]), represent the distance, in atoms, over which the bond moves. Most sigmatropic rearrangements of σ-cyclopentadienyl complexes appear to occur by Woodward-Hoffman allowed *supra*facial [1,5] shifts. In these systems the shifts are equivalent to [1,2] shifts and are thus indistinguishable from those expected on the principle of least motion. [1,3] shifts are expected to be *antara*facial and therefore highly disfavored.

4.2 CP/MAS

Although cross polarization and magic angle spinning are standard techniques of high field NMR, I feel that a short description is necessary because it is very different from the SQUID techniques that have been described thus far. There are three main issues that need to be addressed in order to carry out solid state experiments in high magnetic fields: (1) The dipolar coupling between nuclear spins, (2) the small response of naturally abundant rare spins (e.g. 1.1% ^{13}C), and (3) the anisotropy of the interactions in solid samples. These are treated by decoupling, cross-polarization, and magic angle spinning, respectively. When the spinning speed is larger than the chemical shift anisotropy, we attain "liquid like" spectra (i.e. relatively sharp narrow lines due to the isotropic part of the chemical shift). Using these techniques comes at a cost. The cost is that useful information is suppressed, namely the anisotropic portions of the chemical shift. However, by using Herzfeld-Berger spinning sideband analysis of a spectrum whose spinning speed is smaller than the chemical shift anisotropy, we can recover the structural information from the CSA parameters. The Herzfeld-Berger sideband analysis is described in section 4.4.

4.2.1 Decoupling

Homonuclear dipolar coupling of rare spins is generally not an issue because the internuclear distance between nuclear spins of the same species is typically very large. However, heteronuclear dipolar coupling (coupling between ^{13}C and ^{1}H in our case) may be much more problematic. For example, if the heteronuclear dipolar coupling is stronger than the chemical shift interaction that is used to characterize and analyze chemical structure, then this information is lost. Therefore, the purpose of decoupling experiments is to suppress the effect of dipolar coupling while retaining the interactions of interest.

The Hamiltonian for the system in the presence of dipolar and chemical shift interactions is given by

$$\mathcal{H} = \mathcal{H}_{Z_I} + \mathcal{H}_{CS_I} + \mathcal{H}_{Z_S} + \mathcal{H}_{CS_S} + \mathcal{H}_{\mathcal{D}_{II}} + \mathcal{H}_{\mathcal{D}_{IS}} + \mathcal{H}_{rf} \qquad 4.1$$

where the Hamiltonians have been previously defined in chapter 1 and the I and S subscripts refer to the abundant (proton) and rare (carbon) spins, respectively.

In the doubly-rotating frame, retaining only the secular parts of the heteronuclear dipolar Hamiltonian,

$$\mathcal{H} = \omega_{oI}\sigma_I S_Z + \mathcal{H}'_{\mathrm{DI}} - \omega_D I_Z S_Z + \omega_{oS}\sigma_S S_Z + \mathcal{H}'_{rf}, \qquad 4.2$$

where $\mathcal{H}'_{\mathrm{DI}}$ and $\mathcal{H}'_{rf}$ are the homonuclear I-spin dipolar and rf Hamiltonians in the new frame of reference, respectively. Only the last three terms of the Hamiltonian affect the S spins: the heteronuclear dipolar interaction, the chemical shift, and the applied rf. From the point of view of the S spins, the heteronuclear dipolar interaction has the same form as the chemical shift ($\propto S_Z$). Therefore, if we are to remove the heteronuclear dipole interaction while retaining the chemical shift interaction, we need a technique which will affect the I spins without affecting the S spins. This is achieved with the use of decoupling. In principle, spatial averaging (MAS) could eliminate the dipolar interaction, but in practice the dipolar coupling is usually too strong.

We can do either pulsed or continuous-wave decoupling. Under pulsed decoupling, the evolution due to the action of the heteronuclear dipolar coupling in one (or several) time interval(s) is canceled by its evolution in subsequent interval(s). This is practical only if the I spin(s) in contact with the S spin is not sufficiently coupled to other I spins. (i.e. if spin diffusion between I spins is not particularly efficient) If this is not the case, the evolution in the subsequent interval(s) cannot completely compensate for the interaction in the initial interval(s). To prevent this, the pulse spacing must be shorter than the time over which mutual spin flips occur (T_{2I}). Therefore, we have the requirement that

$$t_c/2 < T_{2I} \qquad 4.3$$

where t_c is the cycle time.

In cw decoupling, the interfering nucleus is continuously excited and the S spin will appear to evolve independent of the heteronuclear interaction with the I spins. A transient magnetization of the S spins is created by the application of a $\pi/2$ pulse followed by the application of a decoupling field at the I-spin resonance frequency during which time the evolution of the S magnetization is observed. In order for cw decoupling to be effective, the decoupling field must be large enough to influence the eigenstates of the system. This can be illustrated by observing the Hamiltonian for the system transformed into the "doubly-rotating-tilted-rotating" frame.

$$\begin{aligned} \mathcal{H} = {} & \omega_{oS}\sigma_S S_Z + \omega_{oI}\sigma_I I\left[I^{-}\exp(i\omega_1 t) + I^{+}\exp(-i\omega_1 t)\right] \\ & -\omega_D\left[I^{-}\exp(i\omega_1 t) + I^{+}\exp(-i\omega_1 t)\right]S_z . \end{aligned} \qquad 4.4$$

This frame assumes that the largest magnitude in the doubly rotating frame is the rf excitation of the I spins. Notice that all terms except the chemical shift of the S spin oscillate at a frequency, ω_1, which depends on the strength of the decoupling field. If ω_1 is large with respect to the spectral width of the chemical shift spectrum, the effect of these terms will not be seen. What is the lower bound on the strength of the decoupling field? The amplitude of the rf field must be larger than the magnitude of the homo- and heteronuclear dipolar coupling of the I spins.

Homonuclear decoupling of the I spins can be accomplished by irradiation of the I-spin system. However, arbitrary radiation can cause rapid destruction of the I-spin magnetization. An alternative approach is to prepare the I-spin system so that it is spin-locked by the decoupling field. Spin locking is achieved by creating a transverse I magnetization along the y-axis with a 90^o_x pulse followed by producing an rf field in the y direction (see figure 4.1). The natural motion of the spins is to precess around B_{1y}. The magnetization lifetime is characterized by $T1\rho$, which is composed of spin-spin and spin-lattice relaxation times. If B_1 is large, $T1\rho$ is large.

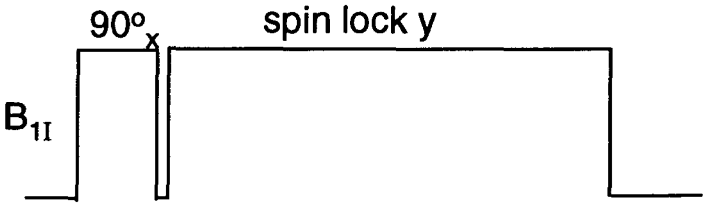

Figure 4.1 Spin-lock decoupling that preserves the magnetization of the I-spin system.

4.2.2 Cross Polarization

The same strong dipole-dipole coupling between rare and abundant spins that make observation of the rare spins difficult when used appropriately permits an enhancement of the rare-spin signal. This is a big advantage! In some cases, it makes the study of a rare-spin system possible. To get a sense of CP we will illustrate it with a thermodynamic approach. An excellent quantum mechanical description may be found in Slichter[42]. There are three basic steps to a CP experiment: 1) the reduction of spin temperature of the I reservoir; 2) polarization transfer between the I and S reservoirs; and 3) observation of the S spin (see figure 4.2).

Consider a system of N_I spins with gyromagnetic ratio γ_I and spin temperature T_I and N_S spins characterized by γ_S and T_S. The I and S spin systems form reservoirs that can be in contact with each other and with the lattice (which is effectively an infinite reservoir). Initially, the I spin reservoir is in thermal equilibrium with the lattice (i.e. it is characterized by spin temperature T_L). In thermal equilibrium, the I spins yield a magnetization of

$$M_I^{(0)} = \beta_L C_I B_o, \tag{4.5}$$

where $\beta_L = \hbar / (kT_L)$ is the inverse lattice temperature and C_I is the Curie constant

$$C_I = \frac{1}{3}\gamma_I^2 \hbar I(I+1)N_I. \tag{4.6}$$

By means of a $\pi/2$-pulse followed by the application of an rf field B_{1I} phase-shifted by 90^o, the magnetization is spin-locked in the rotating frame. Since the polarizing rf field is relatively small, $B_{1I} << B_o$, the locked magnetization $M_I(0)$ appears to correspond to a much higher inverse spin temperature β_o, such that

$$M_I^{(0)} = \beta_o C_I B_{1I} \tag{4.7}$$

where

$$\beta_o = \beta_L \, (B_o/B_{1I}). \tag{4.8}$$

The energy of the spins system is

$$E = -\beta_o C_I B_{1I}^2. \tag{4.9}$$

Next we need to accomplish a transfer of this polarization from the I to the S spins. To do this we will exploit a phenomenon first noticed by Hahn that alternating magnetic fields have a negligible effect on nuclei unless the frequency of alternation is close to the precession frequency. Thus if he applied two alternating fields at frequencies ω_I and ω_S, the frequencies being chosen to satisfy the respective resonance conditions

$$\omega_I = \gamma_I B_o \quad \text{and} \quad \omega_S = \gamma_S B_o \qquad 4.10a,b$$

each species could be viewed in its own rotating reference frame.

Consider spin systems consisting of spin species I and S that can exchange spin energy when two strong rf fields B_{1I} and B_{1S} are simultaneously applied at the I and S Larmor frequencies. The rate of energy exchange strongly depends on the magnitudes of B_{1I} and B_{1S} and reaches a maximum when the Hartmann-Hahn condition

$$\gamma_I B_{1I} = \gamma_S B_{1S}. \qquad 4.11$$

is fulfilled[108]. This condition guarantees that the nutation frequencies ω_{1I} and ω_{1S} of the two nuclear species in their respective rotating frames are equal, which leads to a maximum exchange rate determined by the II and IS dipolar interactions.

After a sufficiently long contact between I and S spins, a thermodynamic equilibrium with equal inverse spin temperatures $\beta_{1I} = \beta_{1S}$ is reached. Since the energy is conserved, one obtains

$$E = -\beta_1 C_I B_{1I}^2 - \beta_1 C_S B_{1S}^2 = -\beta_o C_I B_{1I}^2. \qquad 4.12$$

If the Hartmann-Hahn condition is fulfilled, the resulting inverse spin temperature becomes

$$\beta_1 = \beta_o (1+\varepsilon)^{-1} \qquad 4.13$$

with

$$\varepsilon = \frac{\gamma_I^2 C_S}{\gamma_S^2 C_I} = \frac{S(S+1)N_S}{I(I+1)N_I} \qquad 4.14$$

The resulting magnetizations of the S and I spins become

$$M_S^{(1)} = \beta_1 C_S B_{1S} = (\gamma_I/\gamma_S)(1+\varepsilon)^{-1}\, \beta_L C_S B_o \qquad 4.15a$$

$$M_I^{(1)} = M_I^{(0)}(1+\varepsilon)^{-1}. \qquad 4.15b$$

This results in an enhancement of S magnetization over equilibrium by a factor

$$\eta = M_S^{(1)}/M_S^{(0)} = (\gamma_I/\gamma_S)(1+\varepsilon)^{-1}. \qquad 4.16$$

For cross-polarization from an abundant to a rare spin system, $\varepsilon << 1$. Therefore, the sensitivity enhancement is given by the ratio of the gyromagnetic ratios, which for a ^{13}C-

^1H system is ~4. On the other hand, very little of the I-spin polarization has been eliminated. Therefore, it is possible to repeat the sequence several times (multiple contacts) before allowing the abundant spins to repolarize. CP experiments were initially developed to measure the effect of a rare spin on an abundant spin system. Pines, Gibby, and Waugh developed the technique as it is practiced today, observing the rare spins enhanced by the abundant spins[107].

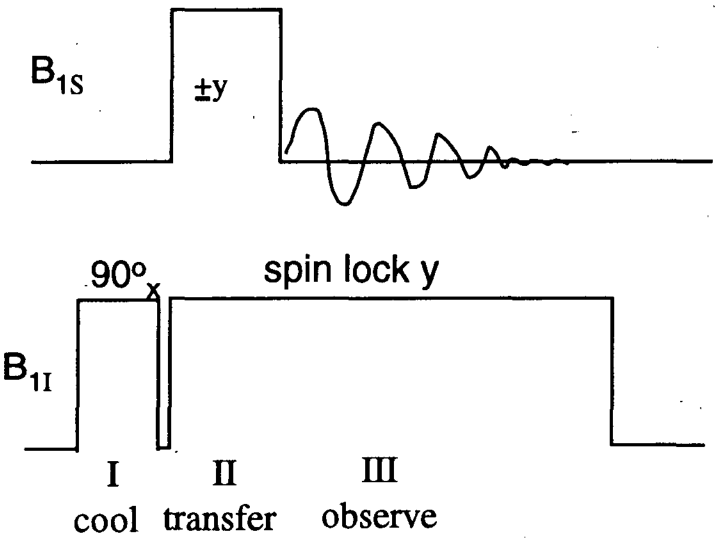

Figure 4.2 The spin-lock polarization transfer experiment showing the three domains.

4.2.3 Magic Angle Spinning

In general, even with proton decoupling, the ^{13}C spectra, dominated by the chemical shift anisotropy (CSA), is still considerably broadened. It was point out by Lowe [109]and Andrews[110] that spinning the sample about an axis inclined at 54°44' (the "magic angle") with respect to the applied static magnetic field will average the shift anisotropy to zero if the spinning rate exceeds the width of the CSA. The combination of high-power proton decoupling and MAS to resolve rare-spin spectra was first demonstrated by Schaefer *et al.*[111]. What follows is a description of the motional narrowing of the spectrum under magic angle conditions[45]. This will also lay the foundation for the discussion of the

Herzfeld-Berger spinning sideband analysis in a later section.

In the rotating frame, the Hamiltonian affecting the time evolution of the carbon spin system under strong proton decoupling is simply the secular part of the chemical shift:

$$H = \omega_{0I}\sigma I_{Z}. \qquad 4.17$$

where σ has the form

$$\sigma = \sigma_{iso} + (\delta/2)(3\cos^2\theta - 1) - (\eta/4)\sin^2\theta(e^{i2\phi} + e^{-i2\phi}) \qquad 4.18$$

and

$$\sigma_{iso} = \tfrac{1}{3}(\sigma_{xx} + \sigma_{yy} + \sigma_{zz}) \qquad 4.19a$$

$$\delta = \tfrac{2}{3}\sigma_{zz} - \tfrac{1}{3}(\sigma_{xx} + \sigma_{yy}) \qquad 4.19b$$

$$\eta = 3(\sigma_{yy} - \sigma_{xx})/(2\sigma_{zz} - \sigma_{yy} - \sigma_{xx}). \qquad 4.19c$$

It is most convenient to express the chemical shift interaction in terms of the spherical harmonics, which easily describe the effects of rotations.

$$\begin{aligned}\sigma &= \sum_{l=0}^{1}\sum_{m=-2l}^{2l}\sigma_{2l,m}Y_{2l,m}(\theta,\phi) \\ &= \sigma_{iso}(4\pi)^{1/2}Y_{0,0} + \delta\left(\frac{4\pi}{5}\right)^{1/2}Y_{2,0}(\theta,\phi) + \frac{\delta\eta}{2}\left(\frac{8\pi}{15}\right)^{1/2}\left(Y_{2,2}(\theta,\phi) + Y_{2,-2}(\theta,\phi)\right)\end{aligned} \qquad 4.20$$

Note that the chemical shift depends on the orientation of the chemical shift principal axes (θ,ϕ) relative to the magnetic field. The spins at this orientation have a resonance frequency $\omega_0\sigma$. Due to a dispersion of orientations of the principal axes in a powder, the resulting spectrum is a superposition of the resonances of all the spins in their various orientations.

In order to examine the effects of rotation about an axis inclined at an angle β to B_0, we need to transform our Hamiltonian. We can describe a rotation about a z-axis by the rotation matrix R_Z. Let z' be the axis of physical rotation. An Euler rotation by β about y of the original coordinate system places z along z'. A rotation $R(0,\beta,\omega_r t)$ about z' specifies the instantaneous form of $\mathcal{H}_{CS}$ in the system rotating at ω_r about z'.

$$\begin{aligned}\mathcal{H}'_{CS} &= R^{-1}(0,\beta,\omega_r t)H_{CS}R(0,\beta,\omega_r t) \\ &= \omega_o\sum_{l=0}^{1}\sum_{m=-2l}^{2l}\sigma_{2l,m}R^{-1}(0,\beta,\omega_r t)Y_{2l,m}(\theta,\phi)R(0,\beta,\omega_r t)I_z\end{aligned} \qquad 4.21$$

which in terms of the Wigner rotation matrices, $D^{2l}_{mm'}$ becomes

$$\mathcal{H}_{CS} = \omega_o \sum_{l=0}^{1} \sum_{m,m'=-2l}^{2l} \sigma_{2l,m} D^{2l}_{mm'}(0,\beta,\omega_r t) Y_{2l,m}(\theta,\phi) I_Z \equiv \omega_o \sigma(t) I_Z \quad 4.22$$

The observables in our experiment, $<I_x(t)>$ and $<I_y(t)>$, the expectation values of the transverse components of angular momentum, are given by

$$<I_R(t)> = \mathrm{Tr}\, \rho(t) I_R \qquad R=x,y \qquad 4.23$$

Recall

$$\rho(t) = U^{-1}(t)\rho(0)U(t) \qquad 4.24$$

where

$$U = T exp\left(-i\int_0^t H(t')dt'\right) = T exp\left[-i\int_0^t \omega_o \sigma(t') I_z dt'\right] \equiv e^{-i\theta(t)} I_z \qquad 4.25$$

and

$$\theta(t) = \omega_o \sum_{l=0}^{1} \sum_{m,m'=-2l}^{2l} \sigma_{2l,m} Y_{2l,m'}(\theta,\phi) d^{21}_{mm'}(\beta) \int_0^t \exp(-im'\,\omega_r t')dt' . \qquad 4.26$$

Thus,

$$<I_R(t)> = \mathrm{Tr}\, U^{-1}(t)\rho(0)U(t)\, I_R = \mathrm{Tr}\, \rho(0)U(t)\, I_R U^{-1}(t) \qquad 4.27$$

Note that this is a rotation of I_R about z by $\theta(t)$. Therefore

$$\begin{aligned}\langle I_x(t)\rangle &= Tr\rho(0)\exp[i\theta(t)I_z]I_x\exp[-i\theta(t)I_z] \\ &= Tr\rho(0)[I_x\cos\theta(t) + I_y\sin\theta(t)] \qquad 4.28a \\ &= \langle I_x(0)\rangle\cos\theta(t) - \langle I_y(0)\rangle\sin\theta(t)\end{aligned}$$

$$\langle I_y(t)\rangle = \langle I_y(0)\rangle\cos\theta(t) + \langle I_x(0)\rangle\sin\theta(t) \qquad 4.28b$$

If our initial state is the spins aligned along the x-axis of the rotating frame $\rho(0) \sim I_x$ then the observed response of the magnetization in the time domain is

$$\langle I_x(t)\rangle = \langle I_x(0)\rangle\cos\theta(t) \qquad 4.29a$$

$$\langle I_y(t)\rangle = \langle I_x(0)\rangle\sin\theta(t) \qquad 4.29b$$

and in the frequency domain, the observed expression is given by

$$\begin{aligned}I(\omega) &= \int_0^\infty \left[\langle I_x(t)\rangle + i\langle I_y(t)\rangle\right] e^{-i\omega t}dt \\ &= \langle I_x(0)\rangle \int_0^\infty e^{i\theta(t)} e^{-i\omega t}dt\end{aligned} \qquad 4.30$$

Notice that $\theta(t)$ (eq 4.26) is an oscillatory function of time. If ω_r is arbitrarily large, then these oscillatory effects are negligible. In addition, if m'=0, then there is also a static component of θ(t),

$$\theta(t) = \sigma_{static}\omega_o t \sum_{l=0}^{1}\sum_{m=-2l}^{2l}\sigma_{2l,m}Y_{2l,0}(\theta,\phi)d^{2l}_{m0}(\beta) \qquad 4.31$$

the amplitude of which is independent of ω_r. If ω_r is large enough to neglect oscillatory terms in eq. 4.26, the observed frequency spectrum will be

$$\begin{aligned} I(\omega) &\cong \langle I_x(0)\rangle \int_0^\infty e^{i\omega_o\sigma_{static}t}e^{-i\omega t}dt \\ &= \langle I_x(0)\rangle \delta(\omega - \omega_o\sigma_{static}) \end{aligned} \qquad 4.32$$

Under these conditions, the spectrum will consist of a sharp peak. Using equations 4.31 and 4.19 note that

$$\sigma_{static} = \sigma_{iso} + \frac{3\cos^2\beta - 1}{2}\frac{\delta}{2}\left[(3\cos^2\theta - 1) + \eta\sin^2\theta\cos 2\phi\right] \qquad 4.33$$

If $3\cos^2\theta - 1 = 0$ (i.e. $\theta = 54°44'$)

$$\sigma_{static} = \sigma_{iso} \qquad 4.34$$

for each orientation (θ,ϕ).

This illustrates the importance of MAS as an analytical tool. It is particularly useful for samples containing nuclei having a number of different chemical isotropic shifts.

4.3 1- and 2-D VT CP/MAS Experimental Results

All compounds were received in sealed glass ampoules. Samples were transferred from the ampoule to a 7 mm Zirconia MAS rotor in a drybox containing an inert nitrogen atmosphere. The remaining materials and rotors were stored in the drybox. Although at one point the inert nitrogen atmosphere was compromised, only the $SnCp_4$ appeared to have suffered degradation with time requiring the packing of a fresh sample.

Solid-state NMR spectra were recorded on a homebuilt spectrometer with a Tecmag Libra interface and a wide bore 300 MHz superconducting solenoid magnet. The ^{13}C CP/MAS spectra were recorded at 75.739 MHz by using a homebuilt ^{13}C-^{1}H double resonance MAS probe of Doty design[112] capable of high power proton decoupling. A CP sequence (figure 4.3) with alternate cycle spin-temperature inversion, a return of residual I magnetization to the z-axis, and a proton radio frequency field of 8.4 G (ν1 = 35.714 kHz) resulting in a 90° pulse length of 7 μs and a carbon-13 radio frequency field of 26.0 G (ν1 = 27.8 kHz) resulting in a 90° pulse length of 9 μs was used. The reason for the mismatch was probably that we were matched to a sideband. The CP contact time was 1 ms. Proton decoupling was applied during acquisition. 2D exchange experiments used the pulse sequence illustrated in figure 4.4.

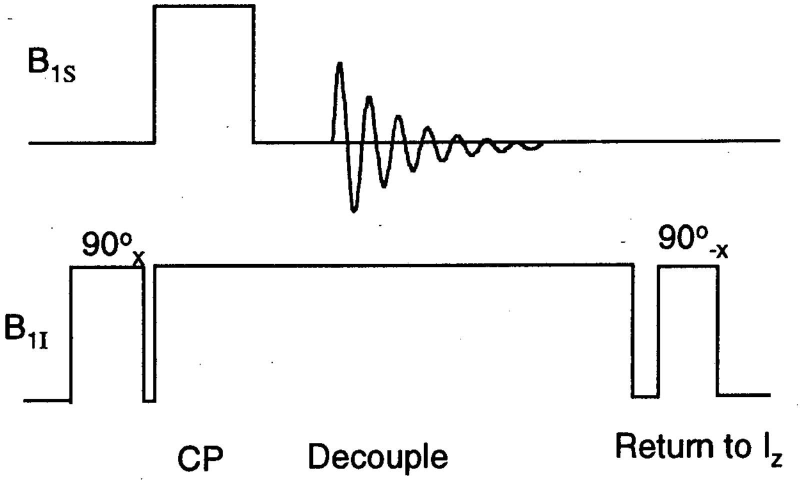

Figure 4.3 CP with spin temperature inversion pulse sequence.

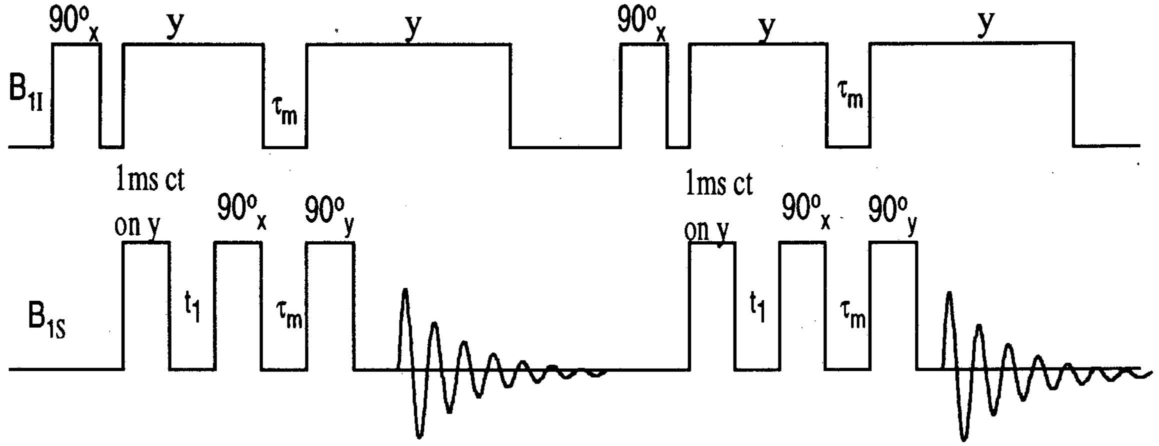

Figure 4.4 Pulse sequence for 2D-exchange experiments.

Temperature control was achieved with the flow of N_2 gas cooled by a heat exchanger from the top of the stack to the probe and was regulated by a Chemagnetics temperature controller. Temperature calibration below room temperature was achieved with a samarium acetate (III) tetrahydrate Curie law chemical shift thermometer[113]. The system was allowed to equilibrate at each new temperature for 20 minutes before spectral accumulation commenced.

The spinning angle was set to the magic angle by using the ^{79}Br resonance of a small amount of KBr. ^{13}C CP/MAS spectra were recorded at a range of temperatures from 153 K to 298 K at a typical MAS rotation rate of ~4 kHz. Chemical shifts were reported on a δ scale with respect to δ(TMS) = 0 and were referenced to the secondary standard adamantane.

4.3.1 HfCp$_4$

An attempt was made to study the dynamic behavior of HfCp$_4$ in solution using ^{1}H NMR spectroscopy[114] . The spectrum yielded a sharp singlet at room temperature at 5.86 ppm in CDCl$_3$ and 5.61 ppm in C$_6$D$_6$. This is similar to the spectrum of TiCp$_4$ in solution, which was subsequently determined by a temperature dependent study that η^1-Cp ring whizzing and η^5/η^1 ligand interchange were occurring at room temperature at rapid rates yielding a time average signal for all protons [115]. Low temperature studies (to 138 K) were performed with no subsequent change in the spectra, suggesting that the activation energies for intramolecular rearrangements in HfCp$_4$ are extremely low. In addition, static solid state ^{13}C NMR studies yielded chemical shielding tensor components of σ_{11}=177, σ_{22}=167, and σ_{33}=40. The MAS spectrum showed a singlet centered at 111.5 ppm.

We report variable-temperature (VT) 1- and 2-D CP/MAS spectra of HfCp$_4$. The structure of HfCp$_4$,**1** is shown in figure 4.5. One dimensional NMR spectra showed that the monohapto groups in **1** were exchanging rapidly at 298 K, and individual resonances for each carbon atom were observed when the sample was cooled to 173 K. Two-dimensional exchange spectra showed that the rings underwent a sigmatropic rearrangement rather than ring flips and that there were only two possible assignments for the carbon resonances. The final determination of the sigmatropic rearrangement mechanism will be possible when definitive peak assignments can be made. We believe

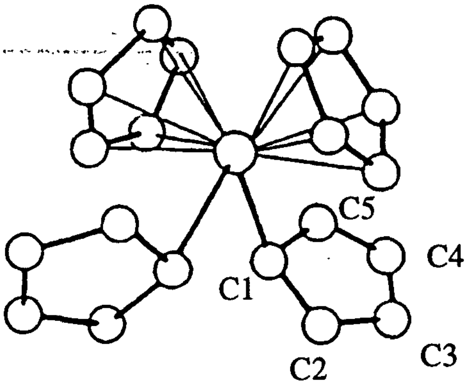

Figure 4.5 Representation of **1** as obtained from X-ray structure determination. The hafnium atoms resides on a crystallographic twofold axis. The η^1-C_5H_5 ring is labeled for discussion later in the section.

that this is the first NMR study of the fluxional motion of η^1-C_5H_5 groups in the solid state using 2D-exchange spectroscopy.

The ^{13}C CP/MAS NMR spectra of $HfCp_4$ in the temperature range between 153 K and 298 K are shown in figure 4.6 The spectrum at ambient temperature consists of a sharp peak at 113.0 ppm which shows an axially symmetric chemical shift anisotropy (CSA) tensor consistent with those know for typical M-(η^5-C_5H_5) moieties[101] due to averaging by the ring orientation process. This peak is assigned to the 10 carbon atoms of the two η^5-C_5H_5 rings. Rapid ring orientation is expected to average the carbon resonances of each individual ring and the molecular symmetry established in the diffraction study ensures the equivalence of the two rings. This resonance is imposed on a very broad resonance which is barely distinguishable above the noise.

At 173 K, five peaks are evident. The largest peak is still due to carbons in the pentahapto Cp rings. The four resonances at 90.0, 126.5, 127.9, and 130.7 are assigned to the monohapto group. Because the four resonances all have approximately equal integrated intensity, a fifth resonance for the monohapto Cp group is likely hidden under the pentahapto Cp resonance. Two dimensional results confirm this (vide infra). Upon heating from 173 K, the peaks for the $(\eta^1\text{-}C_5H_5)_2$ groups began to broaden and coalesce indicating that chemical exchange is occurring on the NMR timescale. Note that the X-ray diffraction data shows that all the molecules in the structure lie on a two-fold crystallographic axis such that the two σ-C_5H_5 rings in each molecule are related by symmetry[116]. The different chemical shifts must therefore reflect the different environments for each of the carbon atoms in an individual ring. The CSA parameters for each of these sites has been calculated by a program based on Herzfeld Berger calculations which are discussed in the next section.

Figure 4.7a shows the 2D exchange spectrum of **1** taken at 188K with a mixing time of 50 ms. The cross peaks indicate exchange between the resonances at 90.0 and 130.7, 90.0 and 113.0, 113.0 and 126.5, 126.5 and 127.9, and 127.9 and 130.7 ppm. Cross peaks between the resonances at 90.0 and 113.0 ppm, and at 113.0 and 126.5 ppm, are more intesnse than indicated in the spectra due to a negative intensity ridge at 113 ppm. Several conclusions about peak assignments and the dominant mechanism for rearrangement are drawn from the location and intensity of the cross peaks in the spectrum. First, the presence of a cross peak between the large peak at 113.0 ppm and the peaks at 90.0 and 126.5 ppm but not the peaks at 127.9 and 130.7 ppm indicates that one of the carbon resonances of the monohapto Cp groups is hidden underneath the pentahapto Cp resonance. Second, ring exchange between the monohapto and pentahapto groups as the dominant rearrangement mechanism at this temperature is ruled out by the absence of cross peaks between the 113.0 ppm and the 127.9/130.7 resonances. Third, the presence of cross peaks between the 90.0 ppm resonance (due to the carbon bound to the metal center) and the peaks at 113.0 and 130.7 ppm indicate that the primary rearrangement mechanism is not ring flips, because the carbon attached to the metal center would not exchange positions during a ring flip. When a longer mixing time (200 ms) was employed to allow multiple exchanges to occur, cross peaks were observed between all of the monohapto resonances (figure 4.7b) This further indicated that the rearrangement mechanism was not ring flips. Fourth, the absence of equal intensity cross peaks between all of the sites in figure 4.7a ruled out a sigmatropic rearrangement mechanism based upon random shifts. We therefore conclude that the dominant mechanism is either a [1,2] or [1,3] sigmatropic rearrangement.

Figure 4.8 shows the location of cross peaks between the different carbon resonances. Because the 2D results have shown unambiguously that the shift mechanism is a sigmatropic rearrangement, the cross peaks must correspond to one shift or rearrangement of the monohapto groups. From this information a connectivity pattern between peaks has been established. Given that the resonance at 90.0 ppm is the carbon attached to the metal center, a definitive assignment of the peaks can be made for either a [1,2] or [1,3] shift. Our results permit both the assignment of the ^{13}C resonances and the determination of the shift mechanism if either the assignments or the mechanism is known. Assignment of the individual sp^2 hybridized carbon resonances is not, however, straightforward. The resonance at 90.0 ppm is assigned to the carbon atom σ-bonded to the metal center. This is a reasonable assumption given that it is the only sp^3 hybridized carbon in the Cp ring and that sp^2 hybridized carbons typically resonate above 100 ppm.

It is interesting to compare our results with a recent solid-state NMR study of $Ti(\eta^5\text{-}C_5H_5)_2(\eta^1\text{-}C_5H_5)_2$ (**2**)[101]. X-ray crystallographic data shows that **1** and **2** have an almost identical solid-state structure. In the study of **2** a large peak at 117.3 ppm was observed for the pentahapto groups, and peaks at 89.3, 114.9, 121.8, 126.8, and 136.3 were observed for the monohapto groups. The peak at approximately 90 ppm (assigned to C1 in both **1** and **2**) are likely due to the same carbon in the monohapto Cp group. Although comparison of the assignments for the four downfield carbons (114.9, 121.8, 126.8 and 136.3 ppm) in **2** to **1** is somewhat ambiguous because of the differences in the observed chemical shifts between the two compounds, making the same assignment for the peaks at approximately 114 ppm observed in both experiments (assigned to C3 in **2**) would imply that a [1,3] shift is occurring, in contrast to the conclusions made by Heyes and

Dobson[101].

2 is currently being synthesized in order to compare the 2D NMR exchange spectra of **1** and **2**. Additional work that will be carried out by the next generation graduate student includes establishing the correct assignments of the monohapto Cp resonances by determining connectivity between neighboring carbons as is done in an INADEQUATE experiment. ^{13}C labeled **1** containing ^{13}C-^{13}C pairs is currently being synthesized in order to perform a 2D experiment in which spin-spin exchange between neighboring carbons is monitored rather than chemical exchange. These results should provide the definitive evidence required to correctly assign the peaks.

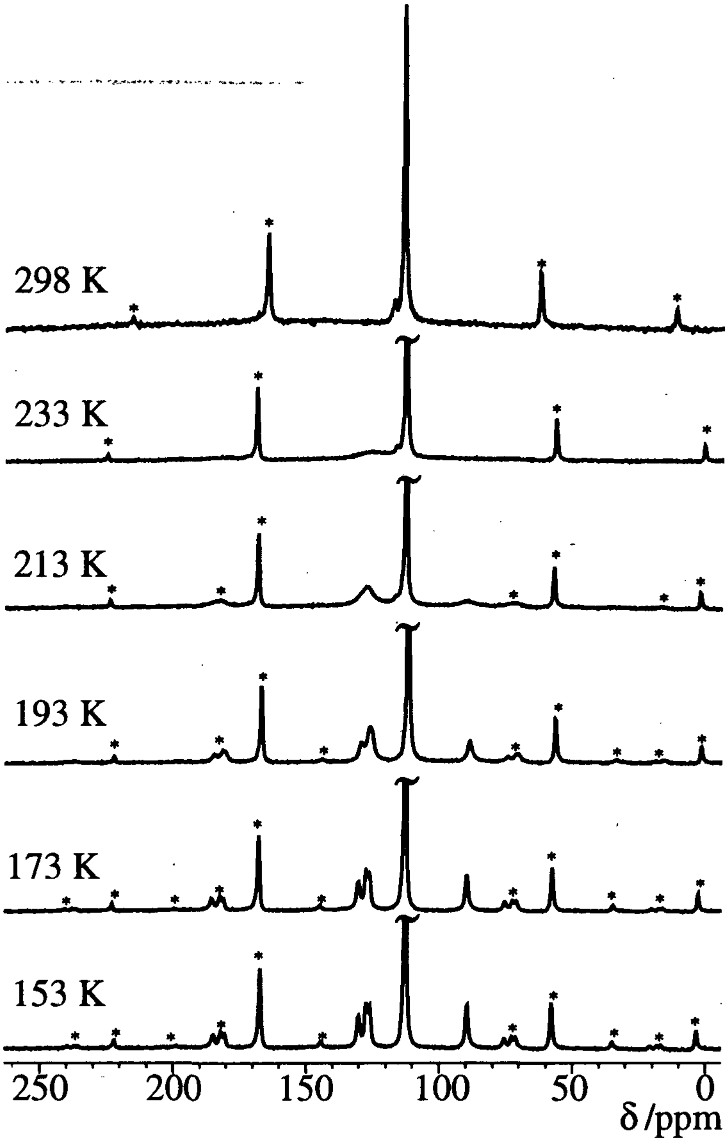

Figure 4.6 ^{13}C CP/MAS NMR spectra of **1**. The isotropic peak for η_5-C_5H_5 is plotted to the same height in each spectrum but is truncated in these plots. An asterisk is used to denote spinning sidebands.

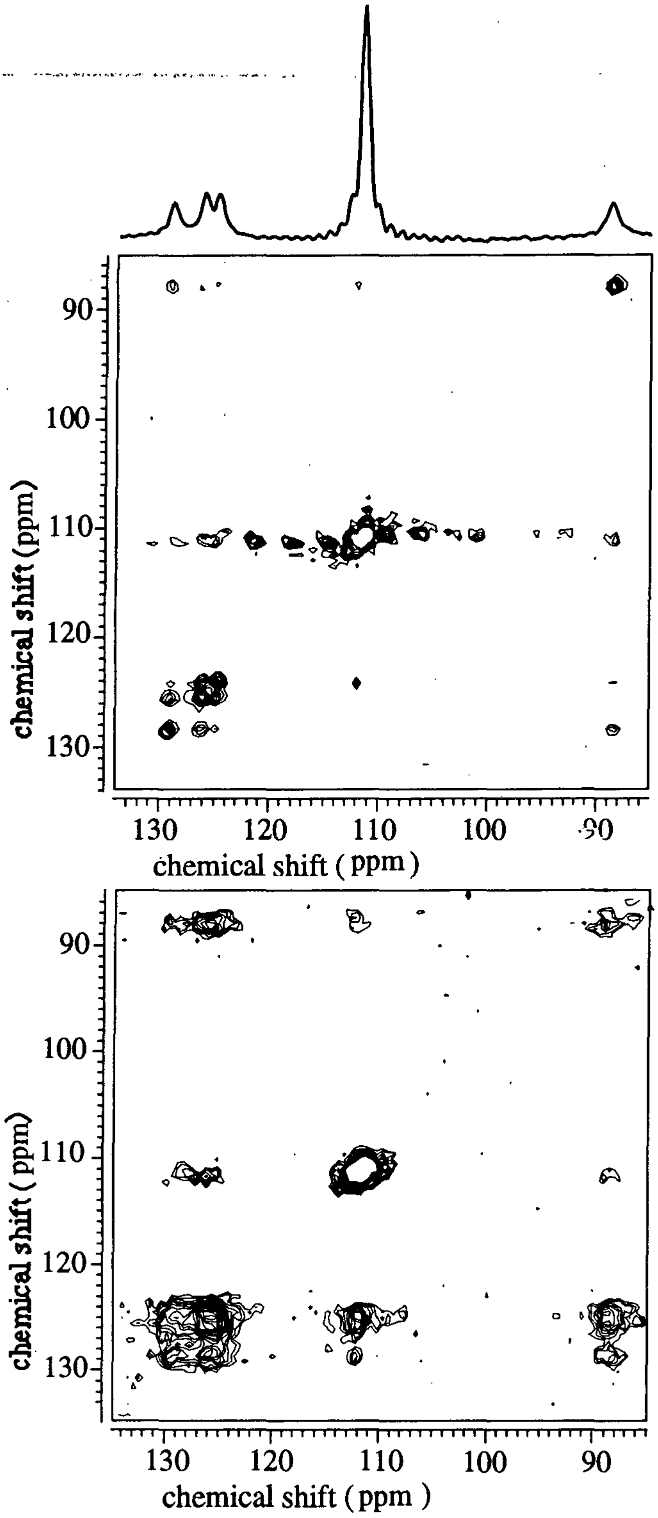

Figure 4.7 2D 75.739-MHz ^{13}C CP/MAS exchange spectrum of **1** at T=188K. The size of the data matrix was 128x256 before zero filling. In 3a) the mixing time was 50 ms. In 3b) the mixing time was 200 ms and we see multiple exchanges occurring.

ppm	90.0	113.0	126.5	127.9	130.7	
[1,2]	1	2	3	4	5	
1	-	X	-	-	X	1
2	X	-	X	-	-	3
3	-	X	-	X	-	5
4	-	-	X	-	X	2
5	X	-	-	X	-	4
	1	3	5	2	4	[1,3]

Figure 4.8 Diagram shows the cross peaks expected in the 2D exchange experiment with assignments of the carbon atoms for the given sigmatropic rearrangements.

4.3.2 $ZrCp_4$

The dynamic behavior of $ZrCp_4$ in solution was probed[114] using ^1H NMR spectroscopy. The spectrum yielded a sharp singlet at 5.83 ppm in $CDCl_3$ and 6.61 ppm in C_6D_6. Low temperature studies (to 138 K) were performed with no subsequent change in the spectrum, suggesting that th activation energies for intramolecular rearrangements in $ZrCp_4$ are extremely low. Additionally, solid state ^{13}C NMR studies were carried out at 300 K under static and magic angle spinning conditions. From the static spectrum chemical shielding tensors for the η^5-C_5H_5 ring could be calculated. Chemical shielding tensors for

ZrCp$_4$ are calculated to be $\sigma_{11} = 178$, $\sigma_{22} = 163.5$, and $\sigma_{33} = 34$. MAS yielded a single isotropic shift of 112.4 ppm.

We report VT ^{13}C CP/MAS spectra of ZrCp$_4$. The structure of ZrCp$_4$ is shown in figure 4.9. X-ray crystallography has shown the molecule to contain three η^5-C_5H_5 rings and one η^1-C_5H_5 ring[117]. The ^{13}C CP/MAS NMR spectra of ZrCp$_4$ in the temperature range of 173 K and 333 K are shown in figure 4.10. The spectrum at 333 K consists of a sharp peak at 112.8 ppm. This peak is assigned to the 15 carbon atoms of the three η^5-C_5H_5 rings. Rapid ring orientation is expected to average the carbon resonances of each individual ring and molecular and molecular symmetry ensures the equivalence of the three rings.

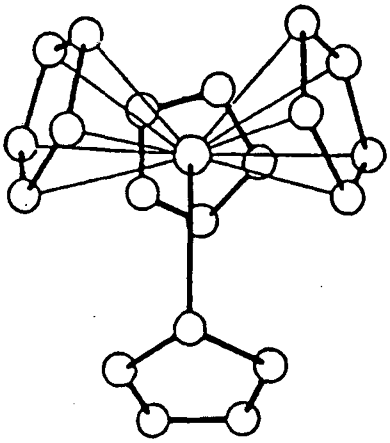

Figure 4.9 Representation of ZrCp$_4$ as obtained from X-ray structure determination.

At 173 K, six peaks are evident. The largest peak is still due to carbons in the pentahapto Cp rings. The five resonances at 119.1, 121.4, 124.3 138.3, and 141.0 are assigned to the monohapto group. Upon heating, the peaks begin to broaden and colesce indicating that exchange is occurring. However, 2D-exchange results at temperatures from 198 to 298 K with mixing times of up to 500 ms did not indicate exchange occurring at these temperatures and on these timescales. It is possible that it was on a slower timescale. As was pointed out by Rogers, et al.[117] the Zr-C(η^1) bond is a σ bond in a very crowded environment.

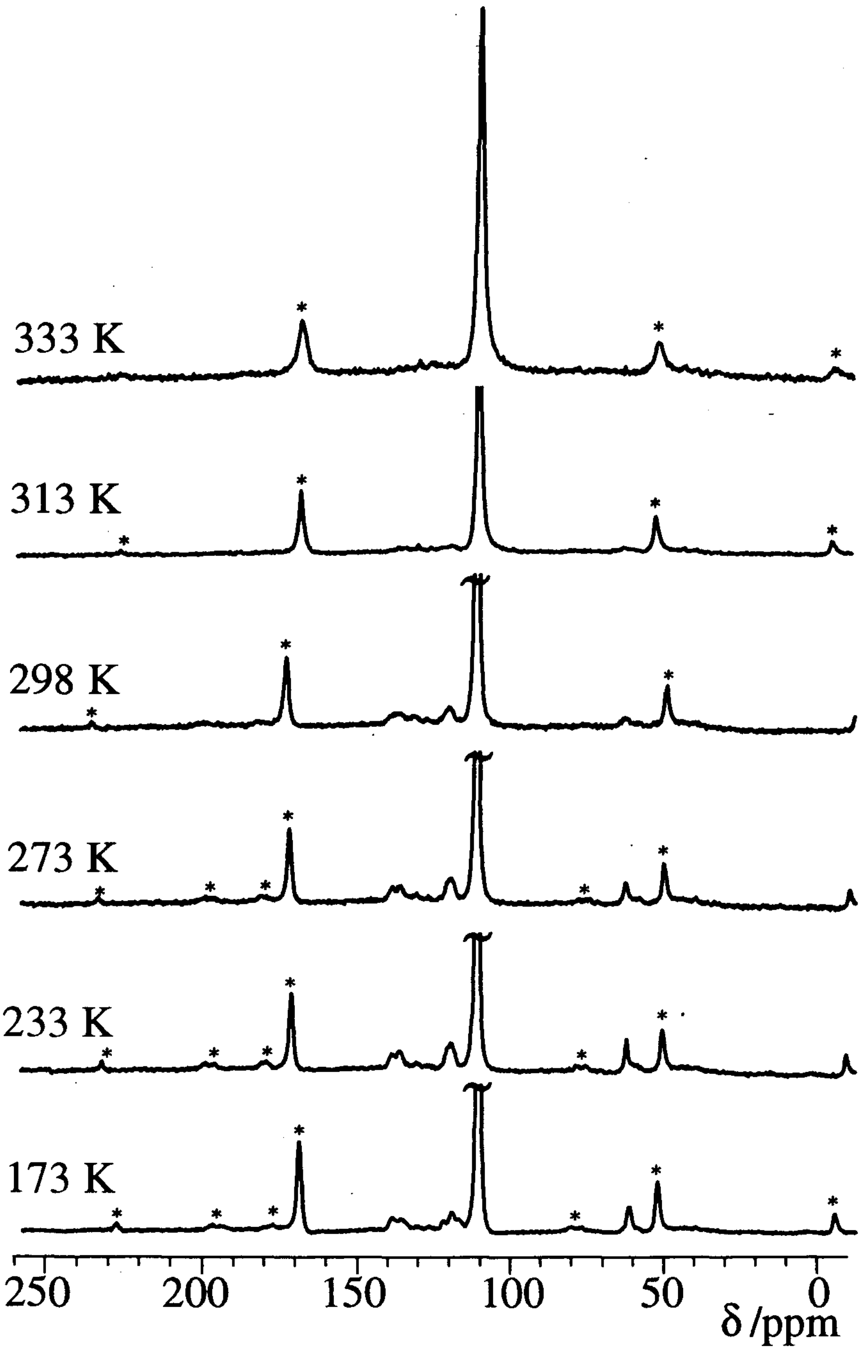

Figure 4.10 75.739-MHz ^{13}C CP/MAS NMR spectra of $ZrCp_4$ at different temperatures. The pentahapto peak is plotted to the same height in each spectrum but is truncated in these plots. Asterisks are used to denote spinning sidebands.

4.3.3 $SnCp_4$

The ^1H NMR spectrum of $SnCp_4$ in solution yielded sharp singlets at 5.96 ppm in$CDCl_3$ (with rapid chemical decomposition in this solvent) and 5.89 ppm in C_6D_6[114]. Once again, no significant changes were observed to 138 K. Static solid state ^{13}C NMR studies yielded chemical shielding tensor components of $\sigma_{11}=180$, $\sigma_{22}=143.5$, and $\sigma_{33}=31$. The MAS spectrum showed a singlet centered at 113.1 ppm.

We report VT ^{13}C CP/MAS NMR spectra of $SnCp_4$. The structure of $SnCp_4$ is shown in figure 4.11. X-ray crystallography has shown the molecule to contain four η^1-C_5H_5 rings bonded by normal σ bonds in a slightly distorted tetrahedral configuration. The ^{13}C CP/MAS NMR spectra of $ZrCp_4$ in the temperature range of 173 K and 333 K are shown in figure 4.12. The signal-to-noise is worse because of fewer acquisitions due to the long spin-lattice relaxation time. At ambient temperature a single resonance at 114.0 ppm is observed. As the temperature is lowered, the intensity of this resonance decreases as the intensity of resonances at 129.2 and 47.4 ppm increases. At 153 K only the resonances at 129.2 and 47.4 ppm are present. The peak at 129.2 ppm probably corresponds to the sp2 carbons in the sample while the 47.4 ppm probably corresponds to the σ-bonded carbon. Due to the long spin-lattice relaxation time, 2D exchange experiments were not attempted.

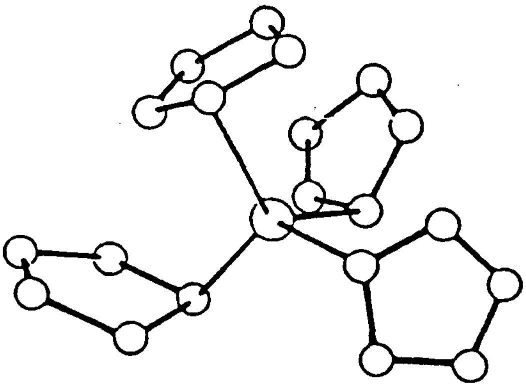

Figure 4.11 Representation of $SnCp_4$ as obtained from X-ray structure determination.

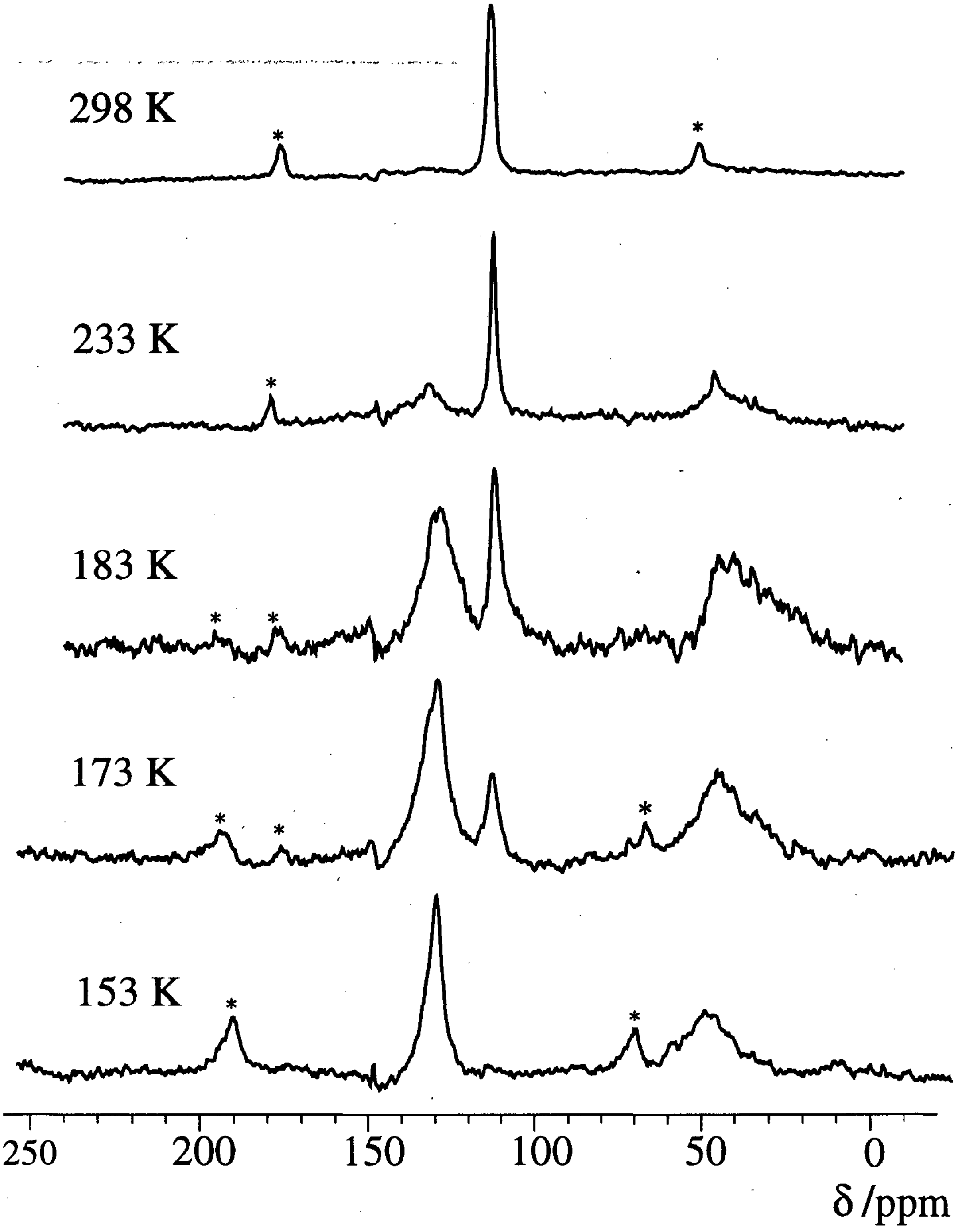

Figure 4.12 75.739-MHz ^{13}C CP/MAS NMR spectra of $SnCp_4$ at different temperatures. The spectra are scaled to the height of the tallest peak. Asterisks are used to denote spinning sidebands.

4.4 Herzfeld-Berger spinning sideband analysis

When the spinning frequency is less than the chemical shift anisotropy, the isotropic line in the NMR spectrum is flanked on both sides by sidebands spaced at the spinning frequency. The intensities of the spinning sidebands are related to the chemical shift anisotropy and provide an opportunity to recover the chemical shift parameters, as was first demonstrated by Herzfeld and Berger[118].

Recall that $\theta(t)$ is an oscillatory function of time with a variety of frequencies that are displaced from $\sigma_{iso}\omega_0$ by integral multiples of the rotation frequency, ω_r. A powder sample contains nuclei with all initial orintations. To obtain the spectrum, we once again integrate 4.30 over all orientations using the full $\theta(t)$ function.

$$I(\omega) = \langle I_x(0) \rangle \int_0^{\infty} e^{i\theta(t)} e^{-i\omega t} dt \qquad 4.30$$

where

$$\theta(t) = \omega_o \sum_{l=0}^{1} \sum_{m,m'=-2l}^{2l} \sigma_{2l,m} Y_{2l,m'}(\theta,\phi) d^{21}_{mm'}(\beta) \int_0^t \exp(-im' \omega_r t')dt' . \qquad 4.26$$

The exponential of a sine or cosine can be expanded by the use of a Bessel function

$$e^{iR\sin\alpha} = \sum_{k=-\infty}^{+\infty} e^{ik\alpha} J_k(R) \qquad 4.35$$

where $J_k(R)$ is a Bessel function of the first kind. Applying Bessel function treatment to our problem yields a frequency spectrum given by the intensity

$$I(\omega) = \int_{-\infty}^{+\infty} \exp(-i\omega t) \sum_{N=-\infty}^{+\infty} \exp(i\omega_o t\sigma) I_N \exp(iN\omega_r t)dt \qquad 4.36$$

The resulting spectrum will consist of a series of lines that have intensities I_N. These intensities depend on sums of products of Bessel functions over the initial random distribution of orientations.

Herzfeld and Berger show clearly that intensities of the sidebands relative to the center band (which is at the isotropic value) depend on the principal values of the chemical shift tensor. By convention, $|\sigma_{zz} - \sigma_{iso}| \geq |\sigma_{yy} - \sigma_{iso}| \geq | \sigma_{yy} - \sigma_{iso}|$, or equivalently, $\sigma_{11} \geq \sigma_{22} \geq \sigma_{33}$. They define two parameters

$$\mu = (\omega_0/\omega_r)(\sigma_{33} - \sigma_{11}) \qquad 4.37$$

which is always positive, for positive ω_r, and

$$\rho = (\sigma_{11}+\sigma_{33}-2\sigma_{22})/(\sigma_{33}-\sigma_{11}) \qquad 4.38$$

such that $-1<\rho<1$, the extreme values corresponding to axially symmetric tensors. They generate contours, μ versus ρ, for the relative intensities of the Nth sidebands compared to the intensity of the isotropic peak, $I_{\pm N}/I_0$. By determining the values of the ratios for the various sidebands of a line, it is possible to overdetermine the values of μ and ρ from which the principal values of the chemical shift tensor may be determined.

The experimental line intensities must be normalized in order to compare them directly with theoretical values. This requires an accurate measure and summation of the intensities of all the sidebands, and may be avoided by working instead with the ratios of the line intensities. Uncertainty in μ and ρ is due to experimental errors and errors in interpolation. Therefore, it is important that enough contours be considered to give accurate values of μ and ρ.

The results CSA tensors for the room temperature $HfCp_4$, $ZrCp_4$, and $SnCp_4$ are summarized in Table 4.1. The $HfCp_4$ and $ZrCp_4$ show an axially symmetric orientation of the principal axes, as expected from η^5-C_5H_5 rings. In addition, CSA tensors were calculated for $HfCp_4$ at 163 K, where the peaks are well-resolved. A problem arises when trying to use this program to calculate CSA tensors for overlapping lines. In this case we have used a program called Speedyfit[119], modified by Susan DePaul, to calculate CSA tensors by means of a least-squares fit of the data. The program calls a subroutine from Cern's MINUIT package to do the least squares fitting. Input parameters are used to simulate a spectrum which is then iteratively modified until it matches the data. The results for $HfCp_4$ are summarized in Table 4.2. Note that one of the monohapto peaks in $HfCp_4$ is buried beneath the pentahapto peak. This leads to difficulty in definitively assigning CSA tensors, since the CSA of that monohapto resonance is not the same as the pentahapto resonance. The intensities of the spinning sidebands are due to a combination of the anisotropy of one of the carbons in the monohapto Cp ring and the carbons in the pentahapto Cp rings. However, since the ratio is 5:1 pentahapto to monohapto carbons, the effect is probably minimal.

	η	σ_{11}	σ_{22}	σ_{33}
HfCp$_4$	0.00±0.01	163±1	162±1	15±1
ZrCp$_4$	0.01±0.15	157±5	156±9	24±5
SnCp$_4$	0.22±0.26	165±8	146±15	23±10

Table 4.1 CSA tensors from Herzfeld-Berger spinning sideband analysis for room temperature HfCp$_4$, ZrCp$_4$, and SnCp$_4$.

HfCp$_4$	η	σ_{11}	σ_{22}	σ_{33}
η^5-C_5H_5/C2	0.00±0.01	162±1	162±1	15±1
C1	1.00±0.04	157±1	90±1	23±1
C3	0.39±0.10	197±6	157±6	24±4
C4	0.41±0.11	199±4	158±6	26±4
C5	0.97±0.06	220±2	132±3	39±2

Table 4.2 CSA parameters for HfCp$_4$ C1-5 are as defined in figure 4.5.

References

(1) Mansfield, P.; Morris, P. G. *NMR Imaging in Biomedicine*; Academic Press: Orlando, 1982.

(2) Blumich, B. *Magnetic Resonance Microscopy: Methods and Appications in Materials Science, Agriculture and Biomedicine*; VCH: New York, 1992.

(3) Schmidt-Rohr, K.; Spiess, H. W. *Multidimensional Solid-State NMR and Polymers*; Academic Press: London, 1994.

(4) Yesinowski, J. P.; Buess, M. L.; Garroway, A. N.; Ziegeweid, M.; Pines, A. *Anal. Chem.* **67**, 2256-2263 (1995).

(5) Shaw, J. *NQI Newslett.* **1**, 26-229 (1994).

(6) Townes, C. H.; Dailey, B. P. *J. Chem. Phys.* **20**, 35 (1952).

(7) Mueller, K. T.; Chingas, G. C.; Pines, A. *Rev. Sci. Instrum.* **62**, 1445 (1991).

(8) Samosan, A.; Pines, A. *Rev. Sci. Instrum.* **60**, 3239 (1989).

(9) Nanz, D.; Ernst, M.; Hong, M.; Ziegeweid, M.; Schmidt-Rohr, K.; Pines, A. *J. Magn. Reson. A* **113**, 169-176 (1995).

(10) Levitt, M.; Freeman, R.; Frenkiel, T. *Adv. Magn. Reson.* **11**, 47 (1983).

(11) Rhim, W.-K.; Elleman, D. D.; Vaughan, R. W. *J. Chem. Phys.* **59**, 3740 (1973).

(12) Millar, J. M.; Thayer, A. M.; Bielecki, A.; Zax, D. B.; Pines, A. *J. Chem. Phys.* **83**, 934 (1985).

(13) Bielecki, A.; Zax, D. B.; Zilm, K. W.; Pines, A. *Rev. Sci. Instrum.* **57**, 393 (1986).

(14) Hoult, D. I.; Richards, R. E. *J. Magn. Reson.* **24**, 71 (1976).

(15) Raftery, D.; Long, H.; Meersman, T.; Grandinetti, P. J.; Reven, L.; Pines, A. *Phys. Rev. Lett.* **66**, 584-587 (1991).

(16) Knize, R.; Wu, Z.; Happer, W. *Adv. Atom. Mol. Phys.* **24**, 223 (1989).

(17) Buess, M. L.; Garroway, A. N.; Miller, J. B.; Yesinowski, J. P. In *Advances in Analysis and Detection of Explosives*; J. Yinon, Ed.; Kluwer Press: The Netherlands,

1993; pp 361-368.

(18) Bray, P. J.; Gravina, S. J.; Hintenlang, D. H.; Mulkern, R. V. *Magn. Resonan. Rev.* **13**, 263 (1988).

(19) Stephenson, D.; Smith, J. A. *Proc. R. Soc. Lond. A* **416**, 146 (1988).

(20) Edmonds, D. T. *Phys. Rep.* **29**, 233 (1977).

(21) Connor, C. Thesis, University of California at Berkeley, 1989.

(22) Chang, J. W. Thesis, University of California at Berkeley, 1991.

(23) Jaklevic, R. C.; Lambe, J.; Mercereau, J. E.; Silver, A. H. *Phys. Rev. A* **140**, 1628 (1965).

(24) Clarke, J. *Am. Jour. of Phys.* **38**, 1071 (1970).

(25) DeWaele, A. T. A. M.; Ouboter, R. D. *Physica* **41**, 225 (1969).

(26) McCumber, D. E. *J. Appl. Phys.* **39**, 2503 (1968).

(27) Kittel, C. *Introduction to Solid State Physics*; John Wiley and Sons: New York, 1986.

(28) Feynman, R. P.; Leighton, R. B.; Sands, M. *The Feynman Lectures in Physics*; Addison-Wesley Publishing: Reading, Mass., 1965; Vol. 3.

(29) Clarke, J. *Proce. IEEE* **61**, 8 (1973).

(30) Herrmann, K.; Zhang, Y. Z.; Muck, H. M.; Schubert, J.; Zander, W.; Braginski, A. I. *Supercond. Sci. Technol.* **4**, 583 (1991).

(31) Miklich, A. H.; Kingston, J. S.; Wellstood, F. C.; Clarke, J.; Colclough, M. S.; Char, K.; Zaharchuk, G. *Appl. Phys. Lett.* **59**, 988 (1991).

(32) Miklich, A. H.; Kingston, J. S.; Wellstood, F. C.; Clarke, J.; Colclough, M. S.; Char, K.; Zaharchuk, G. *Nature* **352**, 483 (1991).

(33) Motchenbacher, C. D.; Fitchen, F. C. *Low-Noise Electronic Design*; John Wiley and Sons: New York, 1973.

(34) Clarke, J.; Goubau, W. M.; Ketchen, M. B. *J. Low Temp. Phys.* **25**, 99 (1976).

(35) Horowitz, P.; Hill, W. *The Art of Electronics*; Cambridge University Press:

Cambridge, Mass., 1980.

(36) Clarke, J. *IEEE Trans. Magn.* **MAG-19**, 288 (1983).

(37) Narasimhan, L. R.; Takigawa, M.; Ketchen, M. B. *Appl. Phys. Lett.* **65**, 1305-1307 (1991).

(38) Hurlimann, M., personal communication.

(39) Chamberlain, R. V.; Moberly, L. A.; Symko, O. G. *J. Low Temp. Phys.* **35**, 337 (1979).

(40) Webb, R. A. *Rev. Sci. Instrum.* **48**, 1585 (1977).

(41) Das, T. P.; Hahn, E. L. *Solid State Physics Supplement 1*; Academic Press: New York, 1958.

(42) Slichter, C. P. *Priciples of Nuclear Magnetic Resonance;* 3rd ed.; Springer-Verlag: New York, 1990.

(43) Blaha, P.; Schwarz, K. *NQI Newslett.* **1**, 32 (1994).

(44) Hunt, M. J. *J. Magn. Reson.* **15**, 113-121 (1974).

(45) Gerstein; Dybowski *Transient Techniques in NMR of Solids: An Introduction to Theory and Practice*; Academic Press: Orlando, 1985.

(46) Freude, D.; Haase, J. In *NMR Basic Principles and Progress*Springer-Verlag: Berlin Heidelberg, 1993; Vol. 29.

(47) Mueller, K. T.; Sun, B. Q.; Chingas, G. C.; Zwanziger, J. W.; Terao, T.; Pines, A. *J. Magn. Reson.* **86**, 470 (1990).

(48) Samosan, A.; Kundla, E.; Lippmaa, E. *J. Magn. Reson.* **49**, 350 (1982).

(49) Wu, Y.; Sun, B. Q.; Pines, A.; Samosan, A.; Lippmaa, E. *J. Magn. Reson.* **89**, 297 (1990).

(50) Hoatson, G. L.; Vold, R. L. In *NMR Basic Principles and Progress*Springer-Verlag: Berlin Heidelberg, 1994; Vol. 32.

(51) Werner, U.; Black, B.; Ziegeweid, M.; Pines, A. *Chem. Phys. Lett.* **209**, 17 (1993).

(52) Werner-Zwanziger, U.; Ziegeweid, M.; Black, B.; Pines, A. Z. *Naturforsch.* **49a**, 1188-1192 (1994).

(53) Muha, G. M. *J. Chem. Phys.* **73**, 4139 (1980).

(54) Day, E. P. *Phys. Rev. Lett.* **29**, 540 (1972).

(55) Abragam, A.; Kambe, K. *Phys. Rev.* **91**, 894 (1953).

(56) Bloembergen, N.; Shapiro, S.; Pershan, P. S.; Artman, J. O. *Phys. Rev* **114**, 445 (1959).

(57) Suter, D.; Ernst, R. R. *Phys. Rev. B* **32**, 5608 (1985).

(58) Black, B. Thesis, University of California at Berkeley, 1993.

(59) Scott, T. A. *J. Chem. Phys.* **36**, 1459 (1962).

(60) Leppelmeier, G. W.; Hahn, E. L. *Phys. Rev.* **141**, 724 (1966).

(61) Fan, N.-Q. Thesis, University of California at Berkeley, 1990.

(62) Blinc, R. In *Advances in nuclear quadrupole resonance*; J. A. Smith, Ed.; Heyden: London, 1975; Vol. 2; pp 71.

(63) Blinc, R. In *26th Congress Ampere on Magnetic Resonance*; Athens, Greece, 1992; pp .

(64) Hurlimann, M. D.; Pennington, C. H.; Fan, N.-Q.; Clarke, J.; Hahn, E. L. *Phys. Rev. Lett.* **69**, 684-687 (1992).

(65) TonThat, D. M.; Clarke, J. *Rev. Sci. Instrum.* submitted (1995).

(66) Abragam, A. *Principles of Nuclear Magnetism*; Oxford University Press: 1960.

(67) Kistenmacher, T. J.; Rand, G. A.; Marsch, R. E. *Acta Cryst.* **B30**, 2573 (1974).

(68) Brock, C. P.; Schweizer, W. B.; Dunitz, J. D. *J. Amer. Chem. Soc.* **113**, 9811 (1991).

(69) Edmonds, D. T.; Summers, C. P. *J. Mag. Res.* **12**, 134 (1973).

(70) Bowers, C. R.; Long, H. W.; Pietrass, T.; Gaede, H. C.; Pines, A. *Chem. Phys. Lett.* **205**, 168-170 (1993).

(71) Gaede, H. C.; Song, Y.-Q.; Taylor, R. E.; Munson, E. J.; Reimer, J. A.; Pines,

A. (1995).

(72) Ziegeweid, M.; TonThat, D. M.; Song, Y.-Q.; Appelt, S.; Munson, E.; Clarke, J.; Pines, A. *Chem. Phys. Lett.* in preparation (1995).

(73) Kastler, A. *J. Phys. Radium* **11**, 255 (1950).

(74) Kastler, A. *Science* **158**, 214 (1967).

(75) Dehmelt, H. G. *Phys. Rev.* **109**, 381 (1958).

(76) Walters, G. K.; Colegrove, F. D.; Schearer, L. D. *Phys. Rev. Lett.* **8**, 439-442 (1962).

(77) Happer, W.; Miron, E.; Schaefer, S.; Schreiber, D.; Wijngaarden, W. A. v.; Zeng, X. *Phys. Rev. A* **29**, 3092 (1984).

(78) Zeng, X.; Wu, Z.; Call, T.; Miron, E.; Schreiber, D.; Happer, W. *Phys. Rev. A* **31**, 260 (1985).

(79) Bouchiat, C. C.; Bouchiat, M. A.; Pottier, L. C. *Phys. Rev.* **181**, 144 (1969).

(80) Bouchiat, M. A.; Brossel, J.; Pottier, L. C. *J. Chem. Phys.* **56**, 3703 (1972).

(81) Grover, B. C. *Phys. Rev. Lett.* **40**, 390 (1978).

(82) Volk, C. H.; Kwon, T. M.; Mark, J. G.; Kim, Y. B.; Woo, J. C. *Phys. Rev. Lett.* **44**, 136 (1980).

(83) Gamblin, R. L.; Carver, T. R. *Phys. Rev.* **138**, 946 (1965).

(84) Herman, R. M. *Phys. Rev.* **137**, 1062 (1965).

(85) Bhaskar, N. D.; Happer, W.; McClelland, T. *Phys. Rev. Lett.* **49**, 25 (1982).

(86) Drung, D.; Cantor, R.; Peters, M.; Scheer, H. J.; Koch, H. *Appl. Phys. Lett.* **57**, 406-408 (1990).

(87) Drung, D.; Cantor, R.; Peters, M.; Ryhanen, T.; Koch, H. *IEEE Trans. on Magn.* **27**, 3001-3004 (1991).

(88) Gatzke, M.; Cates, G. D.; Driehuys, B.; Fox, D.; Happer, W.; Saam, B. *Phys. Rev. Lett.* **70**, 690-693 (1993).

(89) Warren, W. W.; Norberg, R. E. *Phys. Rev.* **148**, 402 (1966).

(90) van Kranendonk, J. *Physicsa (Amsterdame)* **20**, 781 (1954).

(91) Pershan, P. S. *Phys. Rev.* **117**, 109 (1960).

(92) Warren, W. W.; Norberg, R. E. *Phys. Rev.* **154**, 277 (1967).

(93) Gonen, O.; Waugh, J. S. *Physica* **156A**, 219 (1989).

(94) Cotton, F. A. In *Dynamic Nuclear Magnetic Spectrsocopy*; C. Jackman, Ed.; 1975; pp 377-440.

(95) Piper, T. S.; Wilkinson, G. J. *J. Inorg. Nucl. Chem.* **3**, 104 (1956).

(96) Piper, T. S.; Wilkinson, G. J. *J. Inorg. Nucl. Chem.* **3**, 32 (1956).

(97) Bennett, M. J.; Cotton, F. A.; Davison, A.; Faller, J. W.; Lippard, S. J.; Morehouse, S. M. *J. Am. Chem. Soc.* **88**, 4371 (1966).

(98) Woodward, R. B. (1965).

(99) Cotton, F. A. *Acc. Chem. Res.* **1**, 257 (1968).

(100) Mann, B. E. In *Comprehensive Organometallic Chemistry*; G. Wilkinson, F. G. A. Stone and E. W. Abel, Ed.; Pergammon Press: Oxford, 1982; Vol. 3; pp 89-171.

(101) Heyes, S. J.; Dobson, C. M. *J. Am. Chem. Soc.* **113**, 463-469 (1991).

(102) Kuemmerlen, J.; Sebald, A. *J. Am. Chem. Soc.* **115**, 1134-1142 (1993).

(103) Kuemmerlen, J.; Lange, I.; Milius, W.; Sebald, A.; Blaschette, A. *Organometallics* **12**, 3541-3544 (1993).

(104) Benn, R.; Grondey, H.; Nolte, R.; Ecker, G. *Organometallics* **7**, 777-778 (1988).

(105) Benn, R.; Mynott, R.; Topalovic, I.; Scott, F. *Organometallics* **8**, 2299-2305 (1989).

(106) Benn, R.; Grondey, H.; Erker, G.; Aul, R.; Nolte, R. *Organometallics* **9**, 2493-249 (1990).

(107) Pines, A.; Gibby, M. G.; Waugh, J. S. *J. Chem. Phys.* **56**, 1776 (1972).

(108) Hartmann, S. R.; Hahn, E. L. *Phys. Rev.* **128**, 2042 (1962).

(109) Lowe, I. *Phys. Rev. Lett.* **2**, 285 (1959).

(110) Andrew, E. R.; Bradbury, A.; Eades, R. G. *Nature* **182**, 1659 (1958).

(111) Stejskal, E. O.; Schaefer, J.; McKay, R. A. *J. Magn. Reson.* **25**, 569 (1977).

(112) Doty, F. D.; Inners, R. R.; Ellis, P. D. *J. Magn. Reson.* **43**, 399-416 (1981).

(113) Haw, J. F.; Campbell, G. C.; Crosby, R. C. *Anal. Chem.* **58**, 3172-317 (1986).

(114) Allen, G. Thesis, University of Sydney,

(115) Calderon, J. L.; Cotton, F. A.; Takatas, J. *J. Am. Chem. Soc.* **93**, 3587-3597 (1971).

(116) Rogers, R. D.; Bynum, R. V.; Atwood, J. L. *J. Am. Chem. Soc.* **103**, 692-693 (1981).

(117) Rogers, R. D.; Bynum, R. V.; Atwood, J. L. *J. Am. Chem. Soc.* **100**, 5238-5239 (1978).

(118) Herzfeld, J.; Berger, A. E. *J. Chem. Phys.* **73**, 6021-6030 (1980).

(119) de Groot, H. J. M. *J. Chem. Phys.* **73**, 6021 (1980).

Appendix A: Notes on the CW-SQUID spectrometer

The sample

The pickup coil is designed to fit a standard 5 mm NMR tube. Two different types of samples are used: sealed and unsealed samples. The unsealed sample is quick and easy. However, it will not work for air/water sensitive compounds. It is also not desirable for liquid samples, expensive samples, or samples available in only a limited quantity. Since they are attached to the sample stick with grease (which becomes hard at 4.2 K), contamination is eventually possible and removal is very difficult. Typically, we use the standard thin walled NMR tubes (505-PS-9" from Wilmad Glass). The sample tube will not fit on the stick if the walls are thicker. We typically make 3 unsealed samples from one 9" NMR tube, each approximately 3" long.

The standard thickness NMR tubes break under the stress placed on sealed samples. Therefore we use a thicker walled NMR tube (503-PS-8" from Wilmad Glass). We typically make 2 sealed samples form one 8" tube, since more glass is required to seal the samples. The tube is sealed while the sample is immersed in LN2 and a tip is formed at the end. Dental floss is attached to the tip by silicon adhesive. The silicon works better than anything else we have tried, possibly because it bonds better to the silicon in the glass or because even at 4.2 K it is still somewhat elastic. The dental floss is threaded through a hollow tube topped by NMR tube cap.

The sample, attached to the sample stick, is inserted into the probe. The pickup coil is 86 cm from the top of the flange. Measuring 86 cm from the top and bottom of the sample ensure that the sample is in the pickup coil. It is always best to insert the sample into the probe before cooling everything down if you have that option in order to minimize icing. However, it is possible to change samples by pulling up the sample, changing samples, making sure the sample tube and stick are dry, and reinserting it into the probe. Insert warm samples into cold dewars slowly (to minimize boil off) and in the presence of a magnetic field (in case the boil off warms the superconducting static field circuit). Another way of determining if the sample is to use the SQUID as a magnetometer. Monitor the output on the oscilloscope screen. When the sample enters the pickup coil, the sign of the output will change (i.e. if the voltage was going down, it will start to go up and vice versa).

Note on irradiating samples to reduce T_1. I've never done it, but it has been brought up in discussions by Alex as something that might be done. Apparently there is a Co-60 source (gamma rays) on the hill. Bring the sample in LN2, blast it, induce free radicals, and keep it stored at least at LN2 to prevent it from healing. It is probably necessary to consider the potential damage to proteins and other structures irradiation would cause.

Filling

It takes a while for the dewar to cool. Therefore it is a good idea to fill the dewar with LN2 at least several hours in advance or, preferably, overnight to allow the temperature to reach 77 K inside the dewar. We have a resistor placed on the sample can to monitor the temperature. Room temperature is ~.15 ohms. LN2 temperature is ~.18 ohms. The resistance increasing more rapidly at lower temperatures. At 4.2 K the resistance is ~1.4 ohms.

We are hooked into the helium recovery system. Therefore, when you fill the dewar with LHe, the system should be closed to the atmosphere and open to the recovery system. We don't want to waste LHe or freeze the LHe meter. Therefore, until the dewar is cooled to 4.2 K we keep the pressure in the LHe dewar low (~1 atm), and keep a heat gun on the hose between the dewar and the meter. When liquid starts filling, the pressure in the LHe dewar can be increased to 2 atm. You can tell when it starts filling because the resistance increases rapidly and the flow of He gas into the recovery system diminishes. When you are finished filling, close the recovery line and open the system to atmosphere. You cannot run the spectrometer while hooked up to the recovery system because the pressure in the line is not constant and produces strange baselines in the spectra. However, when there is LHe in the dewar and we are not running, the dewar should be hooked up to recovery, including overnight.

There is a LHe meter to measure the amount of LHe that is in the dewar once the system is cooled. It is not calibrated. However, filling to ~35% is enough LHe for a day's run. Depending on how well the system is behaving, you can run until the level is ~22-24%. The dewar is not empty at this point, but around the level of the SQUID. Assuming no field changes, it scales as ~1%/hr. To run longer, simply scale up the fill. Unless you are running overnight, don't put in enough LHe to last overnight unless as this is simply a waste of LHe.

Remember that the field should be turned on before the liquid helium is introduced. This is necessary to trap the flux. If it should be necessary to change the field, turn the SQUID off, set the new desired field, and lift the probe out of the dewar enough to warm it above the critical temperature of the lead. Then put it back down. Because the meter on the power supply is not very accurate, the power supply should be hooked up to an ammeter when applying current to generate the static magnetic field. The solenoid we currently have gives 108 kHz (proton)/A applied current. Therefore, you can set the field fairly accurately. Do not hook up the RF leads until after you are finished filling. You do not want to introduce any unnecessary sources of noise into the spectrometer which could be trapped by the superconducting components.

If the dewar goes soft and needs to be pumped out, it can be removed from the cage with the planks located near the cage. (Presently they are behind the filing cabinet.) Since the dewar has never gone soft on me, I've only pumped on it once for the sake of procedure when the previous graduate student was leaving. Dinh is an expert at pumping on dewars should the need ever arise.

Setup

Don't turn the SQUID till you have finished filling and the SQUID is superconducting. In practice, it takes a little while for it to settle down so wait ~15-20 minutes or so. Push the red button, reset if necessary, and then start turning up the trim pot till the needle goes up to its maximum. After that it only goes down.

The HP 3326A Two Channel Synthesizer. Turn the power on. It will go through a calibration routine and probably come up with error 193 or similar number. Reset the sweeper if this happens. If the error comes up again, turn the power off and start over. For all of our experiments, the primary channel that we use is the B channel. The rf coils have been optimized to maximize the rf tolerance of one channel at the expense of the other. If we optimize for both channels we settle for a significantly lower rf tolerance for both of them. This is not a problem for double resonance experiments since the sweeper can generate two channels that are mixed and output from a single channel. We cannot arbitrarily choose the sweep time. Please select 1, 5, 10, 25, 50, 100, 250, 500, 1000 second intervals only.

The application of an RF field effects the operating level of the SQUID. It may be that the RF still produces magnetic fields across the junction which damps the critical current. Anyway, to determine the RF tolerance for the two channels we turn up the amplitude until the SQUID level is at 50%. This is an arbitrary measure that is used as a gauge from one run to another. Turning up the amplitude produces a damped oscillation of SQUID levels. Therefore, we also measure the 2nd and 3rd maxima if we think that we'll need more rf than what we can get for the first maxima. For the ^{14}N experiments, we usually need at least 3.0 volts on the first maximum. Keep in mind that if your coil configuration changes or some reason, the rf tolerance will change based on the coupling of the coil. 3.0 V is usually enough to excite even the 3 Larmor lines.

We use the oscilloscope to visually monitor the SQUID level (voltage output) during scans. Since a change in magnetization is manifested by a change in the output voltage of the SQUID, it is necessary to keep the voltage in the range of detection. In the next section, I'll talk about changing scale during running experiments. In order to monitor the signal during acquisition, the oscilloscope screen is set to match the range of the screen in the acquisition program. Therefore, the top of the screen of the scope corresponds to the top of the range the acquisition. Each square on the scope corresponds to 0.5 V. If the scope doesn't correspond to the acquisition program, then you must reset it. Select continuous sweep with a fast sweep time (e.g. 1 s) in xaccel8, adjust the middle of the scope to the middle of the screen, and then adjust the scope so that the top and bottom of the oscilloscope screen correspond to the top and bottom of the acquisition screen. Make sure when you do this that you have xaccel8 set to full mode rather than compressed mode.

Xaccel8

Xaccel8 is our data acquisition program, written in Pascal, and last modified by Bruce Black. To begin the program, type xaccel8 at the prompt. Note, that the sweeper must be turned on first because the program will try to set the sweeper and test its GPIB connection. Currently this is operated on a 286 with EGA screen. Therefore, there are several available colors that are used to convey different states of the acquisition. The screen is normally white. The screen is yellow if you are viewing a spectrum in full scale. (Full scale should only be used for viewing spectra not acquiring them due to the diminished resolution when acquiring in full scale mode.) During acquisition, the screen is red. If the spectrometer is out of range, the screen turns blue. There is a dc offset which adjusts the output level of the SQUID to a fixed initial voltage after a recycle delay or during averages. The dc offset has a finite range of 10 V, which if exceeded, can't compensate the output voltage of the SQUID.

Xaccel8 has a number of features:

ScanType	(T) Let's you choose 1 or 2 channels.
Continuous Shot:	(C) Continuous Sweeps
Single Shot	(S) One Sweep

Write (W) Saves your spectrum for single shot experiments.

**Naming files. In DOS you can have an 8 character.3 character extension. The way files have been names is a sequential run number, followed by a 1 or 2 character sample code, followed by a scan number (associated with a specific set of parameters), the period, and the file number (for averages with the same parameters).*

Average (A) Multiple sweeps of the same parameters

**This uses the second channel for dc offset. If you want to run double resonance you have to babysit and manually set it. It will automatically write the sweeps to files. During setup, type in a base file name. The program adds ".sweep#" in good PC fashion. Do not type the period because it will either crash or not write the files, or continually overwrite the first one. (I forget which)*

Multisweep (M) Runs multiple sweeps with different parameters.

View (V) Setup for multiple runs.

** This has the same comments as Averages.*

HPSetup (H) Sets up parameters for Single Shot, Average, and Continuous Sweeps

Delay (D) Let's you set a delay before the scan is taken.

**Particularly useful for averaging or multiple sweeps when you need recycle time in between scans.*

Full/Compress (F) Full scale or not

** Important when running to be in compress. It affects the resolution of the spectrum!!!*

Mode, Oscilloscope (never used them, so I don't know)

Scanning

There are modes on the SQUID controller. For running it should be set in normal mode.

From the SQUID output, the signal goes to the integrator box, which is essentially an additional amplifier and filter. Select gain 20,40,60,80, 100 . This is in addition to the amplifier on the SQUID controller which should be set at 100. From here, the signal is split to the oscilloscope and the digitizer. While acquisition is in progress the screen is not updated except for the time. In order to monitor the sweep, you need to check the oscilloscope and maybe the frequency reporter. 500 kHz tends to be a bad frequency. Try to avoid starting, stopping, and sitting on that frequency. It may also be bad during the scan if you are running on a second or third maximum.

Analyzing Data

Two programs exist to analyze data and one to correct for field for spin I=1 nuclei:

Spec30 (written in Pascal, last modified by Bruce Black)

* Bruce's program takes out jumps and spikes caused by flux jumps in the SQUID, which are jumps to a different output within a single data point. It is necessary to take these out before you can take a derivative. Type h for help screen that displays commands.

SQUID15 (written in Fortran by Ulli Werner-Zwanziger)

*Use Ulli's if you want to apply broadening and take a derivative.

* Ulli's program is written in a half-German half-English mix.

Both are quirky, but between the two you can usually do what you want. There are features that I would have like to have had that weren't present in either one, but hey, I didn't write them in, did I?

Speksim (written in Fortran by Ulli)

Corrects for the effects of an applied magnetic field on the quadrupole coupling constant and asymmetry parameter. Could be better if someone would modify it to iteratively fit the data. However, the way you go about it now is to input a guess for Cq and η, and see how well it fits the data when you input the known magnetic field. The magnetic field can be known fairly precisely since you can generally measure a proton Larmor line.

The Probe

Checking the connections on the probe:

Resistances: The static field coil should be ~1.1 ohm (1.0-1.2 maybe)

The rf field coils should have resistances ~0.6 ohm (.5-.7?)

Give a tug on the wires and make sure that they are secure.

The winding pattern of the Helmholz coils can be found in the notebooks. The pickup coil is wound of NbTi and should have an inductance of ~2μH. We actually tried a gradiometer configuration to get rid of external noise. However, the relation of the size of the gradiometer to the saddle rf coils was such that the B1 fields I suspect are severely distorted and it never worked very well. The gradiometer configuration also cuts down on signal by a factor of 2 (since only half the inductance is in the pickup, the other half being in the reference) but it potentially attenuates the noise by a greater factor (depending on how well balanced it is) and so there is potentially a net gain. The inductance of any coil that you wind can be checked with the vector impedance meter in D62.

Leads to the input coil are NbTi and are superconducting at 4.2 K as is the Nb block. Therefore, it is imperative that the wires is behind the copper leads from the low pass filter. Otherwise, the superconducting circuit is broken. The leads shoul have lead tubing surrounding them for shielding purposes. All wires on the probe should be twisted whenever possible to eliminate stray inductance.

Adjusting the alignment of the sample tube is realized by tightening and loosening the three screws located above the coil forms.

Schematic of Power Supply Hookup

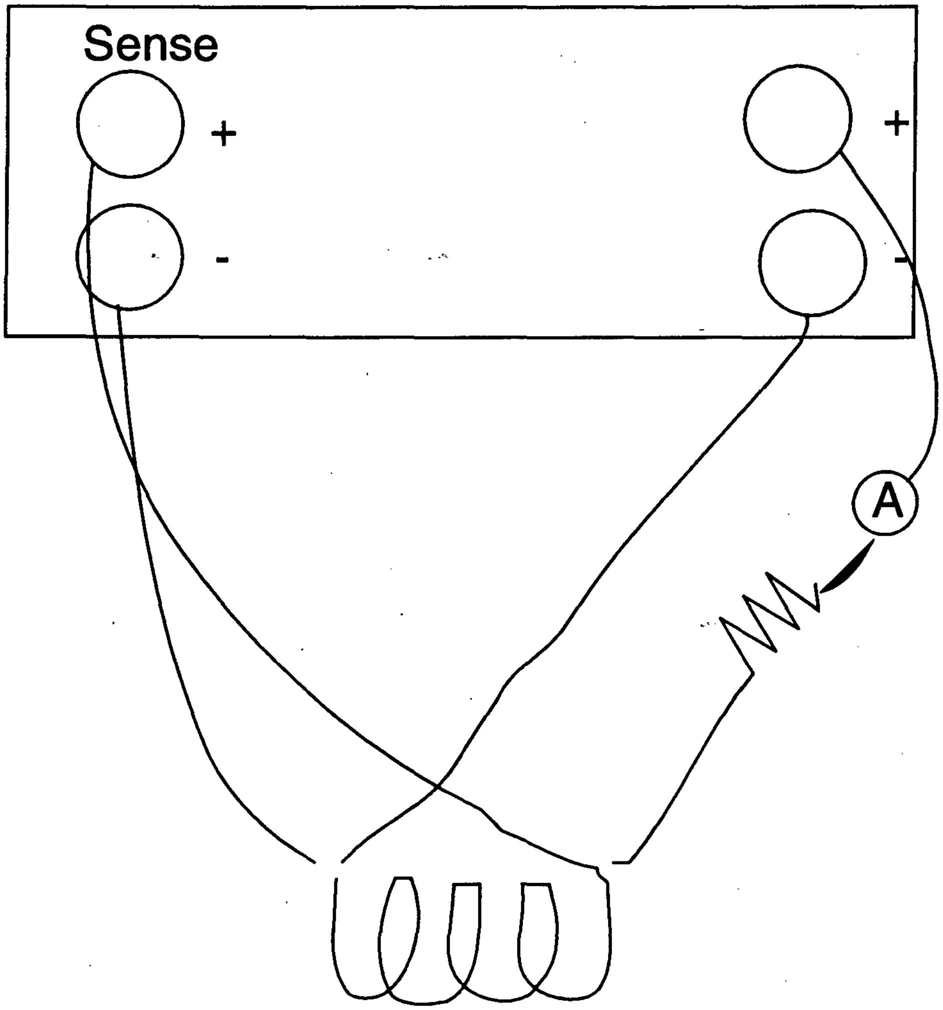

Figure A.1 Schematic of power supply hookup for the applied static magnetic field.

Appendix B Operating Procedure for Optical Pumping with the SDL-8630 Laser

This assumes the rough pump is continually on and the SQUID is in the dewar ready to go.

1) Walk in the room.

2) Fill the dewar with LN2 to start it cooling (should sit at least 1, preferably 2 hours before filling LHe)

3) Start diffusion pump:

  a) Make sure cooling water is running.

  b) Trip blue switch to remove low flow interlock.

  c) Turn on variac to start warming up the oil.

  d) Open the valves to diffusion pump. (Right gets turned to vertical position, left is turned 180

  degrees to so it too is vertical)

4) Pump until the vacuum is good, ideally mid 10^{-6} torr range

5) If glassware not open to vacuum, pump out all glassware leading up to the pumping cell.

6) Pump out the pumping cell.

7) Close stopcock to rack and sample tube. Measure the pressure of Xe in the sidearm.

8) Purify Xe. (basically the old freeze pump thaw method)

  a) Freeze Xe into sidearm.

  b) Close stopcock.

  c) Let warm up. Heat it with a heat gun & beat it with something relatively soft so that the glass doesn't break.

  d) Freeze Xe into sidearm, open stopcock to pump and let it pump down.

  e) Repeat as necessary.

9) Start vaporizing Rb.

  a) Cell should have a bluish tinge. If not torch some Rb so that it does.

  b) Start N2 flowing.

c) Turn on variac.

d) Thermocouple reads in F. Conversion chart on vacuum rack. We want ~80C.

10) Turn on power to laser driver.

11) Hit the TEMP button. Make sure the temperature is stabilized.

12) Turn power to laser on.

13) Hit current. Turn up to ~1.5A.

14) Use monochrometer select and IR viewer to get a bright glow of Rb. (If it flickers, then it is not set quite right)

15) Introduce Xe into the pumping cell. When the Xe is introduced, the glow should quench and then the brightness should grow back in.

a) Close next stopcock up the line. Open stopcock to the Xe and the pumping cell.

b) Close the stopcock to the pumping cell.

c) Freeze remaining Xe back into sidearm.

16) While the Xe pumps, prepare the sample cell. (In our case for right now, this is just pumping out the sample tube)

17) Turn variac off. Leave N2 flowing until 95F (35C).

18) Close stopcock to vacuum rack.

19) Close shutter on laser.

20) Check the pressure of the Xe.

21) Freeze the Xe into the tip of the sample cell in the presence of strong magnetic field. (For us this is a permanent magnet in a small LN2 dewar)

22) Close stopcock on sample tube and line to sample tube. Shut off current that generates the magnetic field in the pumping cell. Carry frozen Xe with field and lower into spectrometer.

23) Disconnect magnetic field around dewar, close door, acquire spectrum, process data.

24) If finished, turn off laser.

a) Turn down current.

b) Turn power to laser off.

c) Turn off power to laser driver.

ERNEST ORLANDO LAWRENCE BERKELEY NATIONAL LABORATORY
ONE CYCLOTRON ROAD | BERKELEY, CALIFORNIA 94720

Prepared for the U.S. Department of Energy under Contract No. DE-AC03-76SF00098